Autonomous Navigation for Binary Asteroid Landing

A vision-based and altimeter-aided navigation filter for small spacecraft

Peter Elffers

TUDelft

Autonomous Navigation for Binary Asteroid Landing

A vision-based and altimeter-aided navigation filter for small spacecraft

Thesis report

by

Peter Elffers

to obtain the degree of Master of Science
at the Delft University of Technology
to be defended publicly on April 26, 2023 at 14:00

An electronic version of this thesis is available at `http://repository.tudelft.nl/`.

Cover image: "In the Coldness of Space" by Smattila on DeviantArt | With written permission.

Faculty of Aerospace Engineering · Delft University of Technology

TUDelft

Delft
University of
Technology

Preface

For many decades, asteroids have captured the attention of scientists. Their uniquely preserved environment since the formation of the Solar System, potential for rare materials mining, and potentially hazardous nature when on a collision course with Earth, have prompted space agencies to send spacecraft to these faraway icy and metallic rock formations in space.

Every spacecraft that is sent to an asteroid needs a navigation system. Over the course of many asteroid missions, the technology in asteroid navigation has brought forth many ingenious technical solutions. A prime example is the Japanese asteroid mission Hayabusa-1, which threw bright objects onto the asteroid surface. These bright objects were subsequently used to navigate the spacecraft to land on the asteroid surface.

Increasing the autonomy of the navigation system used in the vicinity of asteroids is identified as a major contribution to improving the safety and scientific capabilities of the spacecraft. This research work contributes to the existing body of scientific research by proposing an autonomous navigation solution that is designed to operate in a binary asteroid environment.

This thesis project marks the end of my studies at the TU-Delft. It has been an unforgettable experience which shaped my life in many different ways. As a kid I was fascinated with everything that could fly, and aerospace engineering was the only study program I ever seriously considered. I am glad that this passion for flying things was always on my mind, allowing me to push through the challenging times.

Thank you Erik-Jan van Kampen and Erwin Mooij for your support during this thesis project. Often times, I felt that I was getting much more than just the support needed to achieve the goals set out in the thesis. Thank you for being so involved with the project work and helping me become a better engineer.

This project would not have been possible without the support from Airbus Defence & Space in Friedrichshafen. Thank you Edoardo Caroselli for being there for me every day and night of the project duration, you helped me solve many issues that would have otherwise delayed the project. I want to thank all other people in the TESOA-1 department, especially Maurice Martin, for their valuable feedback and for sharing their expertise.

I am thankful for my family who have always supported and encouraged me in the journey, from the very first weeks as a freshman until my graduation. Thank you to my friends in Germany who made the final year of my studies at the Bodensee an unforgettable experience. Finally, I want to thank all friends in Delft for their support during my thesis project.

Contents

Introduction

1.1. Asteroid research

Asteroids are minor bodies of the Solar System, with diameters varying from several meters to hundreds of kilometers. Asteroids can have irregular shapes and their surfaces are often scattered with irregularities such as boulders and slopes. Asteroids are part of the Near-Earth Objects (NEOs). By convention, NEOs are defined as "all small Solar System bodies with orbits around the Sun that lie partly between 0.983 and 1.3 astronomical units away from the Sun." [1]. There are over 600,000 known asteroids in our Solar System, of which more than 20000 are NEOs[1]. The interest in asteroids can be attributed to three general categories:

Scientific research. Asteroids have seen very little to no changes since their formation, making them excellent targets for research related to the origins of the Solar System. Asteroids are believed to have played major roles in the formation of planets [2, 3, 4].

Natural resources mining. Near-Earth objects could be mined to bring valuable resources back to Earth, which becomes increasingly relevant as resource depletion becomes a more pressing concern. There are still many technological and financial obstacles in the way of large-scale asteroid mining. The concept has been proven with several missions having successfully returned asteroid samples to Earth [5].

Planetary defence. NEOs with a diameter larger than 140 meters, and with orbits crossing Earth's orbit, are defined as Potentially Hazardous Objects (PHOs), most of which are asteroids [6]. The PHOs that currently cannot be ruled out as harmless are listed in NASA's Sentry Risk Table. As of March 2023, there are 24 items in this table[2]. An impact of a PHO with Earth could be disastrous and therefore planetary defence techniques are studied and developed. For example, NASA's Double Asteroid Redirection Test (DART) spacecraft recently struck an asteroid in an effort to study the interaction between the asteroid and a kinetic impactor [7, 8].

1.2. Navigation around asteroids

Missions to asteroids all require a navigation system that allows the spacecraft to safely approach the asteroid. Some missions go one step further and involve a form of physical interaction with the asteroid surface. For these applications, knowledge of the position, velocity, and attitude of the spacecraft with respect to the asteroid surface is essential. This thesis focuses on the determination of the position and velocity of a spacecraft in a binary asteroid environment.

1.2.1. Traditional asteroid navigation systems

The traditional method to determine the spacecraft position and velocity with respect to an inertial frame in deep space is to use radiometric tracking [9]. The orbit determination with radiometric tracking is performed using Earth-based ground stations and an antenna onboard the spacecraft. Radiometric tracking combined with a rough estimate of the asteroid's orbital state (ephemeris) in an inertial frame enables the spacecraft can navigate towards the asteroid. Once the spacecraft is at a distance of several thousands of kilometers,

---

[1]https://www.esa.int/Space_Safety/Near-Earth_Objects_-_NEO_Segment, last accessed 2023/03/31

[2]https://cneos.jpl.nasa.gov/sentry/, last accessed 2023/03/23

an orbit determination and characterisation phase is executed [10, 11]. Asteroid-relative measurements are obtained mainly using cameras and laser ranging instruments. These are combined with the spacecraft position and velocity knowledge given by the radiometric tracking and accelerometer data. This allows for the spacecraft to better characterize the orbital state of the asteroid, create a shape model of its irregular surface, to create a library of known landmarks on the surface, and to model the irregular gravity field.

For very close proximity operations below 10 km distance to the asteroid surface, often a form of landmark tracking is used in combination with Light Detection and Ranging (lidar) or laser range finders (LRFs) to determine the position and velocity of the spacecraft. Radiometric tracking is not an option at close range because of the round trip time of the signals to and from Earth. This is only possible by exploiting the knowledge obtained in the characterisation phase. ESA's Rosetta, JAXA's Hayabusa-2, and NASA's OSIRIS-REx missions all used such navigation concepts [12, 13, 14].

1.2.2. Challenges in asteroid navigation

The traditional asteroid navigation methods usually follow a similar approach that involves radiometric tracking for the faraway approach, followed by a characterization phase. Information from the characterization phase is then used to autonomously maneuver the spacecraft close to the asteroid, without relying on Earth-based communication.

A major challenge in the field of navigation around asteroids is to increase the level of autonomy of the spacecraft, especially its reliance on Earth-based radiometric tracking. Radiometric tracking is expensive, limits the safe operating envelope of the spacecraft. There is also a practical constraint on the number of spacecraft that can be supported by the Deep Space Network, which provides the radiometric tracking measurements. On top of all these arguments, radiometric tracking will often also not be available on smaller and cheaper spacecraft. These will have to navigate with a more limited set of sensors. Previous missions show that autonomous navigation is possible after an early characterization phase that heavily relied on radiometric tracking. A major challenge is to skip this expensive and time consuming early characterization phase.

Research in the past decades has focused on increasing the autonomy in asteroid missions. Optical navigation based on the line of sight a common topic of investigation [15, 16], which can also be combined with lidar measurements [17]. The extraction of the line of sight is impossible at very low altitudes because the asteroid fills too much space in the camera frame. A navigation system that includes a transition from line of sight navigation to landmark tracking is investigated in [18].

1.2.3. Recent research

Because of the ongoing interest in asteroids, many researchers study and develop navigation systems to operate spacecraft in the asteroid environment. Typically, the spacecraft combines optical measurements from cameras [19] and laser rangers [20] to estimate its position relative to the asteroid. The spacecraft attitude is determined using star trackers and rate gyros [21].

The images from navigation cameras can produce various measurements such as the line of sight (LOS) [22, 23], centroid and apparent diameter (CAD) [24, 25], and landmark tracking [19, 26, 27]. The type of measurement depends on the altitude and the camera field of view (FOV), with landmarks becoming smaller and smaller in the images as the altitude increases. In general, camera measurements suffer from range ambiguity. If multiple bodies can be observed by the camera(s), triangulation techniques can be used to indirectly provide range measurements [28, 29]. A formation of spacecraft can solve the range ambiguity problem with cameras alone, if interspacecraft measurements are available [30]. A common solution to solve the range ambiguity problem for a single spacecraft is to use a lidar or LRF in combination with the navigation cameras [23, 31].

Gil-Fernández (2018) shows that a spacecraft can autonomously navigate in a binary asteroid environment by solely observing the primary asteroid [32]. However, this requires augmenting the state vector with the gravitational parameter of the asteroid and the pointing error resulting from varying illumination conditions. Dietrich (2014) demonstrates that given an ellipsoid shape model for the asteroid, LRFs alone can be used to navigate the spacecraft [20]. They show that using more than three LRFs does not benefit the state estimation anymore, which is attributed to the geometry and symmetric nature of the ellipsoid surface. Takahashi (2021) proposes a navigation solution that is tightly coupled to the guidance algorithm, in the sense that impulsive ΔV maneuvers issued by the guidance are subsequently measured by onboard

accelerometers [33]. Integration of the accelerometer data then yields information about the position change over time.

1.2.4. Research context

The navigation system developed in this work is developed in the framework of the Near Earth Object Modelling and Payloads for Protection (NEO-MAPP) study[3] which uses ESA's Hera mission as a reference. The goal is to autonomously land a small spacecraft on Dimorphos, the smallest asteroid of the binary system (65803) Didymos. The small spacecraft is ejected from the Hera mothership and then autonomously navigates to a predefined landing position on the surface of Dimorphos. The spacecraft must therefore know its position in the asteroid reference frame. To save time and money, there will not be an early characterization phase in which a database of landmarks is collected along with a precise shape model. A separate navigation system is developed for the final phase of the landing. The only sensors that can be used for the navigation system are a single navigation camera, a single LRF, and accelerometers along all spacecraft axes. The attitude estimation hardware is not considered in this work.

1.3. Research formulation

This research will address the challenge of increased autonomy in asteroid navigation by developing and testing an autonomous navigation solution that relies on a simple set of sensors and little information about the appearance of the asteroid. The solution will be autonomous in the sense that the spacecraft determines its position and velocity with respect to the asteroid without any communication with Earth or any other spacecraft. The binary nature of the target asteroid system considered in this work gives an additional degree of freedom to design the navigation system, which will also be investigated in this work. The research objective that is central in this work is formulated as follows:

> **Research Objective**
>
> Investigate how an autonomous spacecraft can determine its absolute position and velocity in proximity of a binary asteroid by using vision-based navigation.

The research objective is split in several research questions that will be answered in this work. The first research question relates to the existing body of research that is available on the topic of asteroid navigation. This includes navigation systems that are not autonomous, such as the ones used in prior space missions.

> **Research Question 1**
>
> What is the state of the art of navigation around asteroids?

The second research question focuses on the simulated environment that is used to develop, test, and benchmark the developed navigation systems. The simulated environment plays a vital role in the development of the navigation system, and its composition and fidelity influences the validity of the results. The differences in the simulated environment must be taken into account when comparing results from different authors.

> **Research Question 2**
>
> What are the requirements for a simulator that can be used to develop the navigation system?

The prior knowledge that is required to estimate the spacecraft state with a given sensor suite can be provided in various ways. Common are Earth-based measurements from for instance radar imagery, or measurements taken during an early characterization phase. The level of prior knowledge that is required could impact the autonomy of the spacecraft, especially if this prior knowledge can only be obtained during an early characterization phase that relies on Earth-based measurements. Therefore, the third research

---

[3]`https://neomapp.eu/abstract/`, last accessed 2023/03/11

question is as follows:

> **Research Question 3**
>
> What prior knowledge about the asteroid environment is required to estimate the spacecraft state with a given sensor suite?

The performance requirements of the navigation system are a key consideration in the design of the navigation system. The design process is an iterative process in which the navigation system is tuned and modified to meet the requirements. The requirements themselves can also be iterated upon, especially in light of new findings with regards to the sensitivities of the navigation system that come with the development. A closer look at these requirements is taken by answering the fourth research question:

> **Research Question 4**
>
> What are the performance requirements for the navigation system, and how do these requirements change during the iterative design process?

Once the requirements are established, naturally the follow-up question is which navigation systems are capable of providing this required performance. There is no straightforward answer to this question, as the requirements themselves are determined in an iterative process that depends on the sensitivities of each method. This is investigated by answering the fifth research question:

> **Research Question 5**
>
> Which navigation systems can meet the performance requirements?

The final research question is related to a sensitivity study that is performed once a navigation filter is developed that fulfils the performance requirements in a default scenario. The binary asteroid environment is complex, with potentially challenging lighting conditions, irregular gravity fields, and other disturbances. The sensors are not perfect either, and the ejection from the mothership brings uncertainties in the navigation system as well. These effects are studied by answering the sixth research question:

> **Research Question 6**
>
> What are the key sensitivities of the developed navigation system?

1.4. Structure of the report

This report presents the findings of the research project that is created from the research objective and the subsequent research questions. The structure of the report is as follows: first, Chapter 2 presents the scientific article which covers the main findings of the research project. Next, Chapter 3 and Chapter 4 present the preliminary analysis which consists of the literature review and preliminary work on the simulator. Additional results that are relevant to the research objective but not part of the primary findings of the work are presented in Chapter 5. Chapter 6 discusses the verification and validation efforts that have been made, as well as those that are still recommended for future work. Finally, the conclusions of this work and recommendations for future work are given in Chapter 7.

Part I

Scientific Article

Autonomous Navigation for Binary Asteroid Landing

Peter Elffers*

TU-Delft Faculty of Aerospace Engineering, Kluyverweg 1, 2629 HS Delft, The Netherlands

This paper investigates the performance of an autonomous navigation system to navigate a spacecraft in the proximity of a binary asteroid system using optical and laser ranging measurements. The knowledge about the binary asteroid is limited to its orbital parameters and ellipsoid shape models. The accelerometer bias random walk is included in the estimation process. Over a four-hour landing maneuver starting from 6770 m altitude and ending at 550 m, the mean position estimation uncertainty is 41.6 m (3σ). It is shown that the navigation accuracy is sensitive to the Sun phase angle, the irregularity of the asteroid shape, and the goodness of fit of the ellipsoid shape model. The paper demonstrates that the navigation system is robust to large errors in the initialization of the extended Kalman filter state. The impact of image distortion and two types of image noise on the navigation performance are investigated.

I. Introduction

ASTEROIDS are gaining widespread attention from space agencies and industry because of their uniquely preserved environment since the formation of the Solar System, their potential for rare materials mining, and planetary defence purposes. Several missions dedicated to small bodies have been successfully launched and completed. In 2001, NASA's NEAR became the first spacecraft to orbit and land on an asteroid [1]. In 2010, JAXA successfully returned samples of the asteroid (25143) Itokawa with its Hayabusa-1 spacecraft [2], and ESA's Rosetta mission put a lander on the comet 67P/Churyumov-Gerasimenko in 2014 [3].

Because of the interest in asteroid exploration, many researchers have studied and developed navigation systems to safely operate spacecraft in the vicinity of asteroids. For proximity operations in missions that involve landings, autonomous navigation is required because of signal delays that come with Earth-based navigation. Typically, the spacecraft combines optical measurements from cameras [4] and laser rangers [5] to estimate its position relative to the asteroid. The spacecraft attitude is determined using star trackers and rate gyros [6].

The images from navigation cameras can produce various measurements such as the line of sight (LOS) [7, 8], centroid and apparent diameter (CAD) [9, 10], and landmark tracking [4, 11, 12]. The type of measurement depends on the altitude and the camera field of view (FOV), with landmarks becoming smaller in the images as the altitude increases. In general, camera measurements suffer from range ambiguity. CAD attempts to mitigate this issue by using a-priori knowledge about the size and shape of the asteroid and its projection onto the camera sensor. The lack of an accurate shape model combined with difficult lighting conditions makes it very difficult to estimate the radial range from optical measurements. If multiple bodies can be observed by the camera(s), triangulation techniques can be used to provide range measurements [13, 14]. A formation of spacecraft can solve the range ambiguity problem with cameras alone, if interspacecraft measurements are available [15]. A common solution to solve the range ambiguity problem for a single spacecraft is to use a Light Detection and Ranging (lidar) or laser range finders (LRFs) in combination with the navigation cameras [8, 16].

Gil-Fernández (2018) shows that a spacecraft can autonomously navigate in a binary asteroid environment by solely observing the primary asteroid [17]. However, this requires augmenting the state vector with the gravitational parameter of the asteroid and the pointing error resulting from varying illumination conditions. Dietrich (2014) demonstrates that given an ellipsoid shape model for the asteroid, LRFs alone can be used to navigate the spacecraft [5]. They show that using more than three LRFs does not benefit the state estimation anymore, which is attributed to the geometry and symmetric nature of the ellipsoid surface. Takahashi (2021) proposes a navigation solution that is tightly coupled to the guidance algorithm, in the sense that impulsive ΔV maneuvers issued by the guidance are subsequently measured by onboard accelerometers [18]. Integration of the accelerometer data then yields information about the spacecraft position change over time.

This paper investigates a navigation solution for a binary asteroid system that exploits measurements of both asteroids in the camera frame, similar to [13], combined with a single LRF measurement that uses ellipsoid models for the

---

*MSc. Student, Faculty of Aerospace Engineering, Control and Simulation Section, Delft University of Technology

asteroids in a manner similar to that in [5]. The navigation camera will provide LOS measurements, which are corrected for varying illumination conditions as is done in [17]. The intended use of the navigation solution is at medium to far distances because the LOS cannot be determined at very close distance when an asteroid fills the entire field of view of the camera. The contribution of this paper is a navigation filter that leverages the binary nature of the asteroid system in combination with a LRF. This navigation filter is robust to filter state initialization errors due to the high observability with both asteroids in sight, in combination with the LRF. Contrary to the landmark-based approaches, this approach only requires an ellipsoid shape model to determine the position relative to the asteroid.

This navigation system is developed in the framework of the NEO-MAPP study*, which uses ESA's Hera mission as a reference. The goal is to land a μLander on Dimorphos, the smallest asteroid of the binary system (65803) Didymos [19]. This μLander is detached from the Hera mothership at an altitude of around 5 km and navigates autonomously. The landing site for the μLander is a predefined point on the surface of Dimorphos. The spacecraft must therefore know its position in the asteroid reference frame. The requirement for the position knowledge is that the 3σ uncertainty in the position is less than 10% of the altitude. To save time and money, there will not be an early characterization phase in which a database of landmarks is collected along with a precise shape model, as is common practise in asteroid landing missions [2, 12]. A separate navigation system is developed for the final phase of the landing [20, 21]. Throughout the paper, the attitude control system is assumed to be a separate system, providing perfect pointing in the desired direction.

The paper is structured as follows: Sec. II gives an overview of the binary asteroid dynamics. Section III presents the onboard sensors, their mathematical models, and how they are used in the navigation system. The Extended Kalman Filter (EKF) development is described in Sec. IV, followed by an analysis and discussion of simulation results in Sec. V. The conclusions of the research and recommendations for future work are given in Sec. VI. Finally, in Appendix A the mathematics behind the LRF measurement model are described, and Appendix B shows a verification test for the LRF measurement model.

II. Dynamics

The dynamic environment around binary asteroids is one of the most complex environments found in the Solar System. This is due to the irregular shape and composition of the asteroids, combined with third-body perturbations, solar radiation pressure (SRP) and often short rotation periods. This section describes the modeling of the binary asteroid environment and its dynamics.

A. Target binary asteroid

Didymos consists of two asteroids named Didymos (primary) and Dimorphos (secondary). Throughout the paper, the naming of primary and secondary will be used. The asteroid characteristics, including ellipsoid shape models, are given in [22]. This description of Didymos is valid for its state before the impact of DART on 26 September 2023[†]. A summary of the most relevant parameters of Didymos is given in Table 1. The secondary asteroid is tidally locked with the primary.

Table 1   Main characteristics of binary asteroid Didymos [22].

| Property	Nominal value	Uncertainty (1σ)
Diameter of primary	780 m	±30 m
Diameter of secondary	164 m	±18 m
Density of primary	2170 kg/m^3	±350 kg/m^3
Orbit radius of secondary	1.19 km	±0.03 km
Total mass of system	5.278e11 kg	±0.54e11 kg
Rotation period of primary	2.2600 h	±0.0001 h
Secondary orbital period	11.9217 h	±0.0002 h
Spin pole of primary	Parallel to secondary orbital spin pole	
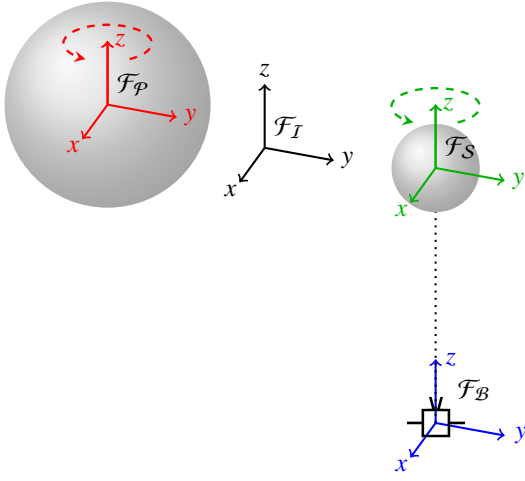
Fig. 1 Sketch of the four reference frames used in this paper. Dimensions are not to scale. Orientation of the asteroids is chosen arbitrarily.
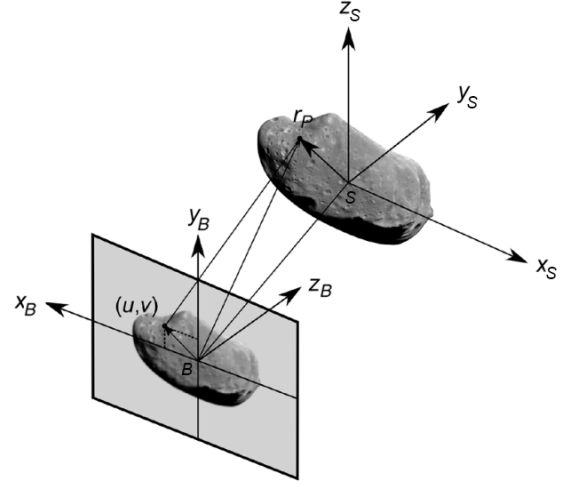
Fig. 2 Projection of a point P defined in the $\mathcal{F}_S$ frame onto the camera sensor in the $\mathcal{F}_B$ frame. Adapted from [8].

B. Reference frames

Four reference frames are used in this work: inertial, primary, secondary, and body. These frames are denoted by $\mathcal{F}_I$, $\mathcal{F}_P$, $\mathcal{F}_S$, and $\mathcal{F}_B$, respectively, and are shown in Fig. 1. The inertial frame is a modified J2000 frame, whose origin is in the binary system's barycenter. The axes of the inertial frame are aligned with the J2000 frame, meaning that the Z-axis points in the direction of the Earth mean rotation pole at epoch J2000, the X-axis points toward the mean equinox at epoch J2000, and the Y-axis completes the right-handed coordinate system. The primary and secondary reference frame have their origins in the centers of mass of the respective asteroids. Their Z-axes point in the direction of maximum moment of inertia, their X-axes in the direction of minimum moment of inertia, and their Y-axes complete the right-handed coordinate systems. The asteroids rotate around their Z-axes. The body frame is fixed to the spacecraft, with the Z-axis aligned with the camera line of sight, and the X- and Y-axes aligned with the camera sensor as shown in Fig. 2. The camera frame is assumed to coincide and align with the body frame and is therefore not mentioned separately. The LRF points along the Z-axis of $\mathcal{F}_B$, and is assumed to coincide with the origin of $\mathcal{F}_B$. The vector notation used in this paper is as follows: $\boldsymbol{r}_I^{SB}$ is a position vector from the origin of $\mathcal{F}_S$ to the origin of $\mathcal{F}_B$, defined in $\mathcal{F}_I$. $\boldsymbol{R}_{IB}$ is a direction cosine matrix that transforms a vector from $\mathcal{F}_B$ to $\mathcal{F}_I$.

C. Spacecraft translational dynamics

The translational dynamics are described in the $\mathcal{F}_I$ frame. The equations of motion are written as:

$$\dot{\boldsymbol{r}}_I^{IB} = \boldsymbol{v}_I^{IB} \tag{1}$$

$$\dot{\boldsymbol{v}}_I^{IB} = \boldsymbol{g}_I + \boldsymbol{a}_{\text{ext}} \tag{2}$$

where $\boldsymbol{r}$ is the position vector, $\boldsymbol{v}$ the velocity vector, $\boldsymbol{g}$ the gravity vector, and $\boldsymbol{a}_{\text{ext}}$ the external acceleration vector from sources other than gravity. The gravity and external acceleration vector will be examined in more detail.

1. Gravity field

The gravity field around asteroids is often highly irregular and as a result a point mass gravity model does not suffice. The spherical harmonics gravity model is a popular choice to precisely model a body's gravity field [23], however its convergence is limited to the body's circumscribing sphere [24]. The spherical harmonics model is therefore not suitable to simulate trajectories that reach within the circumscribing sphere, which is not an unlikely scenario when landing on an asteroid's surface. Alternatively, the polyhedron gravity model can be used to transform a 3D polyhedron

model into a gravity model, assuming a constant density [25]. The polyhedron gravity $\boldsymbol{g}_{\text{ast}}$, defined in the asteroid reference frame, is a summation over the edges and faces of the 3D polyhedron model:

$$\boldsymbol{g}_{\text{ast}} = \nabla U = -G\rho \sum_{e \in \text{ edges}} \boldsymbol{E}_e \boldsymbol{r}_e L_e + G\rho \sum_{f \in \text{ faces}} \boldsymbol{F}_f \boldsymbol{r}_f \omega_f \tag{3}$$

In this equation, U is the gravity potential, G is the gravitation constant, ρ is the mean density of the asteroid, $\boldsymbol{E}_e$ is a dyadic matrix of an edge, $\boldsymbol{r}_e$ and $\boldsymbol{r}_f$ are the distances from a point to an edge and a face, L_e is a dimensionless per-edge factor, $\boldsymbol{F}_f$ is an outer product of a face normal with itself, and ω_f is a dimensionless per-face factor.

For the 3D polyhedron models of the primary and secondary, modified versions of the asteroids Bennu and Itokawa are used. Their respective shape models have been determined during the OSIRIS-REx and Hayabusa-1 missions [26, 27]. This decision is motivated by the desire to have a simulated reality in the camera simulator that is more realistic than the ellipsoid shape models given in [22]. This comes with the benefit of testing the robustness of the developed algorithms on realistic shape models.

The 3D polyhedron models of Bennu and Itokawa are stretched to match the extent of the ellipsoid models along their principal axes of inertia. After calculating the volume of the reshaped 3D polyhedron models, the density of the two asteroids is recalculated to match the mass of the reshaped asteroids to the masses given in [22].

Third-body perturbations are neglected, as for altitudes below 5 km they are orders of magnitude smaller than the other accelerations such as that due to SRP, control acceleration, and gravitational pull.

2. External accelerations

The external accelerations that are simulated consist of the SRP and the guidance acceleration. The SRP due to the albedo of the asteroids is neglected. The constrained terminal velocity guidance algorithm is used to calculate the desired guidance acceleration [28]. The propulsion system dynamics are not considered, thus the calculated guidance acceleration is directly applied to a point mass model of the spacecraft.

A cannonball model is used to model the SRP. The cannonball model considers the spacecraft to be a sphere and as a result the attitude of the spacecraft is not part of the SRP calculation. An analysis on the impact of assuming a cannonball SRP model on the spacecraft dynamics in the vicinity of a binary asteroid environment is given in [29]. The acceleration due to SRP, perpendicular to the Sun direction, can be calculated as follows [30]:

$$\frac{ma_{\text{srp}}}{A_\perp} = \rho p_{\text{sun}} \tag{4}$$

where

$$p_{\text{sun}} = \frac{E}{c} = p_0 \left(\frac{r_\oplus}{r}\right)^2 \tag{5}$$

with

$\rho = 1.2$	[-]	assumed surface reflectivity
$c = 2.99792458 \times 10^8$	[m/s]	speed of light
$E = (1372 \pm 45)\left(\dfrac{r_\oplus}{r}\right)^2$	[W/m^2]	intensity of solar radiation (seasonal)
$p_0 = (4.58 \pm 0.15) \times 10^{-6}$	[N/m^2]	solar radiation pressure at 1 au (seasonal)
$r_\oplus = 1.4962 \times 10^8$	[km]	mean radius of Earth's orbit
$A_\perp = 1$	[m^2]	surface area of the spacecraft projected in the Sun direction

D. Spacecraft rotational dynamics

The rotational dynamics of the spacecraft are not modeled. The pointing knowledge of the spacecraft is assumed to be supplied by the GNC subsystem through a conventional star tracker and rate gyro setup. No pointing errors are taken into account.

E. Asteroid translational and rotational dynamics

The orbit of the asteroids and the Sun are modeled using the Hera SPICE kernels[‡]. The position and orientation of the Solar System bodies is returned in the J2000 reference frame.

III. Onboard sensors

The spacecraft is equipped with various onboard sensors essential for its operation. The characteristics of these sensors and how they are modeled is described here in more detail. The star trackers and gyros are not considered in this section because the attitude control and determination problem is assumed to be solved by a separate spacecraft subsystem. The remaining sensors are the accelerometers, the LRF, and the navigation camera.

A. Accelerometers

The accelerometers measure the proper acceleration of the spacecraft. The accelerometers are assumed to be perfectly aligned with the three axes of the $\mathcal{F}_\mathcal{B}$ frame. The accelerometer measurements $\boldsymbol{a}_{\text{meas},B}$ are subject to noise and bias random walk:

$$\boldsymbol{a}_{\text{meas},B}(t) = \boldsymbol{a}_B(t) + \boldsymbol{b}_{\text{acc},B}(t) + \boldsymbol{\eta}_{\text{acc}}(t) \tag{6}$$

where $\boldsymbol{b}_{\text{acc},B}$ is the bias random walk:

$$\dot{\boldsymbol{b}}_{\text{acc},B}(t) = \boldsymbol{\eta}_{\text{acc,bias}}(t) \tag{7}$$

In Eqs. (6) and (7), $\boldsymbol{\eta}_{\text{acc}}$ and $\boldsymbol{\eta}_{\text{acc,bias}}$ are zero-mean white noise vectors with standard deviations of 2.8284×10^{-4} m/s^2 and 2.8284×10^{-5} m/s^3, respectively. These values are conform the specifications of the accelerometers chosen by Airbus for the NEO-MAPP μLander.

B. Navigation camera

The navigation camera is used in combination with image processing to detect the location of the asteroid centroid in the image. Using this centroid location and a camera model, a unit vector towards the asteroid is calculated in the $\mathcal{F}_\mathcal{B}$ frame. The process is visualized in Fig. 2, where a point P on the asteroid is projected onto the camera sensor, yielding the pixel coordinates (u,v). A unit vector in the direction of P, defined in the $\mathcal{F}_\mathcal{B}$ frame, is then calculated using a camera model. This unit vector contains information about the relative direction of the asteroid with respect to the spacecraft, which can be used in the navigation filter.

1. Camera characteristics

The characteristics of the camera are given in Table 2. A virtual scene with the two asteroids is created in the Planet and Asteroid Natural Scene Generation Utility[§] (PANGU) [31]. The 3D models used for the asteroids are reshaped versions of Bennu and Itokawa, as explained in subsubsection II.C.1. PANGU runs inside of the MATLAB/Simulink® simulator. The inputs for PANGU are the Sun position, asteroids positions and orientations, and the spacecraft position and orientation. Two example images that are rendered in PANGU are shown in Figs. 3 and 4.

Table 2   Characteristics of the navigation camera

Property	Value
Resolution	512x512 px
Focal length f	50 mm
Field of view	30°
Pixel size h_{px}	0.052 $\times 10^{-3}$ m/px
Pixel angular size h_{cam}	0.0010 rad/px

[‡]http://spiftp.esac.esa.int/data/SPICE/hera/misc/hera.html, last accessed 2023/03/13
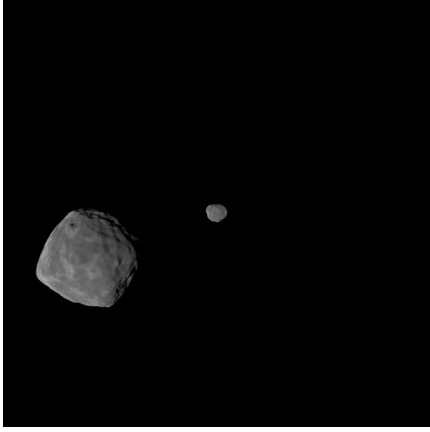[§]https://pangu.software/, last accessed 2023/03/15

Fig. 3 Navigation camera output at 6500 m distance from the surface of the secondary. Own work, rendered in PANGU.
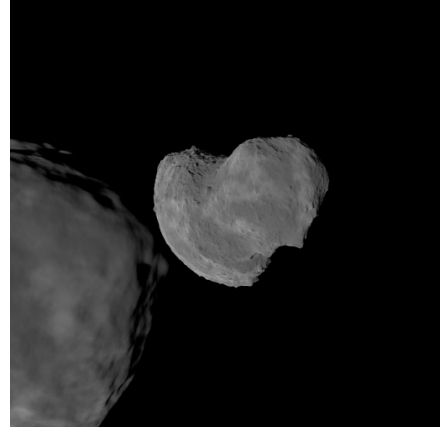

Fig. 4 Navigation camera output at 500 m distance from the surface of the secondary. Own work, rendered in PANGU.

2. Camera model

A camera model is used to extract spatial information from the images. An example is given in Fig. 2, where a point P is projected onto the camera sensor. The inverse is also possible: given the pixel coordinates (u,v), a unit direction vector can be calculated. All points in the direction of this vector project to the pixel coordinates (u,v). The pinhole camera model [32] is used to calculate the pixel coordinates associated with the projection of a point P defined in $\mathcal{F}_\mathcal{B}$:

$$\begin{pmatrix} u \\ v \end{pmatrix} = \frac{f}{h_{\text{px}} Z_B^{BP}} \begin{pmatrix} X_B^{BP} \\ Y_B^{BP} \end{pmatrix} \tag{8}$$

3. Image processing

The camera images are processed to extract the centroid locations of the asteroids in pixel coordinates. These centroids are then used as measurements in the navigation filter. The centroid extraction procedure is challenging due to varying illumination conditions, overlapping asteroids, asteroids that are (partially) out of the image, and irregular shapes. Furthermore, the centroids must be assigned the correct label 'primary' or 'secondary'. In the framework of the image processing, two terms are defined:

Center of figure (cof): the projection of the center of mass (com) of the asteroid onto the camera sensor, in pixel coordinates.

Center of brightness (cob): the centroid of a region of pixels that is detected in the image, in pixel coordinates.

The motion of the center of mass of the asteroids is described in the SPICE kernels. Therefore, ideally we measure the center of figure, as this gives the direction towards a known point in inertial space. However, due to varying lighting conditions casting shadows on the asteroid surface, and irregular asteroid shapes, this is not possible. For example, in Fig. 3 the larger asteroid has a shadow region on the right side, which moves the center of brightness location to the left relative to the center of figure. To mitigate this discrepancy between the center of figure and center of brightness, [17] proposes a factor ε_{cob} that corrects for the changing illumination conditions by shifting the center of brightness in the direction opposite of the Sun direction in the camera frame. The definition of the correction factor and the subsequent correction to obtain an estimate for the center of figure are given by[¶]:

$$\varepsilon_{\text{cob}} = \arctan\left(\frac{8\pi R}{3r}\sin^2\left(\frac{\phi}{2}\right)\right)\frac{\boldsymbol{u}_{\text{det}}}{h_{\text{cam}}} \tag{9}$$

$$\hat{\boldsymbol{p}}_{\text{cof}} = \boldsymbol{\varepsilon}_{\text{cob}} + \boldsymbol{p}_{\text{cob}} \tag{10}$$

[¶]Private communication with Jesus Gil-Fernandez, the author of [17], resulted in a slightly modified equation for ε_{cob} than what is written in his paper. Date: 2022/12/01
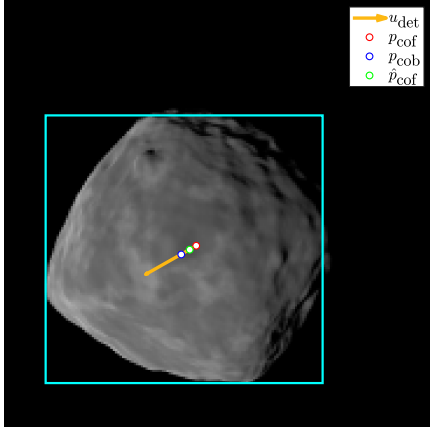
Fig. 5 Key concepts from the image processing. Note that p_{cob} is shifted in the direction opposite of u_{det} to obtain $\hat{p}_{\mathrm{cof}}$.
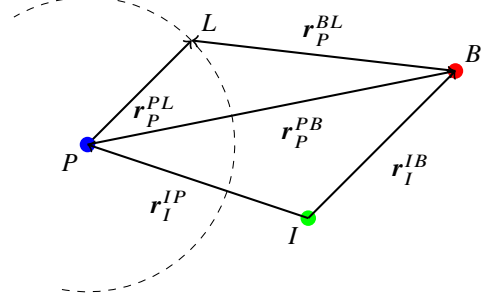

Fig. 6 Sketch of the LRF beam r_P^{BL} intersecting the surface of asteroid P in the point L. Also shown are the position of P and B in the I-frame.

with

$\varepsilon_{\mathrm{cob}}$	[px]	lighting conditions correction factor
$\hat{p}_{\mathrm{cof}}$	[px]	estimated center of figure pixel coordinates
p_{cob}	[px]	center of brightness pixel coordinates
R	[m]	mean radius of asteroid
r	[m]	spacecraft position norm in asteroid-fixed reference frame
ϕ	[rad]	Sun phase angle
u_{det}	[m]	unit vector of Sun direction in camera sensor plane
$h_{\mathrm{cam}} = 0.0010$	[rad/px]	pixel angular size

The correction procedure is visualized in Fig. 5. A limitation of $\varepsilon_{\mathrm{cob}}$ is that in its derivation, a spherical shape is assumed. Therefore, the correction will be less effective or even harm the estimation of $\hat{p}_{\mathrm{cof}}$ if the asteroid shape is non-spherical. For this reason, the correction is only applied to the primary asteroid, but not to the secondary asteroid. All steps of the image processing algorithm are given in Algorithm 1.

Algorithm 1 Image processing

1: Convert the image to grayscale.
2: Binarize the image. Every grayscale pixel is converted to either 1 (white) or 0 (black). The threshold that determines to which group a pixel belongs is set using Otsu's method [33].
3: Fill holes in the image. A hole is defined as a set of background pixels that cannot be reached by filling in the background from the edge of the image.
4: Extract the area, centroid location, and bounding box of each 8-connected object in the binary image.
5: Assign the label 'primary' or 'secondary' to each detected object based on the minimum distance between the object centroid and the predicted projection of the primary and secondary center of mass.
6: Sort the objects within the primary and secondary lists by their area. Select the largest two objects from each list.
7: Apply the Sun phase angle correction $\varepsilon_{\mathrm{cob}}$ to the largest object corresponding to the primary asteroid.
8: Discard the objects if their bounding boxes overlap each other. Stop simulation.
9: Discard objects if their bounding box touches the edges of the frame.
10: Discard all measurements if the distance between two consecutive $\hat{p}_{\mathrm{cof}}$ is beyond a threshold value.

The output of the image processing is either one or two sets of pixel coordinates that represent a center of figure, or a zero output. The logic that determines the subsequent steps, which ultimately leads to exploiting the measurement to gain knowledge about the system state, is included in the navigation filter.

C. Laser range finder

The LRF points in the same direction as the camera, the Z-axis of $\mathcal{F}_\mathcal{B}$, and provides a distance measurement to a point on the surface of the asteroid. The distance r_{LRF} measured by the LRF between the spacecraft and a point L on the surface of the primary asteroid is sketched in Fig. 6 and is expressed as:

$$r_{\text{LRF}} = \left\| \boldsymbol{r}_P^{PL} - \boldsymbol{r}_P^{PB} \right\| \tag{11}$$

The measurement is obtained using PANGU and uses the reshaped 3D models of Bennu and Itokawa. If there would be a pointing error, this is directly reflected in the measurement from PANGU.

IV. Extended Kalman Filter development

This section presents the navigation concept that is implemented using an EKF, the EKF state vector, and the propagation and measurement update steps of the EKF. Directly following the EKF development is a description of the reference landing scenario, the initial setup and tuning of the EKF, and the verification and validation procedure for the simulator and the EKF.

A. Navigation concept

The navigation concept is to autonomously navigate in the binary asteroid environment by combining prior knowledge with onboard measurements. The prior knowledge consists of the ellipsoid shape models, point mass gravity fields, the ephemeris of the asteroids given by the SPICE kernels, and spacecraft parameters. The onboard measurements are obtained by the accelerometers, the camera, and the laser range finder. The camera and laser range finder yield measurements that are relative to the asteroids. Using the ephemeris and (known) attitude, these measurements can be used to estimate the position and velocity of the spacecraft in inertial space. Measurements of both asteroids are used to exploit the binary nature of the asteroid system to provide a better state estimate.

B. State vector definition

The camera and LRF measurements can be relative to both the primary and the secondary asteroid. The camera can provide two measurements, one to each asteroid, if both asteroids are in the image. It is favorable to define the position and velocity in the state vector in the $\mathcal{F}_\mathcal{I}$ frame because measurements from both the primary and secondary asteroid can be easily transformed into the $\mathcal{F}_\mathcal{I}$ frame through the SPICE kernel ephemeris. The state vector consists of the position and velocity of the spacecraft in the $\mathcal{F}_\mathcal{I}$ frame, and the accelerometer bias random walk in the $\mathcal{F}_\mathcal{B}$ frame, as defined in Eqs. (6) and (7). The bias random walk $\boldsymbol{b}_{\text{acc},B}$ is also called the accelerometer bias. The state vector is thus as follows:

$$\boldsymbol{x} = \begin{pmatrix} \boldsymbol{r}_I^{IB} & \dot{\boldsymbol{r}}_I^{IB} & \boldsymbol{b}_{\text{acc},B} \end{pmatrix}^T = \begin{pmatrix} r_{I,x}^{IB} & r_{I,y}^{IB} & r_{I,z}^{IB} & \dot{r}_{I,x}^{IB} & \dot{r}_{I,y}^{IB} & \dot{r}_{I,z}^{IB} & b_{\text{acc},B,x} & b_{\text{acc},B,y} & b_{\text{acc},B,z} \end{pmatrix}^T \tag{12}$$

C. Propagation

The true inertial acceleration of the spacecraft is unknown. Therefore, the measured acceleration, corrected for the accelerometer bias, is used in the filter. The uncertainty in this measurement is included in the propagation equation through the $\boldsymbol{G}$ matrix and the input noise vector ω. Point mass gravity models are used to lower the complexity of the model that is run onboard of the spacecraft. The nonlinear propagation equation is as follows:

$$\dot{\boldsymbol{x}} = f(\boldsymbol{x}, \boldsymbol{u}) + \boldsymbol{G}\omega = \begin{pmatrix} \dot{\boldsymbol{r}}_I^{IB} \\ \ddot{\boldsymbol{r}}_I^{IB} \\ \dot{\boldsymbol{b}}_{\text{acc},B} \end{pmatrix} + \boldsymbol{G} \begin{pmatrix} \boldsymbol{\eta}_{\text{acc}} \\ \boldsymbol{\eta}_{\text{acc,bias}} \end{pmatrix} =$$

$$\begin{pmatrix} \dot{\boldsymbol{r}}_I^{IB} \\ -\mu_p \dfrac{\boldsymbol{r}_I^{IB} - \boldsymbol{r}_I^{IP}}{|\boldsymbol{r}_I^{IB} - \boldsymbol{r}_I^{IP}|^3} - \mu_s \dfrac{\boldsymbol{r}_I^{IB} - \boldsymbol{r}_I^{IS}}{|\boldsymbol{r}_I^{IB} - \boldsymbol{r}_I^{IS}|^3} + \boldsymbol{R}_{IB}(\boldsymbol{a}_{\text{meas},B} - \boldsymbol{b}_{\text{acc},B}) \\ \boldsymbol{0}_{3x1} \end{pmatrix} + \begin{bmatrix} \boldsymbol{0}_{3x3} & \boldsymbol{0}_{3x3} \\ -\boldsymbol{R}_{IB} & \boldsymbol{0}_{3x3} \\ \boldsymbol{0}_{3x3} & \boldsymbol{I}_{3x3} \end{bmatrix} \begin{pmatrix} \boldsymbol{\eta}_{\text{acc}} \\ \boldsymbol{\eta}_{\text{acc,bias}} \end{pmatrix} \tag{13}$$

14

To propagate the state estimation error covariance matrix $\boldsymbol{P}$ of the EKF, the Jacobian of the state derivative is used. It is given by Eq. (14). The term $\frac{\partial \ddot{\boldsymbol{r}}_I^{IB}}{\partial \boldsymbol{r}_I^{IB}}$ is the gravity gradient and is found in [34].

$$
\boldsymbol{F}_x = \frac{\partial f(\boldsymbol{x}, \boldsymbol{u})}{\partial \boldsymbol{x}} = \frac{\partial}{\partial \boldsymbol{x}} \left(-\mu_p \frac{\boldsymbol{r}_I^{IB} - \boldsymbol{r}_I^{IP}}{|\boldsymbol{r}_I^{IB} - \boldsymbol{r}_I^{IP}|^3} - \mu_s \frac{\boldsymbol{r}_I^{IB} - \boldsymbol{r}_I^{IS}}{|\boldsymbol{r}_I^{IB} - \boldsymbol{r}_I^{IS}|^3} + \boldsymbol{R}_{IB}(\boldsymbol{a}_{\text{meas},B} - \boldsymbol{b}_{\text{acc},B}) \atop \boldsymbol{0}_{3x1} \right) = \begin{bmatrix} \boldsymbol{0}_{3x3} & \boldsymbol{I}_{3x3} & \boldsymbol{0}_{3x3} \\ \frac{\partial \ddot{\boldsymbol{r}}_I^{IB}}{\partial \boldsymbol{r}_I^{IB}} & \boldsymbol{0}_{3x3} & -\boldsymbol{R}_{IB} \\ \boldsymbol{0}_{3x3} & \boldsymbol{0}_{3x3} & \boldsymbol{0}_{3x3} \end{bmatrix}
$$

(14)

Finally, the process noise covariance matrix $\boldsymbol{Q}$ is created using the accelerometer noise and bias covariances:

$$
\boldsymbol{Q} = \begin{bmatrix} \sigma_{\text{acc}}^2 & \boldsymbol{0}_{3x3} \\ \boldsymbol{0}_{3x3} & \sigma_{\text{acc,bias}}^2 \end{bmatrix}
$$

(15)

D. Measurement update

The measurement update step includes the Kalman gain calculation, the measurement update itself, and the update of the state estimation error covariance matrix $\boldsymbol{P}$. An essential part in these calculations is the function $z = h(\boldsymbol{x}, \boldsymbol{u})$, which calculates the measurement z that corresponds to the state $\boldsymbol{x}$ and input $\boldsymbol{u}$. The Jacobian of $h(\boldsymbol{x}, \boldsymbol{u})$, called $\boldsymbol{H}_x$, is used in the Kalman gain calculation and in the update of $\boldsymbol{P}$. The measurements that must be calculated are the pixel coordinates of the expected center of figures of the asteroids, and the expected distance to the asteroid surface measured by the LRF. The measurement updates for the camera and LRF are performed separate from one another. Details on the measurement update for the camera and the LRF are given below.

1. Camera update

For every image that the camera outputs, the image processing determines how many asteroids are in the image. If no asteroids are found, no measurement update is executed. If one or two asteroids are found, z will be of size 2x1 or 4x1. In the following, it is assumed that only the primary asteroid is detected by the image processing.

The image processing outputs $\hat{\boldsymbol{p}}_{\text{cof}}$, the estimated center of figure of the primary asteroid in pixel coordinates. To calculate the measurement that is expected given the current state estimate $\hat{\boldsymbol{x}}_{\text{filter}}$, $z = h(\boldsymbol{x}, \boldsymbol{u})$ is used. The knowledge of the ephemeris of the asteroid through its SPICE kernel, which gives the center of mass location of the primary asteroid in $\mathcal{F}_I$, is used in the calculation of $z = h(\boldsymbol{x}, \boldsymbol{u})$ as well. This center of mass location must now be projected onto the camera sensor as shown in Fig. 2. First, it must be transformed into the $\mathcal{F}_B$ frame. This is done as follows:

$$
\boldsymbol{r}_B^{BP} = \boldsymbol{R}_{BI}(\boldsymbol{r}_I^{IP} - \boldsymbol{r}_I^{IB})
$$

(16)

where $\boldsymbol{R}_{BI}$ and $\boldsymbol{r}_I^{IP}$ are given by the SPICE kernel, and $\boldsymbol{r}_I^{IB}$ is part of $\hat{\boldsymbol{x}}_{\text{filter}}$. The next step is to use the pinhole camera model, Eq. (8), to calculate the pixel coordinates corresponding to the projection of $\boldsymbol{r}_B^{BP}$ onto the camera sensor. The coordinates are shifted by 256 pixels to transform them to the image coordinate system, because in the image coordinate system (0,0) is at the image border while in the pinhole model it is at the center of the image. The resulting equation is:

$$
z = h(\boldsymbol{x}, \boldsymbol{u}) = \boldsymbol{p}_{\text{cof}} = \frac{f}{h_{\text{px}} Z_B^{BP}} \begin{pmatrix} X_B^{BP} \\ Y_B^{BP} \end{pmatrix} + \begin{pmatrix} 256 \text{ px} \\ 256 \text{ px} \end{pmatrix}
$$

(17)

Now to find $\boldsymbol{H}_x$, the Jacobian of $h(\boldsymbol{x}, \boldsymbol{u})$ is calculated:

$$
\boldsymbol{H}_x = \frac{\partial h(\boldsymbol{x}, \boldsymbol{u})}{\partial \boldsymbol{x}} = \begin{bmatrix} \frac{\partial h(\boldsymbol{x}, \boldsymbol{u})}{\partial \boldsymbol{r}_I^{IB}} & \boldsymbol{0}_{2x3} & \boldsymbol{0}_{2x3} \end{bmatrix}
$$

(18)

Now the chain rule is applied, using Eq. (16) this results in:

$$
\frac{\partial h(\boldsymbol{x}, \boldsymbol{u})}{\partial \boldsymbol{r}_I^{IB}} = \frac{\partial h(\boldsymbol{x}, \boldsymbol{u})}{\partial \boldsymbol{r}_B^{BP}} \frac{\partial \boldsymbol{r}_B^{BP}}{\partial \boldsymbol{r}_I^{IB}} = \frac{\partial h(\boldsymbol{x}, \boldsymbol{u})}{\partial \boldsymbol{r}_B^{BP}} (-\boldsymbol{R}_{BI})
$$

(19)

15

working out the partial derivative gives:

$$\frac{\partial h(\boldsymbol{x}, \boldsymbol{u})}{\partial \boldsymbol{r}_B^{BP}} = \begin{bmatrix} \dfrac{f}{Z_B^{BP} h_{\text{px}}} & 0 & -\dfrac{f X_B^{BP}}{(Z_B^{BP})^2 h_{\text{px}}} \\ 0 & \dfrac{f}{Z_B^{BP} h_{\text{px}}} & -\dfrac{f Y_B^{BP}}{(Z_B^{BP})^2 h_{\text{px}}} \end{bmatrix} \tag{20}$$

The sensor noise covariance matrix $\boldsymbol{R}$ depends on the number of measurements that is found after the image processing is performed. In the case that only one measurement is found, the measurement vector consists of two pixel values for $\hat{\boldsymbol{p}}_{\text{cof}}$. The $\boldsymbol{R}$-matrix is then as follows:

$$\boldsymbol{R} = \begin{bmatrix} \sigma_{\text{cam}}^2 & 0 \\ 0 & \sigma_{\text{cam}}^2 \end{bmatrix} \tag{21}$$

2. Laser range finder update

The LRF update is only performed if a valid LRF measurement is obtained from PANGU. Equation (11) is used to calculate the expected LRF measurement given the current state estimate $\hat{\boldsymbol{x}}_{\text{filter}}$. The main challenge here is to obtain $\boldsymbol{r}_P^{PL}$, the vector from the center of the asteroid to the LRF contact point L, as sketched in Fig. 6. For this calculation, the ellipsoid shape model is used. This is not a perfect match for the true shape model, but it is assumed to be the best available shape model given the prior knowledge. The intersection of the Z-axis of $\mathcal{F}_B$ and the ellipsoid is calculated. This calculation is derived in Appendix A.

The Jacobian is calculated as follows. First, the part in Eq. (11) that depends on the filter state $\boldsymbol{x}$ is identified to be $\boldsymbol{r}_P^{PB}$, related to the filter state through $\boldsymbol{r}_I^{IB}$:

$$\boldsymbol{r}_P^{PB} = \boldsymbol{R}_{PI}(\boldsymbol{r}_I^{IB} - \boldsymbol{r}_I^{IP}) \tag{22}$$

The measurement equation $z = h(\boldsymbol{x}, \boldsymbol{u})$ for the LRF is given in Eq. (11). The Jacobian of this equation is then:

$$\boldsymbol{H}_x = \frac{\partial h(\boldsymbol{x}, \boldsymbol{u})}{\partial \boldsymbol{x}} = \begin{bmatrix} \dfrac{\partial h(\boldsymbol{x}, \boldsymbol{u})}{\partial \boldsymbol{r}_I^{IB}} & \boldsymbol{0}_{1x3} & \boldsymbol{0}_{1x3} \end{bmatrix} \tag{23}$$

Now the chain rule is applied:

$$\frac{\partial h(\boldsymbol{x}, \boldsymbol{u})}{\partial \boldsymbol{r}_I^{IB}} = \frac{\partial h(\boldsymbol{x}, \boldsymbol{u})}{\partial \boldsymbol{r}_B^{PB}} \frac{\partial \boldsymbol{r}_B^{PB}}{\partial \boldsymbol{r}_I^{IB}} = \frac{\partial h(\boldsymbol{x}, \boldsymbol{u})}{\partial \boldsymbol{r}_B^{PB}} \boldsymbol{R}_{PI} \tag{24}$$

The remaining partial derivative to complete the Jacobian is given by:

$$\frac{\partial h(\boldsymbol{x}, \boldsymbol{u})}{\partial \boldsymbol{r}_B^{PB}} = \frac{\partial \left\| \boldsymbol{r}_P^{PL} - \boldsymbol{r}_P^{PB} \right\|}{\partial \boldsymbol{r}_B^{PB}} = \frac{\boldsymbol{r}_P^{PL} - \boldsymbol{r}_P^{PB}}{\left\| \boldsymbol{r}_P^{PL} - \boldsymbol{r}_P^{PB} \right\|} \tag{25}$$

The sensor noise covariance matrix $\boldsymbol{R}$ represents the uncertainty in the LRF measurement, which is one-dimensional: $R = \sigma_{\text{LRF}}^2$.

E. Reference landing scenario

Now that the EKF is complete, a reference landing scenario is defined. The nominal flight time is 4 hours and the starting position is about 6770 m above the surface of the secondary asteroid. The starting position is in the plane of rotation of the secondary around the primary. The target position that is reached after 4 hours is 300 m above the outward facing pole of the secondary. This infers that somewhere along the trajectory, the primary will appear behind the secondary (Fig. 4), triggering a shutdown of the simulation. The reference trajectory is chosen such that this overlapping of the two bodies in the image only occurs at the very final moments of the simulation when the spacecraft is around 550 m above the surface. By default, the camera and LRF are always pointed at the secondary asteroid. The reference trajectory of the spacecraft is shown in Fig. 7, together with the movement of the asteroids and the Sun direction. The shadow projection onto the YZ-plane shows that the motion of the asteroids and spacecraft is in the plane of rotation of the binary system.
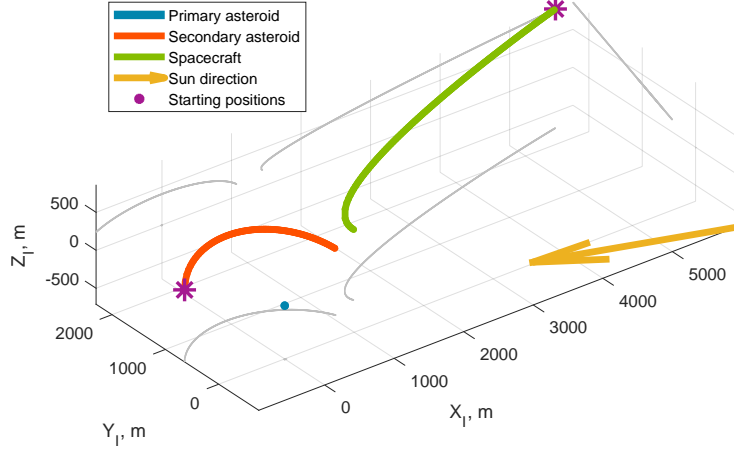
Fig. 7 Trajectory of the primary, secondary, and the spacecraft in the reference landing scenario. Note that the illumination conditions are favorable due to the low Sun phase angles.

F. Initial filter setup and tuning

The initial filter setup and tuning consists of three parts. First, the tuning of the Q- and R-matrices, the initial P-matrix, and the initial filter state are described. Then, the consistency of the filter is verified and typical performance characteristics of the filter are identified. Finally, the effects of various pointing directions for the camera and LRF are examined, followed by a summary of the default EKF configuration after tuning.

1. Filter tuning

The filter tuning process is an iterative process in which the tuning parameters are changed to satisfy the requirements. In this process, the sensitivities of the filter become clear, leading to additional information that is used in the tuning process. The requirement for the position knowledge is that the 3σ uncertainty in the position is less than 10% of the altitude.

The filter state is initialized with the true values of the states, meaning that there is initially no state estimation error. The state estimation error is defined as:

$$\Delta = x_{\text{true}} - \hat{x}_{\text{filter}} \tag{26}$$

For the process noise covariance matrix Q, the previously mentioned values of $\sigma_{\text{acc}} = 2.8284 \times 10^{-4}$ m/s² and $\sigma_{\text{acc,bias}} = 2.8284 \times 10^{-5}$ m/s³ are used as a first guess. The results with these values are satisfactory and no further tuning is performed. For the sensor noise covariance matrix R, trial and error shows that values of 10 px for σ_{cam} and 15 m for σ_{LRF} give good performance. The state estimation error stays well within the 3σ bounds for the majority of the simulation time and the initial convergence time is around 200 s. For the initialization of the state estimation error covariance matrix P, trial and error is used to find a matrix that allows the EKF to quickly converge, without allowing the state estimation error to escape the predicted 3σ bounds. This results in the following matrix:

$$P_0 = \begin{bmatrix} \sigma_{\text{pos},0}^2 & \mathbf{0}_{3x3} & \mathbf{0}_{3x3} \\ \mathbf{0}_{3x3} & \sigma_{\text{vel},0}^2 & \mathbf{0}_{3x3} \\ \mathbf{0}_{3x3} & \mathbf{0}_{3x3} & \sigma_{\text{acc,bias},0}^2 \end{bmatrix} \tag{27}$$

with $\sigma_{\text{pos},0} = 8$ m, $\sigma_{\text{vel},0} = 0.1$ m/s, and $\sigma_{\text{acc,bias},0} = 0.005$ m/s². The requirement on the 3σ uncertainty in the position is met for the reference trajectory.

2. Filter consistency and performance characteristics

A consistent state estimator must satisfy two requirements: the estimation errors (i) are zero-mean, and (ii) have a covariance matrix smaller or equal to the one calculated by the filter [35]. To test the developed EKF for consistency,

ideal measurements are generated for the LRF using Eq. (11) and for the camera using Eq. (17). This is done by feeding knowledge of the true system state from the simulator into these equations. To these ideal measurements, zero-mean white noise with known variance is added. The EKF is then given these variances through the $\boldsymbol{R}$-matrix. The filter output must then satisfy the two requirements associated with a consistent state estimator.

More realistic measurements are introduced in two steps. First, the ideal camera measurement is replaced by the PANGU images and subsequent image processing. The effect of this change on the position estimation error is shown in Fig. 8. Several observations can be made from this figure:

1) The EKF is consistent when ideal measurements with known noise characteristics are used. Calculations show that the error signal mean is close to zero: 2 m, 0.02 m/s, and 3×10^{-5} m/s^2, for the position, velocity, and accelerometer bias signal components. The estimation error statistics are in agreement with the EKF's calculated covariances. Only two simulations with idealized measurements are done in this work. While both simulations suggest that the filter is consistent, more simulations are required to make a definitive statement about the consistency of the EKF.

2) The flight trajectory is such that for the majority of the flight, especially the first 8000 seconds, the LRF and camera are pointed along the negative X-axis of $\mathcal{F}_\mathcal{I}$. The LRF is responsible for most of the state estimation in this direction. Therefore, introducing the camera measurements from PANGU has little effect on the position estimation error in the X-direction.

3) The position estimation errors are smaller in the X-direction compared to the Y- and Z-direction. This is because the LRF is more accurate than the (indirect) distance measurements from the camera images.

4) Note the jump in the 3σ bounds around 2800 seconds, best visible in the position estimation error for the Y-direction. This is due to the loss of visibility of the primary asteroid. As the measurement is lost, the uncertainty in the state estimate increases again.

5) The 3σ bounds along the Y- and Z-direction, which are determined mainly by the camera measurements, keep converging as the spacecraft comes closer to the asteroid. This behavior can be explained as follows: imagine observing an asteroid at 6 km distance, with the camera pointed at the exact center of brightness of the asteroid. If the asteroid now moves 10 px in the image frame, the asteroid would have to move a large distance to make this shift. Repeat the same experiment now with an asteroid at 600 m distance. The distance that the asteroid needs to move to achieve this 10 px shift is now much smaller. In other words, the estimation error in meters, associated with a 10 px uncertainty, gets lower and lower as the distance to the observed object decreases.

6) The estimation error starts to escape the 3σ bounds in the final part of the simulation. This is caused by errors in the image processing that are becoming increasingly large as the irregularly shaped object gets closer. Take for example Fig. 4. The center of brightness of the secondary asteroid will be very far off the true center of figure, causing these errors.

The next development step is to introduce the LRF measurement from PANGU. The result of this step is shown in Fig. 9. We see that the estimation error in the X-direction has increased with the implementation of the PANGU LRF measurement. This is caused by the mismatch between the LRF measurement and the ellipsoid model used in $z = h(\boldsymbol{x}, \boldsymbol{u})$.

3. Pointing direction tuning

To understand which camera/LRF pointing strategy yields the best results, three tests are executed. The camera/LRF pointing is chosen to be either primary, secondary, or at the midpoint in between the two asteroids. Because the goal is to land the spacecraft on the secondary, the spacecraft will always re-point to the secondary in the final phase of flight. The switching point is determined by the image processing: once one of the two asteroids is lost out of sight, the spacecraft reorients itself to point to the secondary asteroid. This maneuver is implemented as an instant change of attitude.

Pointing either primary and then secondary, or always pointing secondary, yields similar results. Pointing secondary is the preferred option as fewer maneuvers are required. The results of pointing at the midpoint, compared to pointing secondary, are shown in Figs. 10 and 11. Several observations are made:

1) The state estimation errors in the X-direction are much larger when pointing at the midpoint. This is due to the loss of the LRF when pointing at the midpoint between the asteroids. From the two camera measurements, the distance to the asteroids can still be determined, although less accurate than with the LRF.

2) The timestep that an asteroid is lost out of sight and the spacecraft reorients to point secondary is delayed, from around 2800 seconds when pointing secondary to 8600 seconds when pointing at the midpoint.

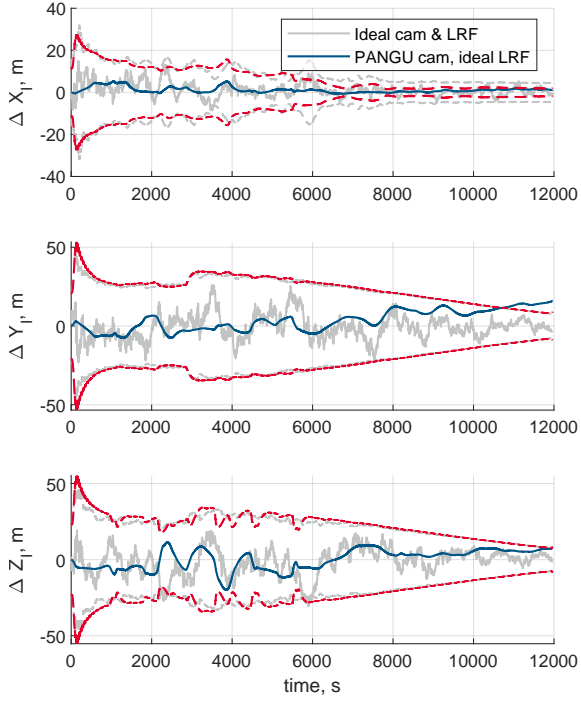3) After the reorientation maneuver, the two curves overlap. This is expected, as the measurements and trajectory

18

Fig. 8 *I*-frame position estimation errors, including error 3σ bounds. Ideal camera measurements compared to PANGU.
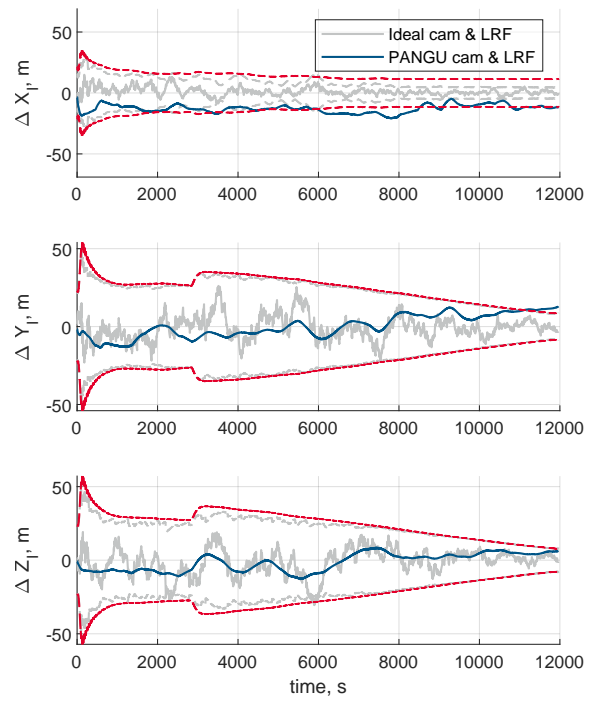
Fig. 9 *I*-frame position estimation errors, including error 3σ bounds. Ideal measurements compared to PANGU camera and LRF measurements.

are the same for both simulations.

The key outcome of this test is that while navigation without the LRF is not preferred due to the larger state estimation errors, it can be used as a back-up if the LRF fails, or in an orientation phase where the spacecraft changes its pointing such that the LRF is not always available.

4. Navigation filter default configuration

The default configuration for the navigation filter that is established after this initial testing phase is given in Table 3.

G. Verification and validation

Verification and validation is done to make sure that the models are implemented correctly, and to check that the produced results match reality. Several steps are taken to verify the results in this work. Validation is left as a recommendation for future work. Examples of verification efforts are: the polyhedron gravity field is verified to approach a point mass model at far distances, the SPICE kernel is verified to output orbits in accordance with [22], the EKF consistency is checked, the LRF ellipsoid model is compared to the PANGU LRF output for a full rotation around the asteroid to verify the correct orientation and dimensions of the ellipsoid model, and the image processing is validated with numerous edge-cases. The PANGU LRF verification is shown in more detail in Appendix B.

V. Results

This section extends on the results from the previous section by testing the behavior of the EKF in three different ways. First, the sensitivity to the initial position of the spacecraft is studied, followed by an analysis on how the EKF responds to errors in the initialization of the filter state, a very relevant test because the deployment from the mothership is imperfect and demands some robustness of the navigation solution. Finally, the sensitivity of the EKF to three common image imperfections is investigated.
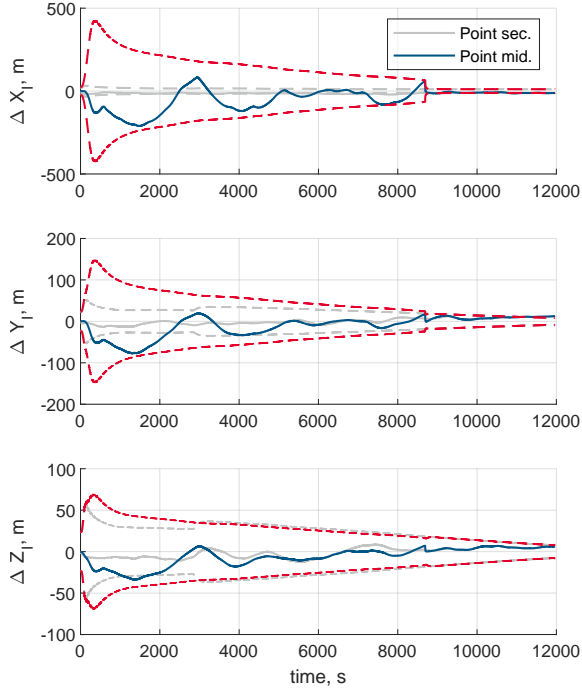
Fig. 10 *I*-frame position estimation errors, including error 3σ bounds. Pointing secondary compared to pointing at the midpoint.
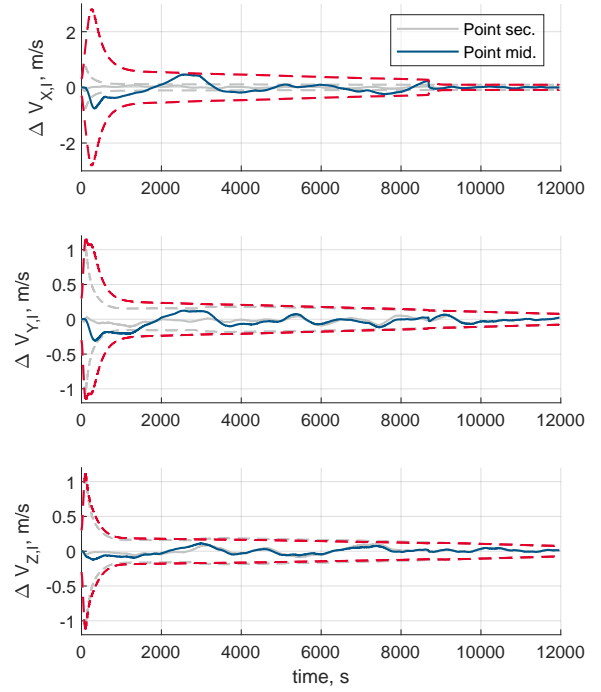
Fig. 11 *I*-frame velocity estimation errors, including error 3σ bounds. Pointing secondary compared to pointing at the midpoint.

Table 3 Navigation filter settings in the default configuration.

Setting	Value	Unit
Pointing strategy	Secondary	-
Approach trajectory	In-plane	-
Starting altitude	6770	m
Final altitude	300	m
Flight time	4	h
Accelerometer sample time	0.125	s
Camera & LRF sample time	5	s
σ_{acc}	2.8284×10^{-4}	m/s^2
$\sigma_{\text{acc,bias}}$	2.8284×10^{-5}	m/s^3
σ_{cam}	10	px
σ_{LRF}	15	m
Initial estimation error	0	-

A. Initial position sensitivity

The initial position can be chosen based on several factors: minimum fuel consumption, favorable lighting conditions, minimal overlap of the two asteroids in the image, to name a few. It could also be that the deployment of other spacecraft attached to the mothership have a higher priority and therefore a sub-optimal starting position is inevitable. Therefore, the sensitivity to the starting position is studied. A semi-sphere of 90 starting points is calculated, with the middle point located on the shell at the default starting position. The semi-sphere is positioned such that the Sun is usually behind the spacecraft, although the Sun phase angles can get very large for some starting positions. The other half of the sphere is
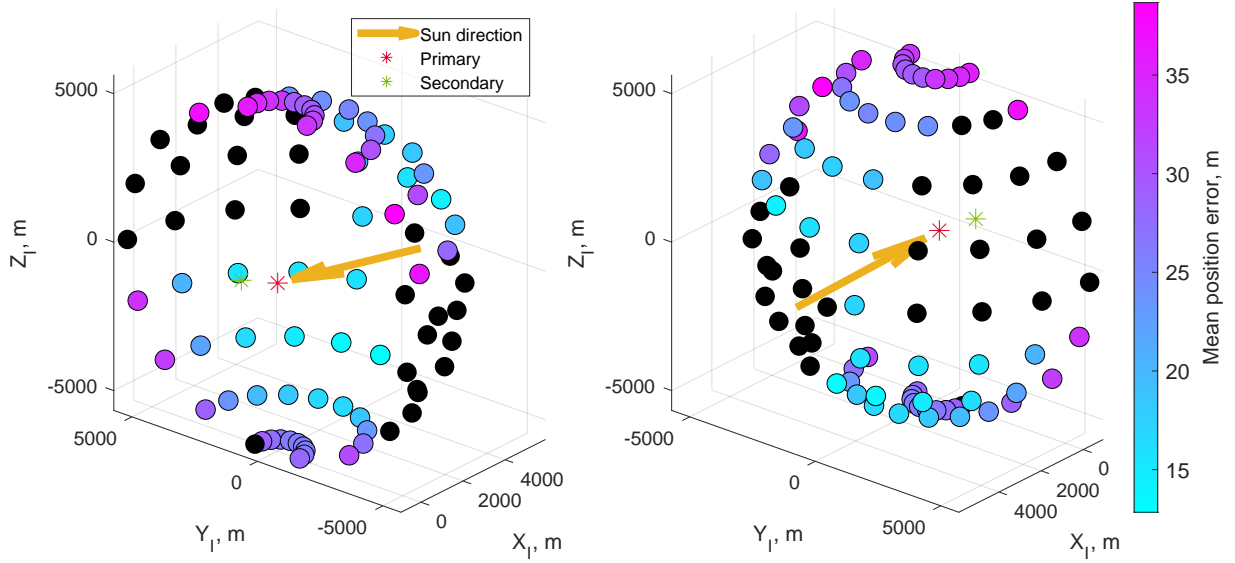
Fig. 12 Mean position error for different starting positions. Black dots indicate trajectories with final altitude above 600 m.

not considered because either the lighting conditions will be very challenging, or the spacecraft must fly around the primary asteroid to get to its target final position. The parameters as described in Table 3 are used. The metric used to summarize the performance of the EKF in a particular run is the mean position error. This error is calculated as follows:

$$\text{Mean position error} = \frac{\sum\limits_{i=1}^{n} \sqrt{\Delta_{x,i}^2 + \Delta_{y,i}^2 + \Delta_{z,i}^2}}{n} \tag{28}$$

where n is the total number of filter state samples in a run.

Figure 12 shows the results from two different viewing angles. The black dots indicate starting conditions that resulted in a trajectory that ended before an altitude of 600 m was reached. This is the result of the simulation being stopped by the image processing due to asteroids overlapping in the image, step 8 of Algorithm 1.

Several observations are made based on Fig. 12:

1) The black dots indicate that overlapping asteroids in the image are a major weakness of the current image processing implementation, limiting the scope of trajectories that can be flown.
2) Approaching the binary system out-of-plane, either from the top or the bottom, partially mitigates the previous shortcoming because the bodies will not overlap except for in the final moments of the high-altitude phase.
3) There is a relationship between the Sun phase angle and the mean position error.

The mismatch between the LRF measurement and the ellipsoid model, as well as the impact of irregular shapes and higher Sun phase angles on the center of figure estimation, have a major impact on the state estimation. To investigate which one of these is dominating the error behaviour observed in Fig. 12, the mean position error is shown against the mean Sun phase angle for the secondary asteroid, Fig. 13. The relationship between the independent variable x (mean Sun phase angle of the secondary) and the the dependent variable y (mean position error) is fit using linear regression. The assumed relationship is based on Eq. (9), because the image processing error is proportional to the Sun phase angle as well. The image processing error trickles down into the state estimation error, thus it is reasonable to expect the mean position error to follow a similar trend. The equation that is fit is:

$$y = \theta_0 + \theta_1 \arctan\left(\frac{8\pi R}{3\bar{r}} \sin^2\left(\frac{x}{2} \right) \right) \tag{29}$$

with $\bar{r}$ the mean altitude above the secondary asteroid, which is 3462 m for all runs that reach below 600 m of altitude. Linear regression yields $\theta_0 = 12.2$ and $\theta_1 = 273.0$. The adjusted R^2 is 0.829, indicating that the mean Sun phase angle of the secondary plays a major role in a run's mean position error.
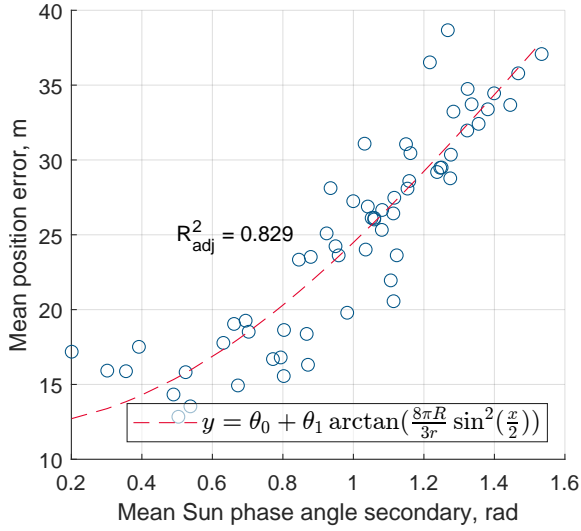
21

Fig. 13 Relationship between the mean Sun phase angle of the secondary asteroid and the mean position error for each colored starting point in Fig. 12.
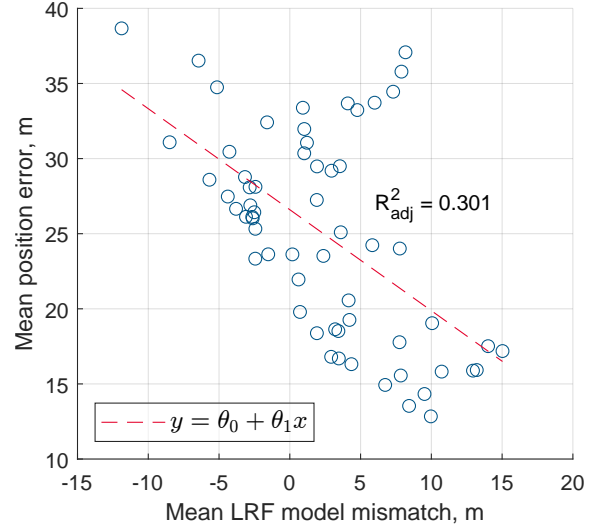

Fig. 14 Relationship between the mean LRF model mismatch and the mean position error for each colored starting point in Fig. 12.

Table 4 Summary of state estimation results for all colored starting points in Fig. 12. Worst value for each metric is highlighted for position, velocity, and accelerometer bias states.

	Position			Velocity			Acc. bias		
	X_I, m	Y_I, m	Z_I, m	X_I, m/s	Y_I, m/s	Z_I, m/s	X_B, m/s^2	Y_B, m/s^2	Z_B, m/s^2
Max RMS error	35.1	24.4	13.0	0.08	0.05	0.05	4.63×10^{-4}	4.04×10^{-4}	2.99×10^{-4}
Max RMS 3σ	28.9	26.8	25.5	0.21	0.20	0.19	1.655×10^{-3}	1.657×10^{-3}	1.436×10^{-3}
Max-max error	74.9	21.8	34.8	0.69	0.11	0.16	4.415×10^{-3}	3.795×10^{-3}	2.867×10^{-3}
Max final error	27.9	21.5	15.5	0.06	0.05	0.04	1.57×10^{-4}	1.38×10^{-4}	2.64×10^{-4}
Max final 3σ	11.3	9.8	8.5	0.09	0.08	0.08	4.78×10^{-4}	4.78×10^{-4}	5.20×10^{-4}

The same procedure is repeated for the LRF model mismatch. An attempt is made to describe the relationship as linear, resulting in an adjusted R^2 of 0.301. The data points and fitted line are shown in Fig. 14. The mean LRF model mismatch is 2.36 m, with a standard deviation of 8.28 m. The effect of the LRF model mismatch on the mean position error is not clear from this analysis, most likely because the image processing errors due to high Sun phase angles are dominating the error behavior. Note that only one ellipsoid model is tested with only one shape model in PANGU. For other (worse) shape models, the effect of the LRF model mismatch might be stronger.

Figures 15 and 16 show the position and velocity errors in the I-frame for all 61 runs that reach an altitude below 600 m. The run with the highest mean position error is highlighted. The centroid-based image processing struggles to estimate $\hat{p}_{\text{cof}}$ as the spacecraft moves closer to the asteroid. This is because the effect of the irregular shape and potentially high Sun phase angles is much more dominant at close range. Due to these two effects, the assumption that $\hat{p}_{\text{cof}}$ is a good approximation for p_{cof} no longer holds. The results of the starting position sensitivity analysis are summarized in Table 4.

B. Filter initialization error sensitivity

The EKF is initialized with a guess for the filter state. This guess is provided by the navigation system of the mothership, and is subject to additional uncertainty because the detachment of the spacecraft from the mothership is prone to errors and comes with uncertainties. The deployer ejection velocity can be adjusted up to a maximum value of 5 cm/s [36]. This does however not mean that the uncertainty is also 5 cm/s, because there are also uncertainties in the velocity of the mothership itself. In [37] the landing scenario for the Milani cubesat to land on Dimorphos is studied,
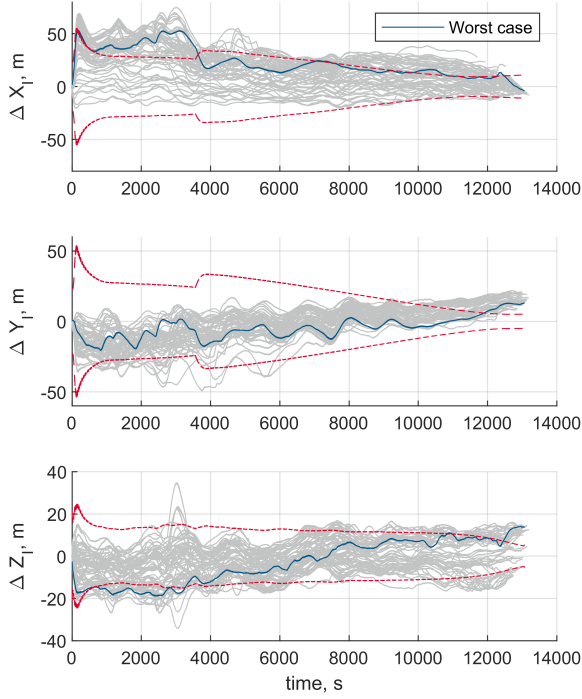
Fig. 15 *I*-frame position estimation errors for all colored starting points in Fig. 12. Error 3σ bounds are shown for the worst case.
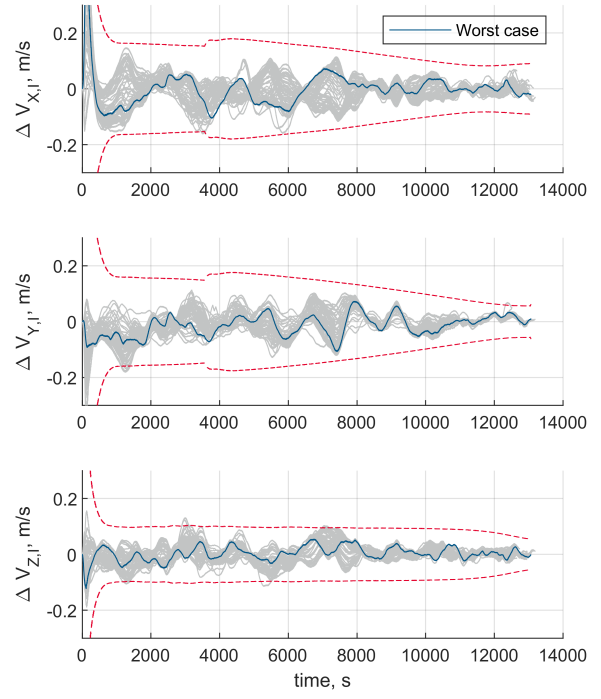
Fig. 16 *I*-frame velocity estimation errors for all colored starting points in Fig. 12. Error 3σ bounds are shown for the worst case.

and values of 13.3 m and 0.33 m/s (1σ) are used for the initial state uncertainty. In this work, very conservative values are used for the initial uncertainty, to push the EKF to its performance bounds in the reference landing scenario. The initial state error is calculated as follows:

$$x_0 = \begin{bmatrix} r^{IB}_{I,\text{true}} + \eta_{\text{pos}} \\ \dot{r}^{IB}_{I,\text{true}} + \eta_{\text{vel}} \\ b_{\text{acc},B,\text{true}} + \eta_{\text{acc.bias}} \end{bmatrix} \tag{30}$$

where η is a 3x1 vector whose components are randomly drawn from a normal distribution:

$$\eta_{\text{pos},x} \sim \mathcal{N}\left(0, \sigma^2_{\text{pos}}\right) \tag{31}$$

The following noise intensities are used: $\sigma_{\text{pos}} = 30$ m, $\sigma_{\text{vel}} = 5$ m/s, and $\sigma_{\text{acc.bias}} = 0.01$ m/s^2. These values are also used for the initialization of the P-matrix. In total 400 simulations are done with this random initialization, the results of which are shown in Figs. 17 and 18. The worst case that still converges is highlighted in the figures and is selected for further investigation. This specific run started with the 5th worst initialization error in terms of position, and the 6th worst accelerometer bias initialization. It thus represents a very extreme case within the dataset and the EKF has trouble converging for this extreme initialization error. By successfully converging in 390 of the 400 simulations with these very conservative initial uncertainties, the EKF proves to be robust to large uncertainties in the initial filter state. This is most likely due to the good initial observability with two asteroids in the camera frame on top of the LRF measurement.

C. Image imperfections sensitivity

The images that are rendered in PANGU have thus far not included any common imperfections. Imperfections such as radial distortion (Fig. 19a), an out-of-focus image (Fig. 19b), and salt & pepper noise (Fig. 19c) are investigated to evaluate the robustness of the EKF and image processing to these effects. Radial distortion is a common image imperfection associated with the lens of the camera, and Hendrycks (2019) mentions several other common image
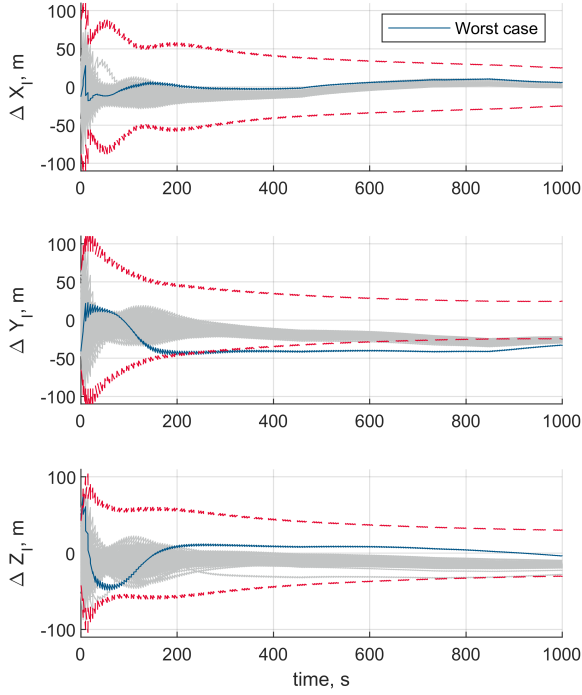
Fig. 17 *I*-frame position estimation errors for 400 random filter state initializations calculated with Eqs. (30) and (31). Error 3σ bounds are shown for the worst case.
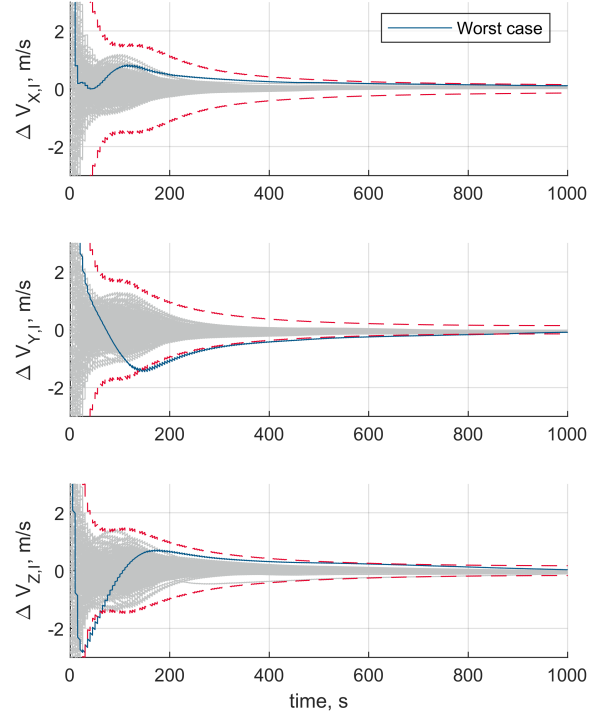

Fig. 18 *I*-frame velocity estimation errors for 400 random filter state initializations calculated with Eqs. (30) and (31). Error 3σ bounds are shown for the worst case.

imperfections [38]. Two overarching categories of imperfections found in [38] are identified and tested in this paper. These are noise imperfections (Gaussian noise, shot noise, impulse noise) and blur imperfections (defocus blur, frosted glass blur, motion blur, zoom blur). The image processing is expected to respond similarly to the imperfections within these two categories and therefore only one type of imperfection is tested from each category. Blur imperfections are simulated using a Gaussian blur filter, and noise imperfections are simulated using the salt & pepper noise filter. MATLAB functions from the Image Processing and Computer Vision toolbox∥ are used to implement the imperfections. The imperfections are applied to the image as soon as it is produced by PANGU, after which the image is sent to the image processing.

To create the radial distortion effect, PANGU's initialization function is changed. This results in the mapping of every undistorted point (i, j) to the observed distorted point (i', j') using Eqs. (32-34). The values for the coefficients K in Eq. (34) that are used are given in Table 5. The constants that are not mentioned are 0.

$$\begin{bmatrix} i' - i_0 \\ j' - j_0 \end{bmatrix} = C(R) \begin{bmatrix} i - i_0 \\ j - j_0 \end{bmatrix} \tag{32}$$

$$R = \sqrt{(i - i_0)^2 + (j - j_0)^2} \tag{33}$$

$$C(R) = 1 + K_0 + K_1 R + K_2 R^2 + K_3 R^3 + K_4 R^4 + \cdots \tag{34}$$

The values for the standard deviation of the smoothing kernel and the noise density are also given in Table 5. The standard deviation of the smoothing kernel determines the Gaussian function that is used to construct a convolution matrix that is applied to the original image [39]. The salt & pepper noise density determines the percentage of pixels that are affected by the noise. Each effect is studied separately, thus a total of 8 simulations are done. These are then

---

∥ https://de.mathworks.com/products/image.html, last accessed 2023/04/08

(a) Radial distortion, K_2 = 2e-06, K_4 = 2e-11.

(b) Gaussian blur, σ_{blur} = 3.

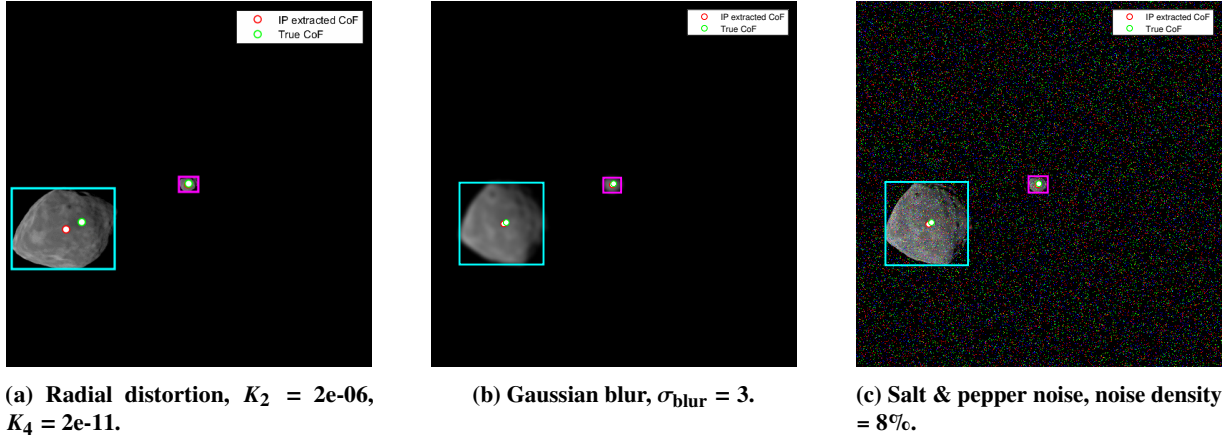**(c) Salt & pepper noise, noise density = 8%.**

Fig. 19 The three types of image imperfections that are studied

compared to a reference simulation without any imperfections. The simulation settings are as described in Table 3, with one change: the starting altitude is chosen to be 8589 m. The reason for this change is that the radial distortion can cause the primary asteroid to touch the border of the image at the start. This would mean that the centroid measurement from the primary asteroid is ignored in the EKF. With a more distant initial position, the primary is always completely visible in the image at the start. The effect of the radial distortion is most dominant at the edges of the image, and the effect on the secondary will be limited because it is in the center of the image. Therefore, changing the altitude to include measurements of the primary asteroid is important to analyse the effects of radial distortion. This effect is also observed in Fig. 19a, where for the primary the estimated center of figure is far off the true center of figure.

Table 5 Values used for the generation of image imperfections. Note that only one effect is applied at a time.

	Values			
Radial distortion coefficients (K_2, K_4)	(0,0)	(1e-6, 1e-11)	(2e-6, 2e-11)	-
Gaussian blur smoothing kernel σ	0	1	3	5
Salt & pepper noise density	0%	2%	5%	8%

For the reference settings described in Table 3, with a starting altitude of 8589 m, there is almost no impact on the EKF performance when the images are subject to Gaussian blur or salt & pepper noise. At all three intensity levels, the mean position error does not change more than 3% compared to the reference. This worst case number is observed for the Gaussian blur with a smoothing kernel σ of 5, resulting in a change of the mean position error from 18.54 m (without blur) to 19.10 m (with blur).

The impact of radial distortion on the state estimation is significant, as can be seen in Figs. 20 and 21. The position and velocity errors are shown for three different levels of distortion, level 0 up to level 2, corresponding to the values in Table 5. It is clear that larger distortion coefficients lead to an increase in the state estimation errors. The mean position error during the first 5000 seconds of the three simulations grows with each increase in radial distortion: from 21.66 m, to 41.28 m, to 59.37 m for the highest level.

Because the primary asteroid touches the border of the camera image earlier with a highly distorted image, the instantaneous reorientation to point at the secondary asteroid occurs at varying timesteps for all three levels of distortion. Once the primary asteroid is out of view, the estimation results are the same. This is reflected in the mean position error in the period after the first 5000 seconds: the mean position errors are then within 20 cm of each other for all three distortion levels. This is expected, because the effect of radial distortion is a function of the distance R from the center of the image, Eqs. (32-34). The distortion effect is therefore smaller in the center of the image, which is exactly where the secondary asteroid is located. On top of this, the asteroid is distorted equally in all directions away from the center of the image. The effect of the distortion on the center of figure estimation is not entirely symmetrical because of the irregular 3D shape model and non-zero Sun phase angle, but the mean position errors show that the state estimation errors due to the distortion effect are decreased significantly when only an asteroid in the center of the image is observed.
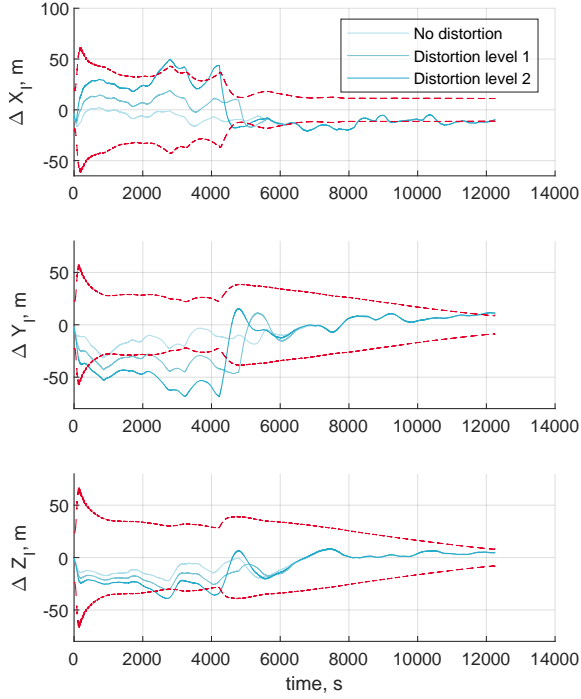
Fig. 20 *I*-frame position estimation errors for three levels of radial distortion given in Table 5. 3σ bounds shown for the highest level of radial distortion.
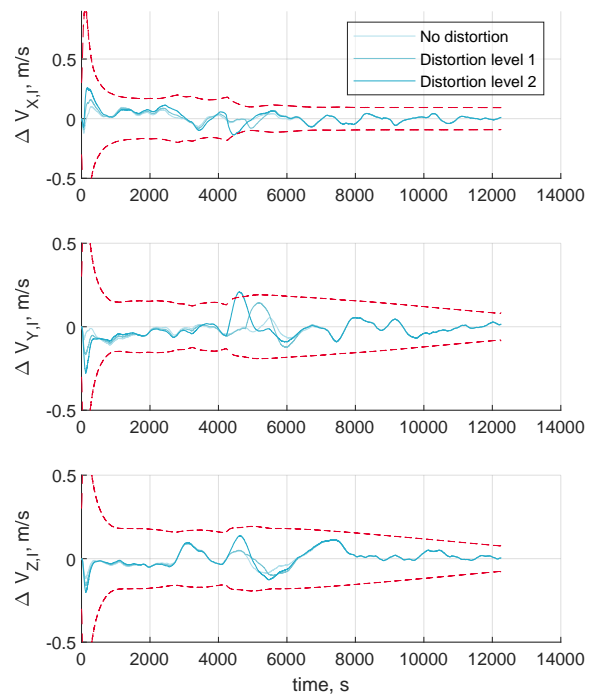

Fig. 21 *I*-frame velocity estimation errors for three levels of radial distortion given in Table 5. 3σ bounds shown for the highest level of radial distortion.

VI. Conclusions and recommendations

This work proposes an autonomous navigation solution for small spacecraft in a binary asteroid environment. It extends on previous work that investigated the effectiveness of laser range finders and cameras for navigation in (binary) asteroid environments. This section concludes the work done in this paper and gives a list of recommendations for future work.

A. Conclusions

An extended Kalman filter with nine parameters in the state vector is shown to successfully estimate the spacecraft state in an inertial reference frame. Prior knowledge of the asteroid ephemeris and ellipsoidal shape model is required to connect the relative measurements to the inertial frame. The image processing that extracts measurements from the camera images is identified as a pivotal component with a large influence on the performance of the filter. Its performance is impacted by high Sun phase angles and irregular asteroid shapes. It is shown that for an irregular asteroid shape and for high Sun phase angles, the quality of the measurements is still sufficient to perform the state estimation. Furthermore, the navigation solution is shown to be robust to large uncertainty in its initial state estimate. The navigation solution converges for 390 out of 400 simulation runs with conservative initialization errors. The filter state is also observable without the laser range finder, as long as there is good visibility of both asteroids. Finally, the navigation solution was tested with distorted and noisy camera images, to which the filter responded in a robust manner without any failure. The navigation solution developed in this work is therefore a robust option for medium to close range navigation in a binary asteroid environment.

B. Recommendations

This research leaves several important questions open that need to be answered in future work. Recommendations following the research presented in this paper are listed below.

Include attitude control and estimation: The pointing algorithm currently relies on the perfect knowledge of the state and asteroid ephemeris. This is an essential part to obtain the camera measurements that are inputs for the EKF.

In reality, this perfect knowledge is not available and therefore the spacecraft must determine and control its attitude. The desired pointing direction of the camera and LRF must be based on image data. Inclusion of such an image-based pointing algorithm leads to a more complete understanding of the capabilities of a spacecraft using this navigation system.

Improve the image processing: The issue of overlapping asteroids needs to be solved to increase the deployability of the navigation system. The current image processing requires permanent separation of the two asteroids in the frame. This limitation needs to be removed such that a wider range of approach trajectories can be flown.

Improve the center of figure detection: This will increase robustness to high Sun phase angles and to irregular asteroid shapes. Possible improvements are to exploit prior knowledge about the asteroid shape with a data-driven approach as proposed in [40], or by using AI-based image processing such as proposed in [41].

Test more image imperfections: This work includes Gaussian blur, radial distortion, and salt & pepper noise. Additional testing could for example include motion blur, over & under exposure, readout/reset smear, and color jitter.

Add more sensors: Adding more sensors potentially increases the robustness and performance of the filter. More LRF's, or a flash lidar could be added, as demonstrated in [5]. Adding a second camera allows the navigation system to obtain LOS measurements of both asteroids without being limited by the FOV of a single camera. These measurements can then be used with a triangulation technique, as presented in [13].

Validation: Testing the system in the real world is necessary to validate the results obtained in this paper. Pseudo-validation in the form of a comparison between the results in this paper and independently published work in literature is a valuable in-between step before real-world validation. A good candidate for real-world validation of the image processing is ESA's GNC Rendezvous, Approach and Landing Simulator (GRALS)**. Fly-bys with other bodies that are encountered on the way to the target asteroid can also be used to validate the navigation system.

Appendix A - Ellipsoid line intersection

The intersection of an ellipsoid and a line is used in $z = h(x, u)$ for the laser range finder measurement model. This appendix shows how this intersection is found. First, a line p is defined according to Eq. (35). This line will be in the direction of the z-axis of the B-frame, the boresight direction of the camera and also the direction of the LRF instrument.

$$p = v_0 + t v_1 \tag{35}$$

$$v_0 = (\chi_0, \gamma_0, \zeta_0)^T \tag{36}$$

$$v_1 = (\chi_1, \gamma_1, \zeta_1)^T \tag{37}$$

Here v_0 in Eq. (36) is the position of the spacecraft in the ellipsoid-fixed reference frame and v_1 in Eq. (37) is the direction that the LRF instrument is pointed in, which is the z-axis of the B-frame. Then, the ellipsoid is defined using Eq. (38). Here a, b, and c are the lengths of the semi-axes of the ellipsoid. For the asteroids, these are provided in [22].

$$\frac{x^2}{a^2} + \frac{y^2}{b^2} + \frac{z^2}{c^2} = 1 \tag{38}$$

Next, the line p is substituted into the ellipsoid equation:

$$\left(\frac{\chi_0 + t\chi_1}{a}\right)^2 + \left(\frac{\gamma_0 + t\gamma_1}{b}\right)^2 + \left(\frac{\zeta_0 + t\zeta_1}{c}\right)^2 = 1 \tag{39}$$

Expanding the terms in Eq. (39) and grouping the terms by their powers of t yields Eq. (40). Finding the solution for t is now only a matter of applying the quadratic formula.

**`https://www.esa.int/ESA_Multimedia/Images/2018/05/GRALS_Testbed`, last accessed 2023/03/21

$$\left(\frac{\chi_1^2}{a^2} + \frac{\gamma_1^2}{b^2} + \frac{\zeta_1^2}{c^2} \right) t^2 +$$

$$\left(\frac{2\chi_0\chi_1}{a^2} + \frac{2\gamma_0\gamma_1}{b^2} + \frac{2\zeta_0\zeta_1}{c^2} \right) t + \qquad (40)$$

$$\left(\frac{\chi_0^2}{a^2} + \frac{\gamma_0^2}{b^2} + \frac{\zeta_0^2}{c^2} - 1 \right) = 0$$

Finally, substituting the values found for t back into Eq. (35) yields the intersection points. The intersection point closest to ν_0 is used as the point of contact of the LRF.

Appendix B - Laser range finder verification

The LRF measurement model uses the ellipsoid-line intersection to calculate the expected LRF measurements. A test is set up in the simulator to check that the implementation is correct. For this test, the spacecraft is placed at a fixed distance of 500 m from the secondary asteroid center of mass. The spacecraft points at the center of mass of the secondary and the LRF measures the distance to the surface. The secondary then completes one full revolution around its center of mass. The experiment setup is visualized in Fig. 22. The LRF measurements are then compared with the expected measurements from the ellipsoid measurement model. By subtracting the LRF measurement from the altitude, the distance from the center of mass to the surface of the asteroid is obtained. With a full revolution of the asteroid, a slice of the asteroid 3D model is obtained. The same can be done for the ellipsoid model. Two tests are done, each test represents a different axis of rotation for the asteroid. The result of one of these tests is shown in the form of a polar plot in Fig. 23. The ellipsoid model captures the overall shape of the asteroid, and its orientation is also correct. This test verifies that the LRF measurement model is implemented correctly.
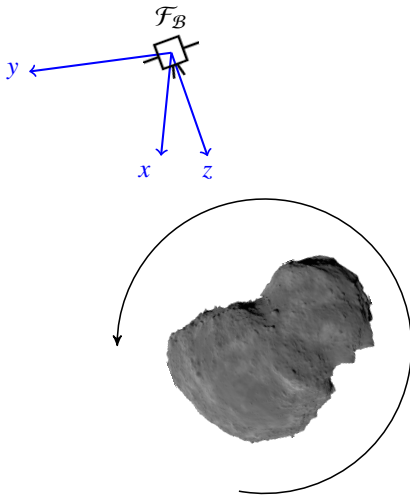

Fig. 22 Sketch of the LRF verification experiment. The secondary asteroid completes one full rotation around one axis.
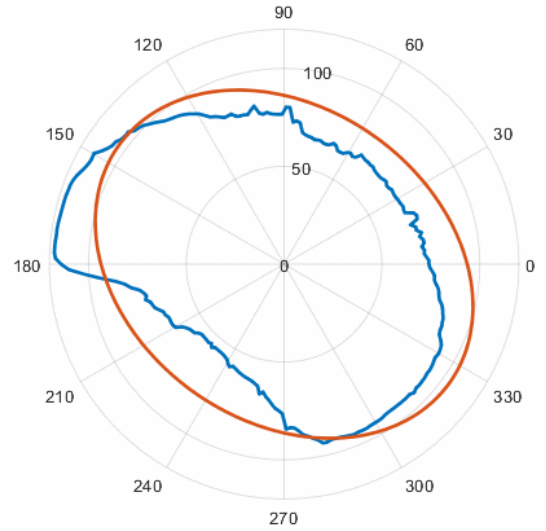

Fig. 23 Polar plot comparing the LRF measurement from PANGU (blue) and the ellipsoid measurements model (orange). Radial distance in m.

References

[1] Cheng, A. F. "Near Earth asteroid rendezvous: mission summary". In: *Asteroids III* 1 (2002), pp. 351–366.

[2] Kawaguchi, J., Fujiwara, A., and Uesugi, T. "Hayabusa—Its technology and science accomplishment summary and Hayabusa-2". In: *Acta Astronautica* 62.10 (2008), pp. 639–647. DOI: 10.1016/j.actaastro.2008.01.028.

[3] Ulamec, S. et al. "Rosetta Lander – Landing and operations on comet 67P/Churyumov–Gerasimenko". In: *Acta Astronautica* 125 (Aug. 2016), pp. 80–91. DOI: 10.1016/j.actaastro.2015.11.029.

[4] De Santayana, R. P. and Lauer, M. "Optical measurements for Rosetta navigation near the comet". In: *Proceedings of the 25th International Symposium on Space Flight Dynamics (ISSFD), Munich*. 2015.

[5] Dietrich, A. and McMahon, J. W. "Asteroid Proximity Navigation using Flash LIDAR". In: *AIAA/AAS Astrodynamics Specialist Conference*. American Institute of Aeronautics and Astronautics, Aug. 2014. DOI: 10.2514/6.2014-4355.

[6] Morley, T. and Budnik, F. "Rosetta Navigation for the Fly-by of Asteroid 2867 Šteins". In: *Proceedings 21st International Symposium on Space Flight Dynamics-21st ISSFD, Toulouse, France*. 2009.

[7] Synnott, S., Donegan, A., Riedel, J., and Stuve, J. "Interplanetary optical navigation-Voyager Uranus encounter". In: *Astrodynamics Conference*. American Institute of Aeronautics and Astronautics, Aug. 1986. DOI: 10.2514/6.1986-2113.

[8] Vetrisano, M. and Vasile, M. "Autonomous navigation of a spacecraft formation in the proximity of an asteroid". In: *Advances in Space Research* 57.8 (Apr. 2016), pp. 1783–1804. DOI: 10.1016/j.asr.2015.07.024.

[9] Christian, J. A. and Lightsey, E. G. "Onboard Image-Processing Algorithm for a Spacecraft Optical Navigation Sensor System". In: *Journal of Spacecraft and Rockets* 49.2 (2012), pp. 337–352. DOI: 10.2514/1.A32065.

[10] Christian, J. A. "Optical Navigation Using Planet's Centroid and Apparent Diameter in Image". In: *Journal of Guidance, Control, and Dynamics* 38.2 (Feb. 2015), pp. 192–204. DOI: 10.2514/1.g000872.

[11] Morita, H., Shirakawa, K., Kubota, T., Hashimoto, T., and Kawaguchi, J. "Hayabusa's Real-time Landmark Tracking Navigation for Descents and Touching-Downs". In: *AIAA/AAS Astrodynamics Specialist Conference and Exhibit*. American Institute of Aeronautics and Astronautics, June 2006. DOI: 10.2514/6.2006-6537.

[12] Adam, C. D. et al. "Transition from Centroid-Based to Landmark-Based Optical Navigation During OSIRIS-REx Navigation Campaign at Asteroid Bennu". In: *RPI Space Imaging Workshop*. 2019.

[13] Torre, F., Grey, S., and Vasile, M. "Angles-Only Navigation in the Proximity of a Binary Asteroid System". In: *Journal of Guidance, Control, and Dynamics* 44.1 (Jan. 2021), pp. 57–74. DOI: 10.2514/1.g004355.

[14] Stastny, N. B. and Geller, D. K. "Autonomous Optical Navigation at Jupiter: A Linear Covariance Analysis". In: *Journal of Spacecraft and Rockets* 45.2 (Mar. 2008), pp. 290–298. DOI: 10.2514/1.28451.

[15] Jia, H., Zhu, S., and Cui, P. "Observability-Based Navigation Using Optical and Radiometric Measurements for Asteroid Proximity". In: *IEEE Transactions on Aerospace and Electronic Systems* 56.4 (2020), pp. 2677–2688. DOI: 10.1109/TAES.2019.2953947.

[16] Huixin, Y., Xixiang, Y., and Weihua, Z. "State estimation of spacecraft formation near small asteroid". In: *Proceedings of 2014 IEEE Chinese Guidance, Navigation and Control Conference*. 2014, pp. 55–60. DOI: 10.1109/CGNCC.2014.7007219.

[17] Gil-Fernandez, J. and Ortega-Hernando, G. "Autonomous vision-based navigation for proximity operations around binary asteroids". In: *CEAS Space Journal* 10.2 (2018), pp. 287–294.

[18] Takahashi, S. and Scheeres, D. J. "Autonomous Exploration of a Small Near-Earth Asteroid". In: *Journal of Guidance, Control, and Dynamics* 44.4 (2021), pp. 701–718.

[19] Caroselli, E., Belien, F., Falke, A., Curti, F., and Förstner, R. "NEO-MAPP μLander GN&C for Safe Autonomous Landing on Small Solar System Bodies". In: *AAS GNC Conference*. Feb. 2022.

[20] Caroselli, E., Martin, M., Atkinson, K. R., Curti, F., and Förstner, R. "Autonomous lidar-free hazard detection and landing site selection for small bodies descent". In: *AAS GNC Conference*. Not yet published. Feb. 2023.

[21] Caroselli, E., Belien, F., Falke, A., and Curti, F. "Deep learning-based passive hazard detection for asteroid landing in unexplored environment". In: *AAS GNC Conference*. Feb. 2022.

[22] *"Hera Didymos reference model"*. ESA-TECSP-AD-017258. Revision 3. ESA. Feb. 2020.

[23] Kaula, W. *Theory of Satellite Geodesy: Applications of Satellites to Geodesy*. Blaisdell Publishing Company, 1966.

[24] Winkler, T., Kaplinger, B. D., and Wie, B. "Optical Navigation and Fuel-Efficient Orbit Control Around an Irregular-Shaped Asteroid". In: *AIAA Guidance, Navigation, and Control (GNC) Conference*. American Institute of Aeronautics and Astronautics, Aug. 2013. DOI: 10.2514/6.2013-5117.

[25] Werner, R. A. and Scheeres, D. J. "Exterior gravitation of a polyhedron derived and compared with harmonic and mascon gravitation representations of asteroid 4769 Castalia". In: *Celestial Mechanics and Dynamical Astronomy* 65.3 (1997). DOI: 10.1007/bf00053511.

[26] Nolan, M. C. et al. *Shape Model of Asteroid (101955) Bennu Bundle V1.1*. 2021. DOI: 10.26033/33BA-S419.

[27] Gaskell, R., Saito, J., Ishiguro, M., Kubota, T., Hashimoto, T., Hirata, N., Abe, S., Barnouin, O., and Scheeres, D. "Gaskell Itokawa Shape Model V1.0". In: *NASA Planetary Data System* (Sept. 2008).

[28] Simplicio, P. V. M. "Guidance and Control Elements for Improved Access to Space: from Planetary Landers to Reusable Launchers". English. PhD thesis. 2019. URL: https://research-information.bris.ac.uk/en/studentTheses/e2e36630-aa1f-4c9e-84a0-1fc290603520.

[29] Jean, I., Ng, A., and Misra, A. K. "Impact of solar radiation pressure modeling on orbital dynamics in the vicinity of binary asteroids". In: *Acta Astronautica* 165 (2019), pp. 167–183. ISSN: 0094-5765. DOI: https://doi.org/10.1016/j.actaastro.2019.09.003.

[30] Walter, U. *Astronautics*. en. 3rd ed. Cham, Switzerland: Springer International Publishing, Mar. 2019.

[31] Martin, I., Dunstan, M., and Sanchez Gestido, M. "Planetary Surface Image Generation for Testing Future Space Missions with PANGU". In: *2nd RPI Space Imaging Workshop*. United States: Sensing, Estimation, and Automation Laboratory, Oct. 2019.

[32] Oh, S.-M. and Johnson, E. "Relative Motion Estimation for Vision-Based Formation Flight Using Unscented Kalman Filter". In: *AIAA Guidance, Navigation and Control Conference and Exhibit*. American Institute of Aeronautics and Astronautics, June 2007. DOI: 10.2514/6.2007-6866.

[33] Otsu, N. "A Threshold Selection Method from Gray-Level Histograms". In: *IEEE Transactions on Systems, Man, and Cybernetics* 9.1 (1979), pp. 62–66. DOI: 10.1109/TSMC.1979.4310076.

[34] Montenbruck, O. and Gill, E. *Satellite Orbits*. Springer Berlin Heidelberg, 2000, p. 244. DOI: 10.1007/978-3-642-58351-3.

[35] Bar-Shalom, Y., Li, X.-R., and Kirubarajan, T. *Estimation with Applications to Tracking and Navigation*. John Wiley & Sons, Inc., 2001. DOI: 10.1002/0471221279.

[36] *"Hera proximity operations"*. ESA-TECSAG-TN-011315. Revision 1. ESA, 5, Feb. 2020.

[37] Fontcuberta, Í. "Landing a cubesat on an asteroid's moon". PhD thesis. Politecnico di Milano, 2021.

[38] Hendrycks, D. and Dietterich, T. *Benchmarking Neural Network Robustness to Common Corruptions and Perturbations*. 2019. arXiv: 1903.12261 [cs.LG].

[39] Stockman, G. and Shapiro, L. G. *Computer Vision*. en. Upper Saddle River, NJ: Pearson, Jan. 2001, pp. 137, 150.

[40] Pugliatti, M., Franzese, V., and Topputo, F. "Data-Driven Image Processing for Onboard Optical Navigation Around a Binary Asteroid". In: *Journal of Spacecraft and Rockets* 59.3 (May 2022), pp. 943–959.

[41] Kaluthantrige, A., Feng, J., Gil-Fernández, J., and Pellacani, A. "Centroiding technique using machine learning algorithm for space optical navigation". In: *3rd IAA Conference in Space Situational Awareness*. 2022, pp. 1–13.

Part II

Preliminary Analysis

*This part has been assessed for the course AE4020 Literature Study.

31

Literature Review

3.1. Preliminary work overview

This thesis is about autonomous navigation around asteroids. To understand why this topic is worth investigating, historical missions to asteroids are presented in Section 3.2. In Section 3.3 numerous recent studies on autonomous navigation around asteroids are presented. Section 3.4 presents the framework of the NEO-MAPP research study that this thesis is part of and the requirements that are set within the framework of this study. Preliminary technical work on the simulator is presented in Section 4.1, followed by conclusions of the preliminary work and a reflection on the answers to the research questions so far in Section 4.2.

3.2. Mission heritage

This chapter aims to partly answer RQ 1:

> **Research Question 1**
>
> What is the state of the art of navigation around asteroids?

Historical research and missions to asteroids brought forth a wealth of knowledge. Throughout time, missions got more advanced and so did the navigation technologies. Therefore, it is worthwhile to study the literature about asteroid missions and their flight-proven navigation methodologies. The research into asteroids was kicked off by the discovery of Ceres on January 1 1801 by Giuseppe Piazzi [34]. Ceres is a dwarf planet in the asteroid belt between the orbits of Mars and Jupiter. Since then, Earth-based observation technology has improved dramatically, leading to an increase in the number of asteroid discoveries. This is visualized in Fig. 3.1.

3.2.1. Earth-based Observations

Several asteroid properties can be determined from Earth-based operations, mainly relying on light-curves and radar measurements. These properties can include the body mass, shape, rotational period, spectrum and albedo [35, 36, 37]. There are also limitations to these Earth-based observations however. Some important limitations are:

- Only the Deep-Space Network (DSN) 70 meter antenna can provide data with a high enough signal-to-noise ratio to construct shape models. The applicability to close by asteroids is very limited however [36].

- The shape model constructed from the inversion of light-curves is very sensitive to the convexity of the target body. There is therefore a large uncertainty in the shape model.

- The asteroid mass can only be estimated if it is a multi-body asteroid orbiting a common center of mass.

To characterize the asteroid completely, the best solution is to fly there and take measurements from a spacecraft. The scientific research value, natural resource mining potential and planetary defence goals justify the money and time efforts made by space agencies to conduct such missions to asteroids. In this
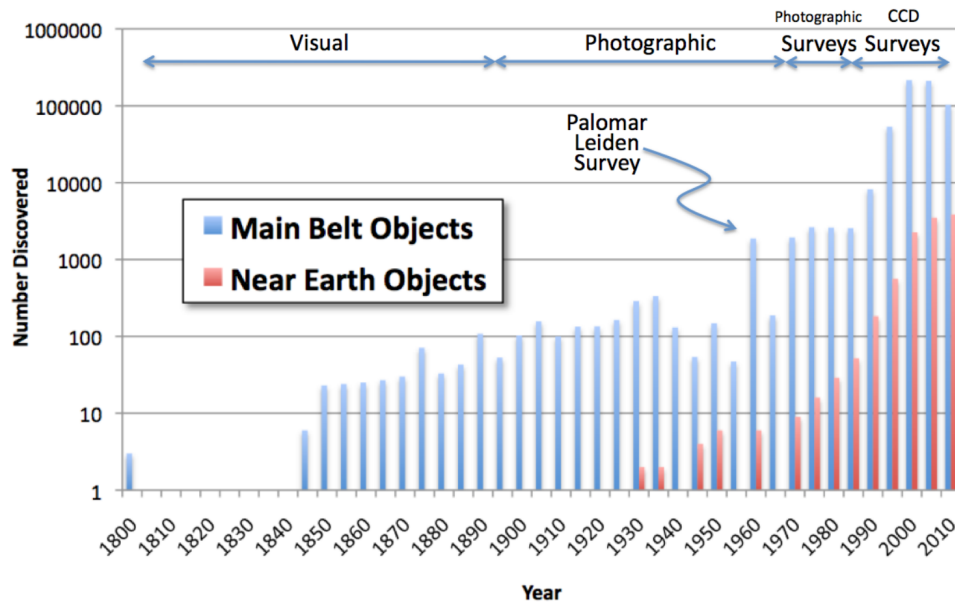
Figure 3.1: Main-belt and near-Earth discoveries [34].

chapter, several important past and present asteroid exploration missions will be presented. The focus will be on the navigation solutions and sensors used to achieve this.

3.2.2. Early Fly-bys

Before dedicated mission to asteroids were launched, several fly-bys of asteroids were conducted. The first one was the encounter of Galileo, a joint mission between ESA and NASA, with (951) Gaspra on October 29, 1991 [38]. Galileo was launched on October 18, 1989 to study Jupiter, its moons and the asteroids (951) Gaspra and (243) Ida. The second fly-by is especially interesting in the framework of this thesis because it was the first discovery of a binary asteroid.

A list of historical asteroid fly-bys and visits is given in Table 3.1.

Table 3.1: Historical asteroid missions overview [39].

Asteroid	Mission	Exporation Type	Year
(951) Gaspra	Galileo	Fly-by	1991
(243) Ida	Galileo	Fly-by	1993
(253) Mathilde	NEAR - Shoemaker	Fly-by	1997
(433) Eros	NEAR - Shoemaker	Orbiting/Landing	1998 - 2001
(9969) Braille	Deep Space 1	Fly-by	1999
(5535) Annefrank	Stardust	Fly-by	2002
(25143) Itokawa	Hayabusa	Hovering/Sampling	2005
(2867) Šteins	Rosetta	Fly-by	2008
(21) Lutetia	Rosetta	Fly-by	2010
(4) Vesta	Dawn	Orbiting	2011-2012
(4179) Toutatis	Chang'e 2	Fly-by	2012
67P/Churyumov-Gerasimenko [1]	Rosetta	Hovering/Landing	2014
(1) Ceres [2]	Dawn	Orbiting	2015-2018
(162173) Ryugu	Hayabusa2	Hovering/Sampling	2019
(101955) Bennu	OSIRIS-REx	Orbiting/Sampling	2018
(65803) Didymos	DART	High-Speed Impact	2021

3.2.3. NEAR - Shoemaker

NEAR (Near Earth Asteroid Randezvous) - Shoemaker is a NASA mission launched in February 1996. The goal of the mission was to increase the knowledge of asteroids in general by returning data to Earth. Near started orbiting its target asteroid (433) Eros in February 2000. An image of the asteroid is shown in Fig. 3.2. NASA's DSN (Deep Space Network) was used to perform radiometric tracking of the spacecraft to navigate it towards Eros [40]. Cameras were used to create a database of landmarks, after which these landmarks were tracked for navigation purposes, as well as rotational state estimation, shape, mass and gravity estimation. The landmark tracking and matching was done by hand by operators on Earth. A Laser Range Finder (LRF) was also used to get altitude measurements whenever the distance to the surface was in the hundreds of kilometers range. The LRF measurement was used in the orbit determination filter. The LRF was also used to solve for an accurate shape model, which was then used to obtain a-priori gravity estimates by assuming a constant density. The LRF was never used for real navigation purposes, but merely as a consistency check on the radiometric tracking and landmark-based navigation. By comparing the estimated gravity to the real gravity that the spacecraft experienced, it was concluded that the internal structure of the asteroid was mainly uniform. This constant density will also be assumed to create the gravity models in Subsection 4.1.3.

3.2.4. Hayabusa-1

Hayabusa-1 is a JAXA mission launched in May 2003. One of the primary goals of the mission was to return a sample of the surface of the target asteroid (25143) Itokawa back to Earth. A hybrid navigation solution was employed that combines optical navigation with radiometric tracking [11]. Images were processed on ground to calculate the direction vector from the spacecraft to the asteroid. A nonlinear least-squares estimator was used to obtain the spacecraft position and velocity in an intertial frame. In the final part of the descent, between 20 km and 3 km altitude, a more autonomous approach was envisioned. However, due to a hardware failure the crew decided to fly the spacecraft by hand. Still, the envisioned autonomous system is of interest for this thesis and is shown in Fig. 3.4. The intention was to use the

---

[1]67P/Churyumov-Gerasimenko is classified as a comet

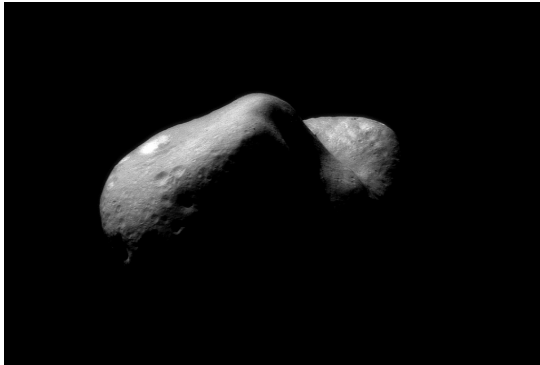[2]Ceres is classified as a dwarf planet since 2006

Figure 3.2: "Over Eros' horizon", taken on February 14, 2000 by NEAR. (Credits: NASA ,JPL, JHU-APL)
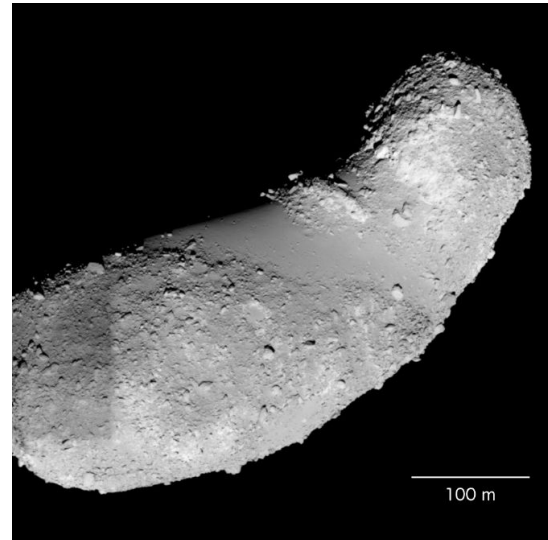

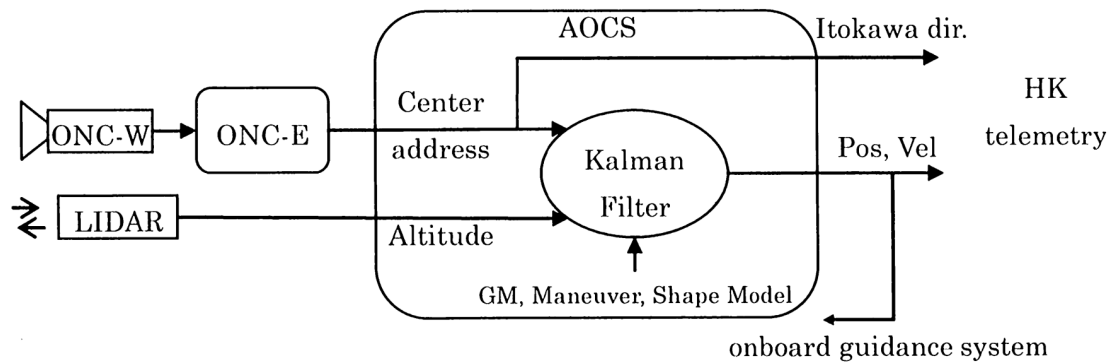**Figure 3.3:** "Itokawa", taken on 19 October 2005 by Hayabusa-1. (Credits: JAXA)

Figure 3.4: Onboard navigation system of Hayabusa-1 [11].

altitude measurement from the Lidar together with the 'center address' which is calculated from images of the onboard navigation camera's. This center address is found by extracting groups of adjoining pixels whose brightness is beyond a specified threshold. The group that has the highest number of pixels is assumed to be the one representing the asteroid, after which the centre of this group in the frame (pixel coordinates) is used in a Kalman filter to estimate three-dimensional relative position and velocity [41].

Noteworthy is the target marker approach that was used for the final descent. A bright object was released from the spacecraft and fell onto the surface of the asteroid. This target marker was then used by the navigation system as a point of reference in the frame.

3.2.5. Rosetta

Rosetta is an ESA mission launched in March 2004 to comet 67P/Churyumov–Gerasimenko, shown in Fig. 3.5. The spacecraft performed fly-bys of asteroids (2867) Šteins and (21) Lutetia on its way to the comet [10]. During the approach, from circa 44000 km to 122 km, radiometrics and optical information were used as primary measurements for the navigation. Single image frames contain both the asteroid and the star field behind it, giving valuable information for the state estimation. After 3500 km, the star field was no longer useful because the centroiding errors were so large that they were more significant than any pointing error that could be deduced from the measurements.

Upon arrival, an early characterisation phase was carried out, during which the rotational state, shape, landmarks identification and a first estimate of the gravity field were determined [19]. Since then, and

Figure 3.5: "67P/Churyumov–Gerasimenko", taken on March 11, 2015 by Rosetta's narrow angle camera 'Osiris'. (Credits: ESA/Rosetta/MPS for OSIRIS Team MPS/UPD/LAM/IAA/SSO/INTA/UPM/DASP/IDA – CC BY-SA 4.0)
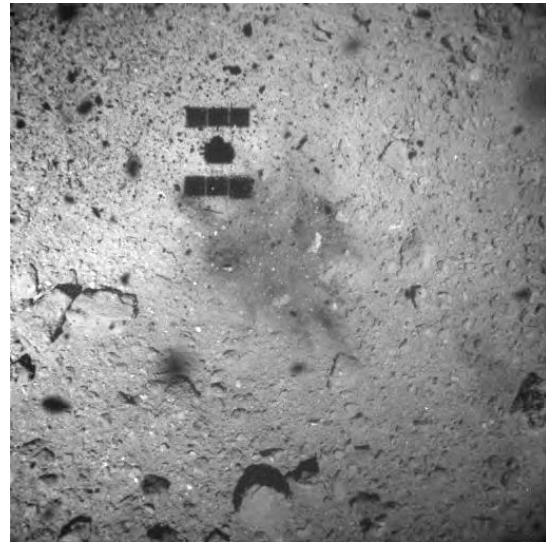

Figure 3.6: "Ryugu, image captured near the touchdown site immediately after touchdown.", taken on 22 February 2019 by Hayabusa-2's wide angle optical navigation camera 'ONC-W1'. (Credits: JAXA, University of Tokyo, Kochi University, Rikkyo University, Nagoya University, Chiba Institute of Technology, Meiji University, University of Aizu, AIST.

throughout the rest of the mission phases, Rosetta navigated using landmark observations which were obtained on-ground by processing NAVCAM images. As the mission progressed, automatic feature detection methods were phased in to track the landmarks.

3D high-resolution maps (maplets) of landmarks are created from these observations. Combined with an albedo map and photometric model, the visual appearance of the landmark can be predicted for every observation condition. Matching the landmarks to a library of known landmarks gives a measurement for the navigation filter.

3.2.6. Hayabusa-2

Hayabusa-2 is a JAXA mission launched in December 2014 to target asteroid (162173) Ryugu. Hayabusa-2's purpose is to characterize a C-type asteroid and study its subsurface properties. Besides this, an artificial crater generation technology is demonstrated, with the goal of having increased robustness in the sample-return missions. This artificial crater is created by launching a mass at high speed into the surface, leaving a 2-m-class crater [42]. Besides this, two rovers, MASCOT and MINERVA-II were successfully released on the surface of the asteroid. A stunning image of the spacecraft's shadow cast onto the asteroid is shown in Fig. 3.6.

For the navigation, an extensive characterisation phase is carried out. In this phase, the axis of rotation, period, shape model, and gravity field are determined. The characterisation phase uses a home position at 20 km altitude and various descents to around 1 km were carried out. During these descents, Lidar was used to estimate the vertical velocity [43]. Radiometric tracking once again plays a vital role in the navigation of the spacecraft, allowing the precise determination of the orbit.

During the final descent, a target marker is once again deployed, just as with Hayabusa-1. It is released at 100 m, and then from 30 m the spacecraft is fully autonomous in its descent.

3.2.7. OSIRIS-REx

OSIRIS-REx stands for Origins Spectral Interpretation Resource Identification Security Regolith Explorer. It is a NASA mission to asteroid (101955) Bennu, launched in September 2016. Its main purpose was to

characterise the geochemistry of the asteroid by bringing back samples to Earth.

For its navigation, OSIRIS-REx uses a combination of radiometric tracking and optical navigation. The uncertainties in Bennu's ephemeris, size, shape, spin-state and composition were too large to rely on radiometric tracking alone, creating a need for optical navigation [44]. To solve for the camera pointing error, separate images at different exposure times were taken to image both the star field as well as the asteroid from the same position. A centroiding algorithm is used to determine the inertial attitude of the camera at the image epoch. Once the center of the asteroid is found in the frame, the CoM location is determined using an appropriate algorithm. The camera attitude and the residual between the predicted and observed target centroid are then used to estimate a solution for the body-relative spacecraft state [45].

For close operations and for navigation to the touch-and-go zone, landmark tracking is used. A transition period from centroid-based navigation to landmark-based navigation occurred once the digital terrain maps of the surface had been generated. Besides the terrain map, albedo maps and photometric curves were available for these landmarks, making it possible to render the landmark image and compare it to the real camera image. Images of a collection of landmarks are rendered simultaneously onboard and then matched to the visual information, yielding position and attitude information. Besides these measurements, 4 Lidar sensors were also used to provide additional measurements to the navigation system.

3.2.8. DART

DART (Double Asteroid Redirection Test) is NASA's contribution to the AIDA (Asteroid Impact and Deflection Assessment) mission. This is a joint mission between ESA and NASA. DART has already been launched in November 2021 and is currently on its way to the binary asteroid (65803) Didymos, the same asteroid system that is studied in this thesis. DART will impact with the moon of the binary asteroid, Dimorphos. ESA's contribution is then to send a spacecraft to investigate the aftermath of the impact.

The majority of the flight will be navigated using radiometric tracking provided by the DSN [46]. However, the asteroid encounter cannot rely on radiometrics. The impact speed will be around 6.6 km/s. With the 70 seconds round-trip-time, this means that it is impossible to use ground-in-the-loop GNC techniques. Therefore, an autonomous navigation solution is used. The optical navigation relies on a centroiding algorithm that functions in three steps. First, all pixels in the image that are above a certain brightness threshold are selected. Then, groups of pixels that satisfy this threshold requirement are grouped together. Then the final step calculates a set of statistics associated with each group, such as the size of the group, average brightness and centroid location. This list of statistics for each group is then used to determine which one of the groups is the asteroid. The largest/brightest group is the default setting. The result of this calculation is the line of sight measurement. Combined with accurate attitude information, the line of sight measurement is transformed into inertial coordinates. Proportional navigation principles are then used in an extended Kalman filter to predict the miss distance at closest approach [7].

3.2.9. Conclusion Past Missions

The goal of this chapter is to partially answer RQ 1:

> **Research Question 1**
>
> What is the state of the art of navigation around asteroids?

Historical missions are a good indicator for the state of the art, as these are flight-proven technologies that have had various successes during real missinos. While not every single historical asteroid mission has been covered, it is clear that there is a certain common approach that is used in one way or the other in all of them. To underline this, Table 3.2 shows an overview of the navigation techniques used in historical asteroid missions.

Radiometric tracking using the Deep Space Network is the backbone of almost all of the navigation strategies. This technique provides a precise estimate of the position of the spacecraft with respect to Earth. Vision-based navigation techniques are then used at later stages in the mission to provide information about the relative position and velocity of the spacecraft with respect to the asteroid. An early characterisation phase during which a shape model and landmark library is created is very common. By using laser range

Table 3.2: Overview of navigation techniques used in historical missions to asteroids.

Mission name	Year	Altitude phase	Sensors used	Type of filter	Comments
NEAR Shoemaker	2000	350-35 [km]	Radiometrics, camera, LRF	Batch estimation, square root information filter	Camera not used for primary navigation, rather for mapping
Hayabusa-1	2003	4000 - 20 [km]	Radiometrics, cameras	Nonlinear least-squares estimation	Images processed on ground to calculate vector measurements (line of sight), target marker used for descent/landing
		20 - 3 [km]	Camera, Lidar	Kalman filter	Not used due to hardware failure, backup human-in-the-loop method used
Rosetta	2004	44000 - 122 [km]	Radiometrics, cameras		Stars used to solve camera pointing errors at >3500 [km]
		122 - 0 [km]	Radiometrics, camera		Landmark tracking, processing on Earth. First manual process, later automatic
Hayabusa-2	2014	20 - 0 [km]	Radiometrics, cameras, Lidar		Lidar used for vertical speed estimation. Target marker tracking below 100 [m]
Osiris-REX	2016	-	Radiometrics, cameras, Lidar		Centroid-based optical navigation for far away operations, stars used to solve camera pointing error
		-	Radiometrics, cameras, Lidar		Onboard image rendering using model, matched to observations
Dart	2021	>35000 [km]	Radiometrics, cameras	Extended Kalman filter	
		35000 - 0 [km]	Cameras		Centroid-based navigation, proportional navigation

finders and Lidar, the distance to the asteroid is measured, allowing the gravity field to be estimated. Radiometric tracking is still used to solve for the orbit, making it an essential component of the navigation strategy.

A major drawback to relying so heavily on radiometric tracking for navigation purposes is that the spacecraft must always be equipped with the hardware to support this, preferably a steerable High-Gain antenna. The use of the Deep Space Network is also expensive, and due to long round-trip-times not well suited for close proximity operations when used just on its own. The fact that the orbit determination is generally done in batches, meaning that an orbit arc of a certain duration is required, makes it unsuitable for close proximity operations. The vision-based components are added to the navigation system to escape the limitations of Earth-in-the-loop state estimation techniques that use radiometric tracking. Once Earth is out of the loop, the state estimation can be performed much faster, after which onboard autonomous guidance decides the next maneuver of the spacecraft.

The early characterisation phase is therefore a costly and long process that is absolutely necessary to facilitate the safe operation of the spacecraft close to the proximity of the asteroid. The early characterisation phase is used to gather knowledge about the body which is used in part for the autonomous navigation for close proximity operations.

3.3. Current status of asteroid navigation research

While the previously flown asteroid missions have proven that certain navigation methods provide satisfactory performance for that mission, new navigation methods can still improve on these existing solutions. The push towards a higher level of autonomy, the use of low-cost hardware, and less dependence on the Deep Space Network for radiometric tracking, brings new challenges for the development of the navigation system. This chapter again deals with RQ 1, but now by looking at recent research instead of past missions.

> **Research Question 1**
>
> What is the state of the art of navigation around asteroids?

First in Subsection 3.3.1 an introduction on autonomy in general and the definitions used in this research work is given. Then in Subsection 3.3.2 a selection of research work that builds upon the past asteroid missions is presented with a focus on autonomous navigation. In Subsection 3.3.3 a few research works on image processing of asteroid navigation camera images are presented.

3.3.1. Autonomy

Autonomy and autonomous navigation are two keywords in this thesis that deserve some attention on their own such that it is clear what is meant by these words. NASA defines autonomy as follows:

> **"Autonomy is the ability of a system to achieve goals while operating independently of external control."**
>
> *- 2015 NASA Technology Roadmaps*

The definition of a system by NASA is as follows:

> **"A system is the combination of elements that function together to produce the capability required to meet a need. The elements include all hardware, software, equipment, facilities, personnel, processes, and procedures needed for this purpose."**
>
> *– 2016 NASA Sys. Eng. Handbook*

Autonomy is not necessarily linked to artificial intelligence or automation, but they are often used as means to make a system autonomous. The goal of autonomy is to have a system that is self-directed and self-sufficient. This does not exclude human intervention, as long as it is included in the definition of the system that is autonomous. Autonomy is needed in time-critical decision making, especially when communications constraints are large such as in the deep space environment. Autonomous systems can

use the on-board data instead of just a limited set of downlinked data. This leads to a possible improvement of the robustness of the system and a reduced complexity. Reduced complexity again leads to a reduce in cost.

NASA defines four major branches of autonomy. These are:

1. Situation and Self Awareness
2. Reasoning and Acting
3. Collaboration and Interaction
4. Engineering and Integrity

The work in this research focuses on the first branch, situation and self awareness. Especially the sub-branches "sensing and perception" and "state estimation and monitoring".

3.3.2. Recent Navigation Methods Research

The past asteroid missions have been autonomous up to varying degrees. Once the early characterisation phase is completed and a great deal of knowledge about the asteroid is gathered and processed, either onboard or on Earth, the spacecraft is ready to perform some tasks autonomously. This is especially relevant for close proximity operations, where the round-trip delay is so large that remote controlling from ground is impossible. The research works that are highlighted in this literature review are selected based on the sensor set and assumed prior knowledge. Preference goes to research that uses a simple sensor set such as camera's, accelerometers, star trackers and laser range finders. Radiometric tracking is not an option because Earth must be kept out of the loop. Furthermore, some research work on image processing is included in the next section.

Autonomous vision based navigation for proximity operations around binary asteroids
By Jesus Gil-Fernandez and Guillermo Ortega-Hernando, 2018
The objective of this autonomous system is to improve the on-board knowledge of the state compared to the ground prediction. This is of great importance because the ground-based prediction error at some stages in the mission under consideration is comparable to the camera field of view. This paper describes a method to estimate the state vector given by Eq. (3.1). The target asteroid used is the binary asteroid Didymos is used [32]. ϵ_{cob} relates changing illumination conditions to a mismatch between the center of mass (CoM) and center of brightness (CoB). Through image processing the CoB can be observed, but the CoM is what is known from the ephemeris data. Therefore, a link between the CoB and CoM must be made, and this ϵ_{cob} parameter aims to make this link more accurate. The equation used is valid for quasi-spherical bodies.

The estimation of the CoM of an asteroid is in reality a very elaborate and complex procedure. A simple relationship between Sun phase angle and CoB on a sensor from multiple kilometers away is therefore a very rough approximation of the location of the CoM. It will still be called the CoM because this is in the end what is approximated to make the link with ephemeris data. However, it is important to remember the origin of this measurement and the large uncertainties at play.

$$\hat{X} = [r, \dot{r}, \mu, \epsilon_{cob}]^T \tag{3.1}$$

Only the primary is observed using a single camera. The state is determined relative to the asteroid body. Combined with knowledge of the ephemeris of the binary asteroid system and the attitude of the spacecraft, the state is therefore also determined in inertial space. The image processing consists of several steps, such as windowing to remove the secondary asteroid from the calculations, thresholding, binarization and the computation of the CoB. An unscented Kalman filter (UKF) is used for the state estimation. The goal of this navigation system was to keep the camera pointed at the asteroid during a close proximity maneuver, and the performance in this regard was satisfactory according to the authors. Some metrics on the performance of the filter are shown in Figs. 3.7 and 3.8.

Autonomous Exploration of a Small Near-Earth Asteroid
By Shota Takahashi and Daniel J. Scheeres, 2021
This paper presents an end-to-end autonomous exploration scheme with onboard navigation [33]. A
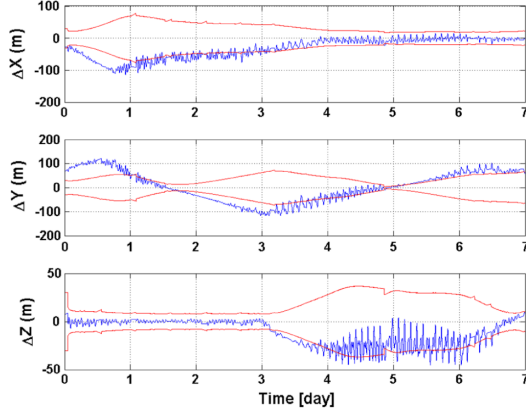
Figure 3.7: "Position estimation error and estimated ± 1-sigma (Monte Carlo worst case scenario with high-fidelity image generation and IP in the loop)" [32]
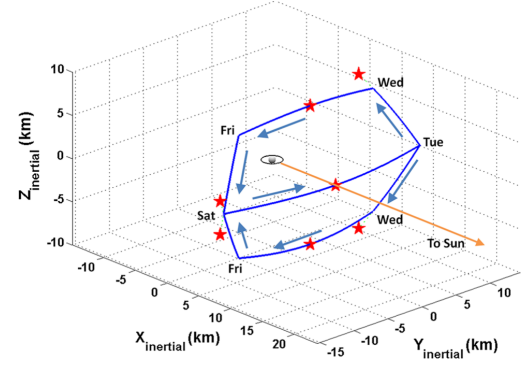

Figure 3.8: "Trajectories for the detailed characterization phase (arrows indicate flying direction)" [32]

Figure 3.9: Two types of information that can be extracted from camera images: the angular direction and angular size of the asteroid object. Both suffer from scale invariance. [33]

technique called ΔV ranging is used in the navigation. In practice, this means that once a certain distance or predefined event surface is crossed by the spacecraft, an impulsive maneuver is performed. This maneuver relocates the spacecraft back away from the asteroid. A series of such maneuvers allows the spacecraft to complete the characterization of the asteroid.

The sensors used are only a camera and an accelerometer. Because camera measurements suffer from scale invariance, meaning that there is no information about the scale of the object in the frame when only images are used. The scale of the object must be determined in another way. Once this scale is known, the size of the object in the frame can be used to estimate the distance to the object. The method to perform this estimation relies on ΔV ranging.

The states estimated by the filters in this paper are as described in Eq. (3.2).

$$\hat{X} = [r, \dot{r}, \rho_{srp}, \mu, \Delta V_i, \tau_i]^T \qquad (3.2)$$

Here ρ_{srp} is the reflectivity coefficient used in the solar radiation pressure calculation. ΔV_i is the ΔV of maneuver i and tau_i is the time of the ith maneuver. Two different filters are used. An extended Kalman filter (EKF) is used to detect when the next maneuver should happen, for instance when the position crosses a certain event surface. Then a different filter that the authors call the iterative Kalman filter (IKF) is switched on to design the ΔV maneuver. The authors state that if state errors are small, the EKF-only approach is also sufficient, and that the IKF adds robustness to the navigation process in this case.

In this research work, there is a strong coupling between navigation and guidance. The maneuvers are essential to the navigation, otherwise the scale invariance cannot be broken and state estimation is impossible. The use of the angular size of the asteroid, depicted in Fig. 3.9 is especially interesting because not many research works extract this measurement out of the image frames. The authors write that "For the hovering trajectory, the numerical analysis shows that the angular size information helps determine the relative range, assuming that the asteroid's size is known accurately". As a reference asteroid, the authors use (101955) Bennu with a mean radius of 246 m. The performance of the method for the trajectory shown in Fig. 3.11 is shown in Fig. 3.10.
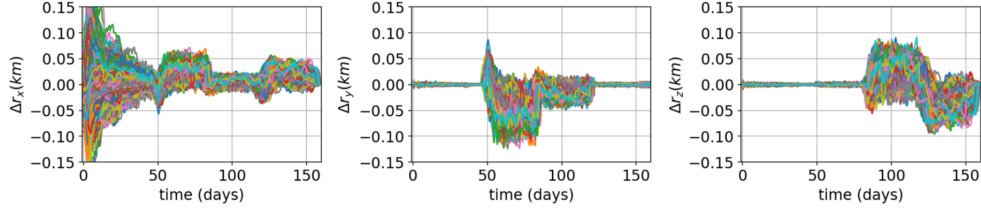
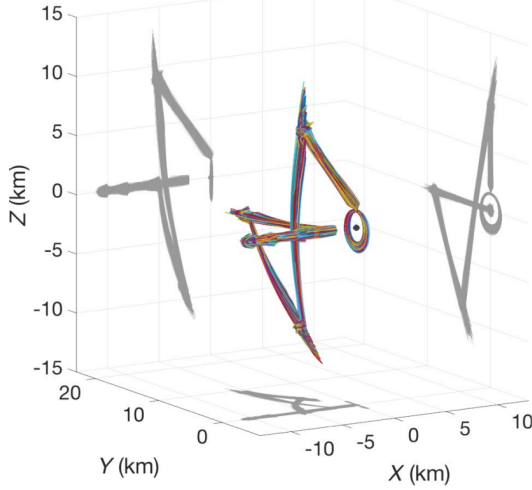**Figure 3.10:** "Position and parameter errors for the 1000 Monte Carlo runs (close-hovering phase)" [33]

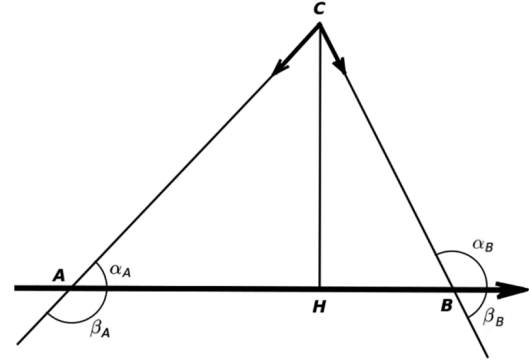**Figure 3.11:** "Trajectories from 1000 Monte Carlo runs (close-hovering phase)" [33]

Figure 3.12: "Basic triangulation scheme" [28]

Angles-Only Navigation in the Proximity of a Binary Asteroid System
By Francesco Torre, Stuart Grey, and Massimiliano Vasile, 2021

This paper investigates the possibilities of performing an angles-only navigation strategy at the binary asteroid systems 65803 Didymos [28]. The fundamental principle of angles-only navigation is triangulation, shown in Fig. 3.12. The pointing vectors of the camera to the primary and secondary asteroid are used in combination with knowledge of their respective motion. Interesting about this method is that the binary nature of the target asteroid is used to perform the state estimation with very minimal hardware.

Two core sensitivities of this method are the dependence on separation of the two objects to perform the triangulation accurately, and the knowledge of the position of the two bodies. The authors choose to fly at the Lagrange point L4 to test the algorithm, which guarantees excellent separation of the two bodies. Furthermore, it is assumed that individual measurements can be taken of both primary and secondary asteroid.

The states estimated are the position and velocity, given in Eq. (3.3).

$$\hat{X} = [r, \dot{r}]^T \tag{3.3}$$

Because in reality the binary asteroid system rotates and undergoes a wide range of lighting conditions, the authors implemented a limb fitting algorithm to find the CoM of the object in the frame. This method predicts the CoM location in the camera detector frame based on fitting an ellipse to the detected edges in the frame. The estimate for the CoM is then the center of the fitted ellipse, as seen in Fig. 3.13. The authors state that this method works well for spherical objects, but for ellipsoids the performance deteriorates. This nagative effect is strongest when the body is partially lit.

For the state estimation, an unscented H^∞ filter (UHF) is used. The authors motivate this choice by the expectation that the dynamics of the spacecraft are significantly nonlinear and the significant uncertainty in
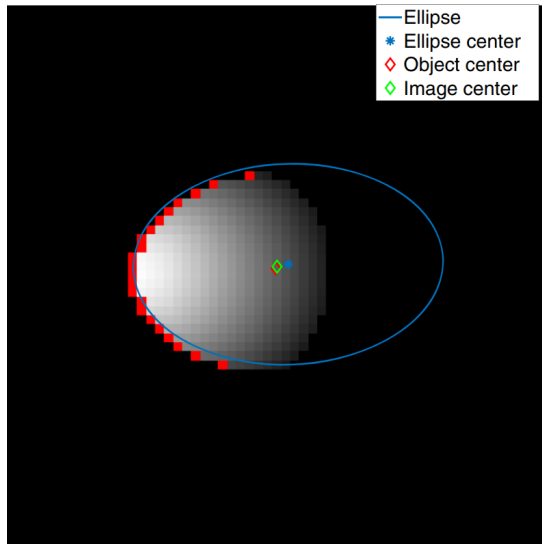
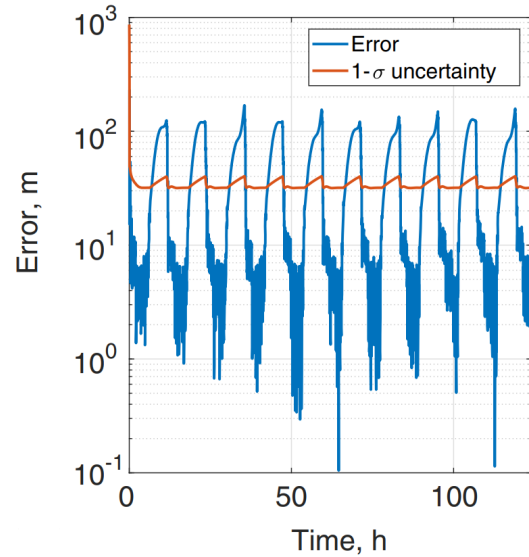**Figure 3.13:** Ellipse limb fitting algorithm applied to a half lit asteroid [28]

Figure 3.14: "Position estimation error" [28]

the measurements. The H^∞ filter is deemed a good compromise between robustness and computational complexity for this type of problem [23], and the choice in this particular case is motivated by this previous analysis.

The results at L4 with the exact knowledge of the distance between primary and secondary are shown in Fig. 3.14. The periodic behaviour in the errors is caused by the eclipses. If there is a slight difference in the distance between primary and secondary that is used in the simulation and in the filter, the state estimation deteriorates significantly as can be seen in Fig. 3.15. The change in semimajor axis of the orbit of the secondary gives it a different period, causing high-amplitude periodic differences between the real position of the secondary and the belief that the spacecraft has of this position. This amplitude can be as big as twice the semimajor axis of the orbit. As a solution, the authors propose an augmented state vector in which the semimajor axis is also estimated. They show that this does allow the spacecraft to safely navigate in the precence of uncertainties in the semimajor axis.

Variations in the eccentricity and inclination of the orbit of the secondary also increased the state estimation error by as much as an order of magnitude for variations of 0.030 and 25 degrees in the eccentricity and inclination respectively. Because these changes do not alter the orbital period, the result is less catastrophic than a varying semimajor axis.

Autonomous Optical Navigation at Jupiter: A Linear Covariance Analysis
By Nathan B. Stastny and David K. Geller, 2008

This paper takes the concept of angles-only navigation a step further than [28] by applying a similar navigation solution to the problem of navigating around Jupiter by taking angle measurements from the moons of Jupiter [29]. Where in a binary system at most two angular measurements are available, in the environment with many moons this number can be greatly increased. Even after a selection procedure based on the visual magnitude of the moon as detected by the navigation camera, the Sun cone angle and whether the moon is obscured by Jupiter, still 8 or more moons are visible most of the time.

An extended Kalman filter (EKF) is used with a state vector given by Eq. (3.4). ϵ are the sensor misalignments and $\delta\theta$ the attitude knowledge error.

$$\hat{X} = [r, \dot{r}, \epsilon, \delta\theta]^T \tag{3.4}$$

The authors conclude that the greatest sensitivity of the system lies in the number of moons that are imaged. The next greatest sensitivity is the line-of-sight pointing error resulting from attitude knowledge
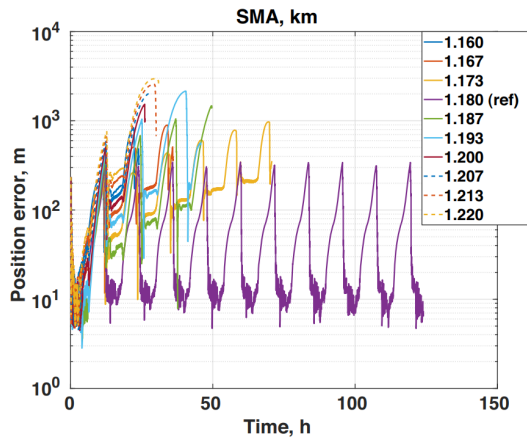
Figure 3.15: Sensitivity of the state estimation to variations in the semimajor axis of the orbit of the secondary asteroid [28]
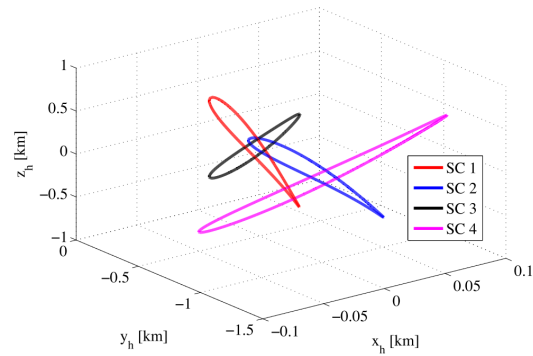

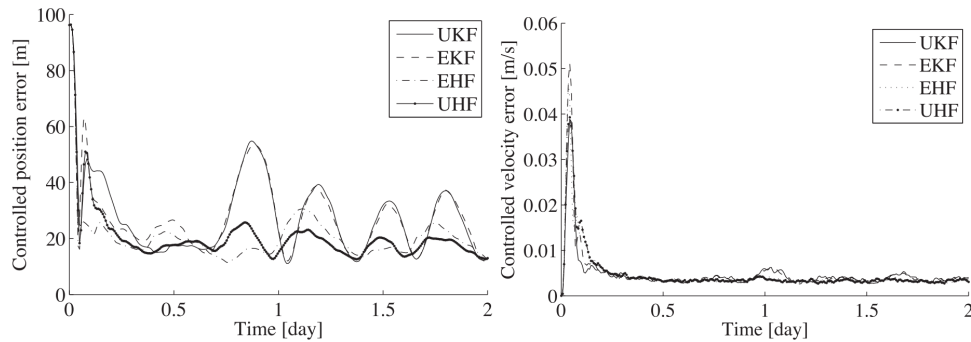**Figure 3.16:** Nominal trajectories flown by the 4 spacecraft in the formation [23]

Figure 3.17: "Controlled (a) position and (b) velocity average RMSE for UKF, EKF, UHF and EHF" [23]

errors. Unmodeled accelerations due to the gravity field of Jupiter, ephemeris estimation errors and the system imaging frequency have a smaller impact. The angles-only solution has a lot of potential if there is good separation of the bodies, preferably at a wide range of positions relative to the spacecraft.

Autonomous navigation of a spacecraft formation in the proximity of an asteroid
By Massimo Vetrisano and Massimiliano Vasile, 2015

The authors of this paper choose a very extensive sensor suite for their asteroid navigation solution. Camera's, Lidar, a Sun Doppler shift sensor, radiometrics and an inter-satellite link for formation flying are all available [23]. The measurement equations following from each of the sensors are described in detail, offering a starting point for the use of these sensors in a different configuration as well.

The performance of different filter types is evaluated and a comparison between four options is made. These options are the UKF, UHF, EKF, and extended H^∞ filter (UHF). The motivation for the H^∞ filter is that unlike the UKF and EKF, it does not require prior assumptions on the nature of the noise in the system. This is therefore a preferred option when the Gaussian hypothesis at the basis of the UKF and EKF cannot be fully guaranteed. However, the UKF is known to work reasonably well when the Kalman filter hypotheses are not fully satisfied.

The target asteroid is modeled as an ellipsoid. The trajectories of the four satellites are shown in Fig. 3.16. The resulting state estimation for the nominal trajectories by the four filters is shown in Fig. 3.17. The UHF is about 20% more computationally expensive than the EHF, but the authors still deem this the best option out of the four due to its superior accuracy and robustness.
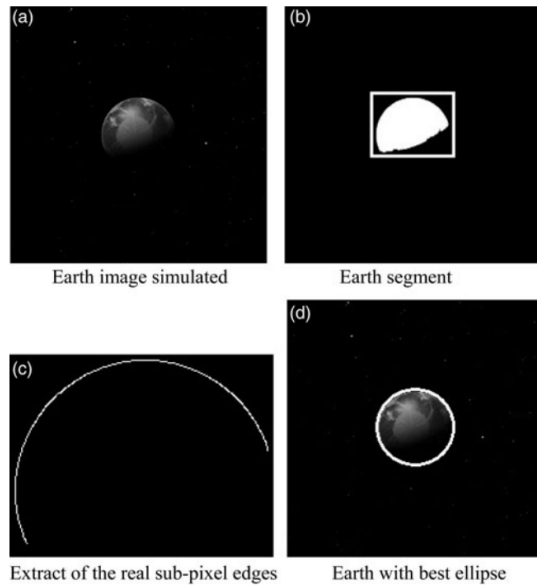
Figure 3.18: "Simulating the Earth image with the planet centroid extracting algorithm" [47]
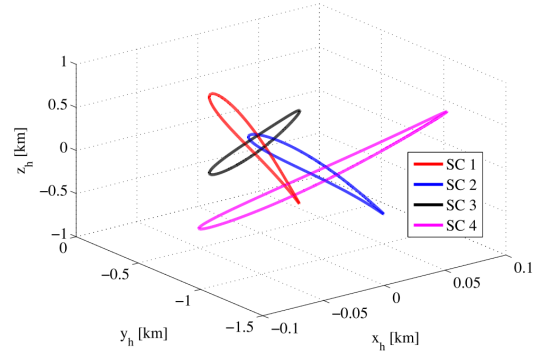

Figure 3.19: "Nominal trajectories" [23]

3.3.3. Image Processing Research

So far, several methods for processing the images from the navigation camera have come up. In [32], first the CoB is determined and then the CoB to CoM transition is made using a mathematical relationship that depends on the direction of the Sun in the detector frame. In [33], the image processing itself is not performed but as a placeholder an estimate of the errors introduced in the image processing and CoM detection in the sensor plane is used. A similar approach is taken in [23]. In the angles-only approach detailed in [28], a limb fitting method is used in combination with binarisation and edge detection.

Given that during the approach phase, the asteroid bodies might be overlapping in the frame and/or partially lit, it is worthwhile to study alternative options for the image processing.

A High-accuracy Extraction Algorithm of Planet Centroid Image in Deep-space Autonomous Optical Navigation
By Siliang Du, Mi Wang, Xiao Chen, Shenghui Fang, and Hongbo Su, 2022
Two different algorithms are presented in this work. A sub-pixel edge-detecting algorithm based on the Prewitt-Zernike moments is developed to detect edge points of objects in the images at the sub-pixel level [47]. Besides this, a planet segmentation algorithm similar to the one in [32] is presented. The sub-pixel edge-detecting algorithm is an improvement over normal edge-detection algorithms. The detected edges can subsequently be used for ellipsoid fitting, as shown in Fig. 3.18.

Centroiding technique using machine learning algorithm for space optical navigation
By Aurelio Kaluthantrige, Jinglang Feng, Jesus Gil-Fernandez, and Andrea Pellacani, 2022
This paper focuses solely on the extraction of the CoM location from images [48]. As a test scenario, they use the binary asteroid (65803) Didymos. The authors show that a Convolutional Neural Network (CNN) based approach, building on the existing HRNet, is robust to Sun phase angle and observations including only part of the asteroid in the frame. Examples of training images that are used are shown in Fig. 3.20. The disadvantages of such a method are the long training times, the generation of a data set that includes enough scenarios of lighting, alignment and location in the frame to make sure the network performs well on every orientation of the two bodies that it might encounter during its deployment. Furthermore, it is difficult to verify the robustness of the solution in face of unforeseen differences between the modeled environment and reality.

Navigation about irregular bodies through segmentation maps
By Mattia Pugliatti and Francesco Topputo, 2021
Another neural-networks centered method is presented in [49]. An onboard method is proposed that can
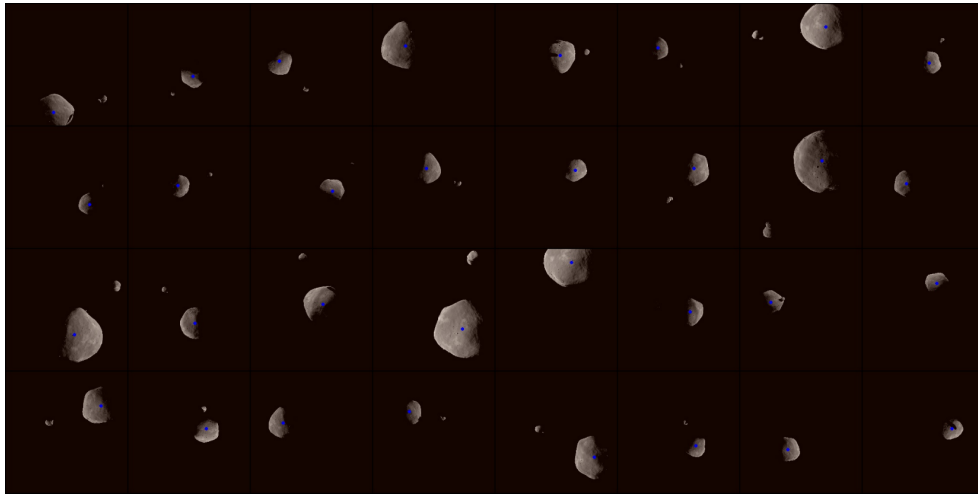
Figure 3.20: "Sample keypoints detection results during training" [48]

estimate the spacecraft position relative to the asteroid directly from images. This strength of this method is in its ability to deal with irregular asteroid shapes, where classical approaches such as limb fitting and Lambertian sphere correlation do not perform very well. A two-step approach is used, in which first a CNN estimates the rough position of the spacecraft, followed by a Normalized Cross-Correlation technique to refine the position estimate. The algorithm is tested on comet 103P/Hartley and the binary asteroid (65803) Didymos. The authors show a position estimate with a relative error between 5 and 8%. Only altitudes between 1.3x and 0.7x the altitude at which the body completely fills the frame were tested. The method relies heavily on assumptions concerning the physical appearance of the target body which is used to train the CNN. Therefore, the applicability of the method is constrained to later stages of the mission where the navigation system can already safely approach the body to distances where surface landmarks can be clearly distinguished.

3.4. NEO-MAPP problem definition

This thesis is written in collaboration with Airbus Defence/Space GmbH in the framework of the NEO-MAPP research project. The navigation filter that is developed in this thesis therefore has to meet the requirements set by the study. This chapter presents the background on the NEO-MAPP project in Subsection 3.4.1, the description of the target asteroid in Subsection 3.4.2, the performance requirements in Subsection 3.4.3, the novelties of the research in Subsection 3.4.4 and finally a conclusion with regards to the research questions in Subsection 3.4.5.

This chapter partially answers RQs 3, 4, and 5.

> **Research Question 3**
>
> What prior knowledge about the asteroid environment is required to estimate the spacecraft state with a given sensor suite?

> **Research Question 4**
>
> What are the performance requirements for the navigation system, and how do these requirements change during the iterative design process?

> **Research Question 5**
>
> Which navigation systems can meet the performance requirements?

3.4.1. NEO-MAPP Research Project

The Near Earth Object Modelling and Payloads for Protection (NEO-MAPP) research project is a European research project for studying planetary defence and asteroid exploration. The reference mission for the NEO-MAPP project is ESA's Hera mission. Hera is ESA's contribution to the Asteroid Impact and Deflection Assessment (AIDA), alongside NASA's DART mission. NEO-MAPP is a standalone study, although most partners involved in Hera are also involved in NEO-MAPP. The target body of NEO-MAPP is the binary asteroid 65803 Didymos.

The NEO-MAPP project concentrates on two topics:

- Maturation or adaptation to specific use cases of existing modelling capabilities regarding the different processes undergone by asteroids (impacts, dynamics, structural evolution).
- Development of instruments, technologies and related data exploitation models to support NEO missions.

The NEO-MAPP objectives include [50]:

1. Pushing the limits of numerical modelling of the response of NEOs to a kinetic impact, as well as of their physical and dynamical properties while maturing European modelling capabilities linked to planetary defence and NEO exploration.
2. Increasing the maturity of multiple spaceborn and landed European instruments directly related to planetary defence, while focusing on measurements of surface, shallow sub-surface and interior properties of NEOs
3. Developing algorithms and simulators to prepare for close proximity operations and payload data analyses and exploitation
4. Developing innovative and synergetic measurement and data-analysis strategies that combine multiple payloads, to ensure optimal data exploitation for NEO missions
5. Developing and validating robust GNC strategies and technologies enabling surface interaction and direct response measurements performed by CubeSat or small/micro-lander architectures

Airbus Defence and Space is responsible for the design of the microlander and its GNC system. The research in this thesis is focused on the design of a vision-based navigation filter for the High-Altitude Phase (HAP) of the landing of this microlander. It is assumed that the microlander detaches from the mothership at 5 km distance from the barycentre of the asteroid system. During the HAP, the microlander approaches a predetermined landing site on the secondary body up to 300 m, as shown in Fig. 3.21. The absolute position of this landing site is known and is chosen based on constraints such as Sun phase angle and surface rotational velocity. Therefore, the HAP Navigation (HAPNAV) filter has to output the absolute position of the microlander. The attitude is assumed to be known from a standard gyrostellar estimator with the star trackers and gyros.

3.4.2. Target Asteroid Description

The most important properties of the Didymos system are given in Table 3.3.

Table 3.3: Overview of (65803) Didymos properties.

| Parameter	Value	Reference
Official minor planet number of primary	65803	[51]
Official name of primary	Didymos	[51]
Method of discovery of companion	Photometric lightcurve	[51]
Diameter of Primary D_p	0.780 km $\pm$ 0.03 km	[52]
Diameter of Secondary D_s	0.164 km $\pm$ 0.018 km	[See D_s/D_p below]
Bulk density of the primary ρ_p	2170 kg m^{-3} $\pm$ 350 kg m^{-3}	[from shape model M_{tot}]
Distance between the centre of primary and secondary	1.19 km $\pm$ 0.03 km	[52]
Total mass of system	5.278 $\times 10^{11}$ $\pm$ 0.54 $\times 10^{11}$ kg	[53]
Rotational period of the primary	2.2600 h $\pm$ 0.0001 h	[54]
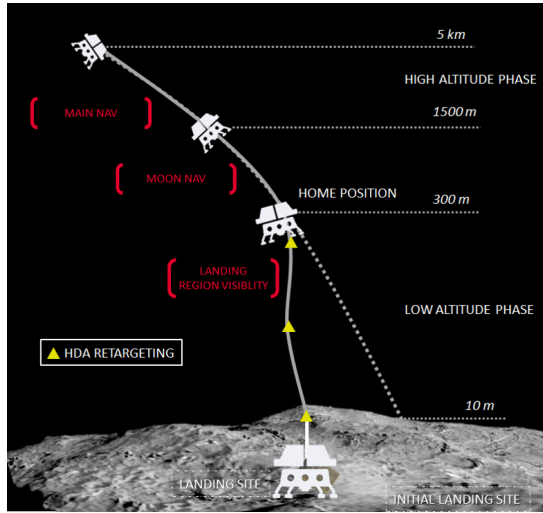
Figure 3.21: Landing phases in NEO-MAPP
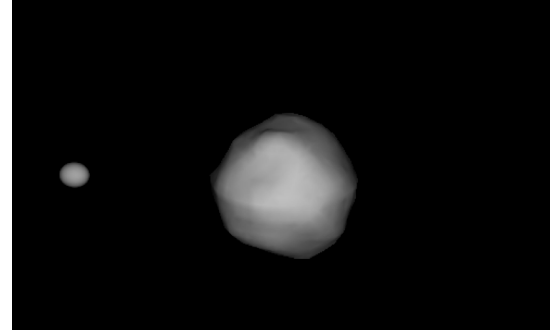
Figure 3.22: Shape model of Didymos and its moon Dimorphos, based on photometric light curve and radar data. (Credit: Naidu et al., AIDA Workshop, 2016)

Furthermore, $M_s/M_p = V_s/V_p = (D_s/D_p)^3 = (0.21 \pm 0.01)^3 = 0.0093 \pm 0.0013$. From radar observations, a rough shape model is available [52]. A render showing these shape models is shown in Fig. 3.22.

3.4.3. Performance Requirements

The landing zone is predefined based on a number of criteria and is located at the pole of the secondary asteroid facing to the outside of the binary system. This location is selected based on the scientific interests of the study. Furthermore, at this location the illumination properties are favourable. The landing zone is defined in an absolute reference frame and therefore the navigation solution that navigates the spacecraft towards the home position shown in Fig. 3.21 must also estimate the absolute state of the spacecraft. The available sensor suite is limited to a single navigation camera, 3-axis accelerometers, one or more laser range finders, star trackers and rate gyros.

The mission Interface Control Document (ICD) compiles a list of requirements on the system. A list of requirements relevant to this research work has been compiled and is shown in Tables 3.4 and 3.5.

3.4.4. Research Novelties

Several components of this research can be considered novel and add to the body of scientific research. First of all, this particular sensor suite is not commonly used in the literature. Besides this, the mission scenario assumes that the mothership has relayed updated ephemeris information to the μlander. Because the landing zone is at the outer pole of the secondary asteroid, the primary will be visible behind the secondary body as seen in Fig. 3.24. This makes angles-only navigation such as investigated by [28] impossible due to the lack of separation of the bodies. However, in other phases of the flight both asteroid bodies will be visible in the camera frame, as seen in Fig. 3.23. This research work aims to extract information about both the primary and secondary from these images, instead of taking the common approach in literature where one of the two bodies is removed by the image processing algorithm and only a single measurement remains. The use of a laser range finder in combination with visual information has been studied before, especially in combination with landmark tracking for absolute navigation [55]. In this case, the laser range finder will be used without a high-fidelity model of the surface available.

3.4.5. Conclusion on Research Questions

This chapter partially answered RQs 3, 4, and 5. The information that contributes to answering these RQs will now be reviewed.

Table 3.4: Mission requirements table

| ID	Title	Description
LAN-MIS-0040	Initial Conditions Single Asteroid	At separation of the µLander from the orbiter and initialisation of the landing activity the following pre-conditions shall apply: Position in the inertial J2000: Value Accuracy TBD +- TBD Velocity in the inertial J2000: TBD+- TBD
LAN-MIS-0050	Initial Conditions Binary System	At separation of the µLander from the orbiter and initialisation of the landing activity the following pre-conditions shall apply: Initial distance in I-frame in the range $[5,8] \pm 0.05\,km$ Initial velocity in the I-frame in the range: $$[7,14] \pm 10\% \frac{cm}{s}$$
LAN-MIS-0090	Mission Phases	The µLander shall support all mission phases from separation to landing.
LAN-MIS-0160	Mission Autonomy	The lander shall be autonomous in every mission phase from deployment until landing both nominal and contingencies
LAN-MIS-0170	Failure Tolerance Approach	Single point failure tolerance shall be applied to all the system and subsystem
LAN-MIS-0180	Descent Trajectory	The lander should be capable of following a programmed trajectory.
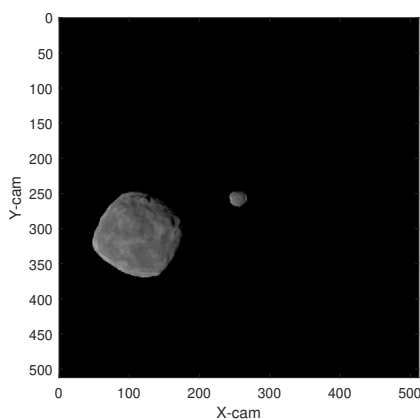
Figure 3.23: View through the navigation camera at 5 km altitude. Own work, rendered in PANGU.
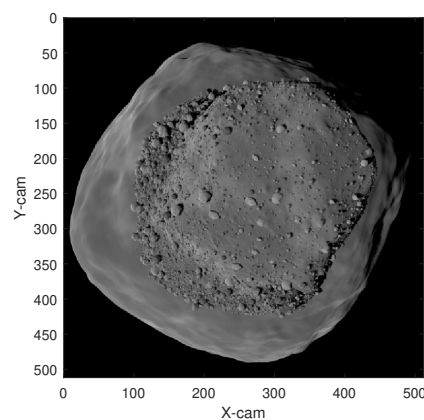
Figure 3.24: Same scenario, now from 300 m altitude. Own work, rendered in PANGU.

Table 3.5: System requirements table

ID	Experiment	Objective
T2.1	Autonomous visual based navigation for semi-autonomous attitude guidance	Position knowledge error (any axis) lower than 100 m relative to the centre-of-mass of Didymos with 95% probability. Contribution of attitude guidance to APE lower than 0.5 deg (95 %probability). NOTE: This includes the autonomous navigation error.
T2.3	Autonomous visual based navigation for trajectory guidance	Position knowledge error (any axis) lower than 10% distance to the target asteroid with 99.7% probability, 90% confidence level. Altitude error at closest distance lower than 20% of nominal altitude with 99.7% probability. Attitude Pointing Error relative to the surface point of interest lower than 1 deg (95% probability).
T2.4	Sensor data-fusion for robust navigation	At least the same as the equivalent vision-based navigation solution.

> **Research Question 3**
>
> What prior knowledge about the asteroid environment is required to estimate the spacecraft state with a given sensor suite?

What exact prior knowledge and assumed parameters of the asteroid environment are required for a successful state estimation is still unknown. However, the given sensor suite is now known to be a single navigation camera, 3-axis accelerometers, one or more laser range finders, star trackers and rate gyros.

> **Research Question 4**
>
> What are the performance requirements for the navigation system, and how do these requirements change during the iterative design process?

The navigation solution shall provide an estimate of the absolute state of the spacecraft that is up to the requirement specifications presented in Tables 3.4 and 3.5. The 3σ position knowledge error for any axis shall be below 10% of the distance to the target asteroid. The initial distance to the asteroid in the I-frame shall be in the range $[5,8] \pm 0.05$ km. The initial velocity in the I-frame shall be in the range $[7,14] \pm 10\%$ cm/s. The final altitude above the outward facing pole of the asteroid during the high altitude phase shall be such that the low altitude navigation system can take over. There is some flexibility in this last requirement, because it is unknown at this stage what altitude can be reached with the high altitude navigation system. The minimum distance that can be reached is 300 m above the surface of the secondary asteroid, because at this altitude the asteroid will fill the complete FOV of the camera. Centroid-based navigation will become impossible once this threshold altitude is crossed.

> **Research Question 5**
>
> Which navigation systems can meet the performance requirements?

While no in-depth answer to this question is given, the performance requirements are now established. The only navigation solutions that satisfy the performance requirements are those that meet all accuracy requirements with the given sensor suite.

3.5. Thesis outlook

This chapter presents a summary of the literature study report so far and presents the outlook for the rest of the thesis. First, the motivation for the research is once again presented in Subsection 3.5.1. A trade-off of different navigation methods is presented in Subsection 3.5.2, which leads to a conclusion on what the navigation filter to be developed in this work will look like.

3.5.1. Motivation for the Research

The motivation for this research is two-fold. On the one hand, there is a practical need for a navigation solution for the high-altitude phase within the NEO-MAPP research project. The available sensors, the required performance and the prior knowledge that can be exploited by the navigation filter are all predetermined.

From a more scientific perspective, this work adds to the scientific research on asteroid navigation. The use of the information gathered by the mothership onboard of the μlander and the autonomous nature of the navigation solution are similar to a scenario that is often encountered in science and asteroid mining mission concepts. The specific asteroid environment that is studied in this thesis is a binary asteroid. While this complicates the environment simulation and vision-based navigation, it also brings valuable opportunities to innovate in the navigation system by exploiting the binary nature of the target asteroid.

Several related studies with similar mission concepts have been conducted before. For instance, [32] proves that the state relative to the asteroid can be estimated at the cost of augmenting the state vector of the filter with the gravitational parameter and a parameter depending on the illumination conditions.

Table 3.6: Overview of filter types in reviewed literature

Paper	Filter Type	Comment
[32]	UKF	UKF is heavy, could be improved with partial EKF in the propagation step
[33]	EKF, IKF	EKF used for position estiation, IKF for design of the ΔV maneuvre
[28]	UHF	Good compromise between robustness and coputational complexity
[29]	EKF	-
[23]	EKF, EHF, UKF, UHF	The choice of the H^∞ filter is preferable when the Gaussian hypothesis cannot be fully guaranteed, for example when biases in the instruments are not detected

The secondary asteroid in the binary system is completely disregarded and no ranging sensors are used, leading to a rough estimate of the position with large error bounds. In [33], scale invariance problem is solved through a navigation strategy that is coupled with a guidance algorithm that designs ΔV maneuvers. The authors also investigate the use of not just the line-of-sight measurement, but also the size of the asteroid on the image sensor to extract range information. An approach that relies completely on the binary nature of the asteroid by processing two line-of-sight measurements is presented in [28]. Taking this approach one step further by observing even more objects in the frame, [29] compares four different navigation filter architectures their navigation performance when relying on line-of-sight measurements to the moons of Jupiter. The authors of [23] include a swarm of satellites in their analysis with a very broad sensor suite, leading to excellent results and a good comparison of four different Kalman filter architectures.

This research will build on these prior studies by combining several prior study results. The approach of [32] will be augmented by adding the exploitation of the measurements from the binary asteroid system from [28], combined with the range information acquisition with a laser range finder from [23].

3.5.2. Trade-Off of Navigation Methods from Literature

An overview of the navigation methods in the literature is shown in Table 3.6. An overview of the sensors used in these papers is given in Table 3.7.

For the filter that is to be developed in this research work, the EKF will be used at first. It has shown good results in comparable navigation filters and the improvements by going to an UKF or UHF might not be required to meet the requirements of the NEO-MAPP study. An augmented version of [32] that includes the laser range finder measurements, as well as double line-of-sight measurements from both the asteroids is going to give a starting point for the navigation filter. If necessary, the angular size information can also be included, given that enough knowledge is available on the size of the objects in the frame.

Table 3.7: Overview of sensors used in reviewed literature

Paper	Sensors	Comment
[32]	Camera, Sun sensor	S/C to Asteroid vector found using mathematical relationship to compensate for lighting conditions. This relationship relies on knowledge of the Sun direction.
[33]	Camera, accelerometer	ΔV ranging used to break scale invariance. Could also be done with LRF/Lidar, removes navigation/guidance coupling.
[28]	2x camera, Sun sensor, star trackers	Assumes navigatin around L4 of binary asteroid system (ideal scenario in terms of body separation)
[29]	Accelerometer, camera, star trackers	Attitude changes to observe all moons one by one. Key finding: the more moons at different relative positions, the more accurate the state estimation.
[23]	Camera, Lidar, Sun Doppler shift, radiometrics antenna, inter-satellite link	Very elaborate sensor suite including radiometrics. Good documentation on use of sensors (measurement equations, noise characteristics).

<div align="right">

4

</div>

Preliminary Work

4.1. Simulator implementation

A first look at the simulator that will be used as an environment to test the navigation filter solution is included in the literature study. The goal of this exercise is to deepen the understanding of the problem by getting hands-on experience, while also producing valuable preliminary results which are at the basis of the technical work of the thesis. This work is related to RQs 2 and 3:

> **Research Question 2**
>
> What are the requirements for a simulator that can be used to develop the navigation system?

> **Research Question 3**
>
> What prior knowledge about the asteroid environment is required to estimate the spacecraft state with a given sensor suite?

The start of the technical work is split up in three parts. In Subsection 4.1.1, a high-level overview of the simulator architecture is given. Subsection 4.1.2 explores the disturbances present in the environment of the binary asteroid. Finally, Subsection 4.1.3 presents a detailed analysis on the gravity fields of the asteroid, followed by a conclusion of the preliminary simulator work in Subsection 4.1.4. The contributions of this chapter to the answering of the research questions is discussed in Subsection 4.1.5

4.1.1. High-Level Overview of the Simulator

A simulated environment will be used to develop and test the navigation solution. This simulator will provide the navigation filter with its inputs, and can then be used to compare the navigation filter estimated state to the "real" state. In Fig. 4.1 an overview of the components of the simulator is given. Each individual component will now be discussed.

Environment

The simulator includes an environment that the spacecraft will fly through during the HAP. This includes the gravity fields of both asteroids, perturbing forces from other solar system body gravity fields and the solar radiation pressure (SRP). This is the part of the simulator that is studied during this literature study phase. The precise position and velocity of the two asteroid bodies, perturbing planets are calculated in the J2000 frame. This reference frame has its origin in the solar system barycenter. Besides that, the angular position and rate are included. The transformation matrices and attitude quaternions in various relevant reference frames are calculated too. This is all done based on the NASA JPL SPICE kernels which contain the most up-to-date information about the ephemeris of the bodies in the solar system.

Reference Frames

Several reference frames are used in the simulator for different reasons. These are summarized in Table 4.1. A visual representation of the frames is shown in Fig. 4.2.
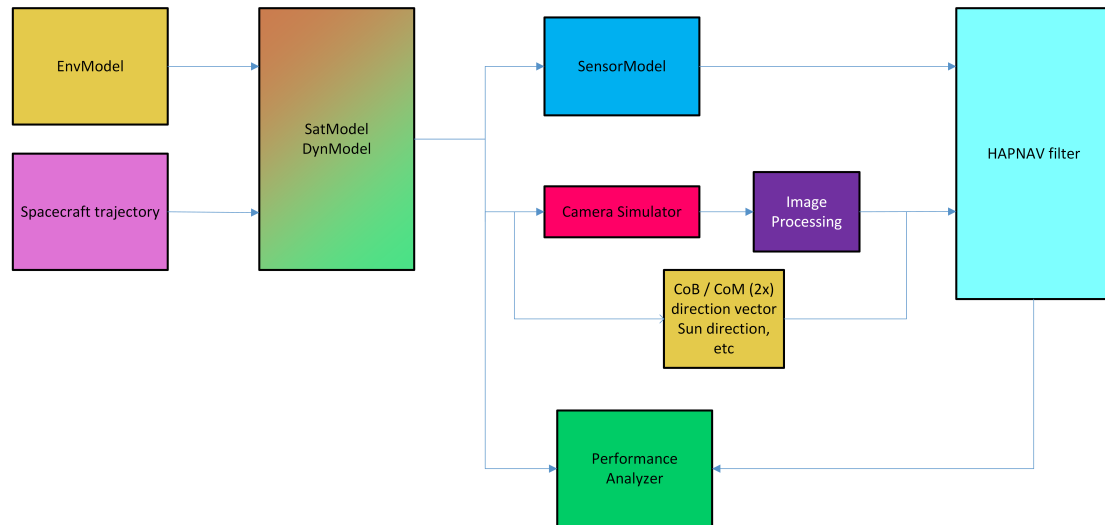
Figure 4.1: Schematic diagram of the different components of the HAPNAV simulator.

Table 4.1: Description of reference frames used in the simulator.

| Name	Definition	Center & axes	Comments
J	J2000	Solar System barycenter Z: aligned with Earth's rotation X: mean equinox Y: complete right-handed system	Describe the orbit of the binary system Describe the Sun position Defines initial conditions for landing
I	J2000	CoM of binary system X, Y, Z same as J2000	Describe orbit of the Didymos system Describe the landing trajectory
P	Primary fixed	CoM of primary Z: maximum MoI X: minimum MoI Y: complete right-handed system	Rotates with the primary body
S	Secondary fixed	CoM of secondary Z: maximum MoI X: minimum MoI Y: complete right-handed system	Rotates with the secondary body
B	Spacecraft fixed	CoM of spacecraft X, Y, Z oriented with principal inertia axes	Describe the attitude Describe the sensors/actuators positions Z axis is the camera line of sight
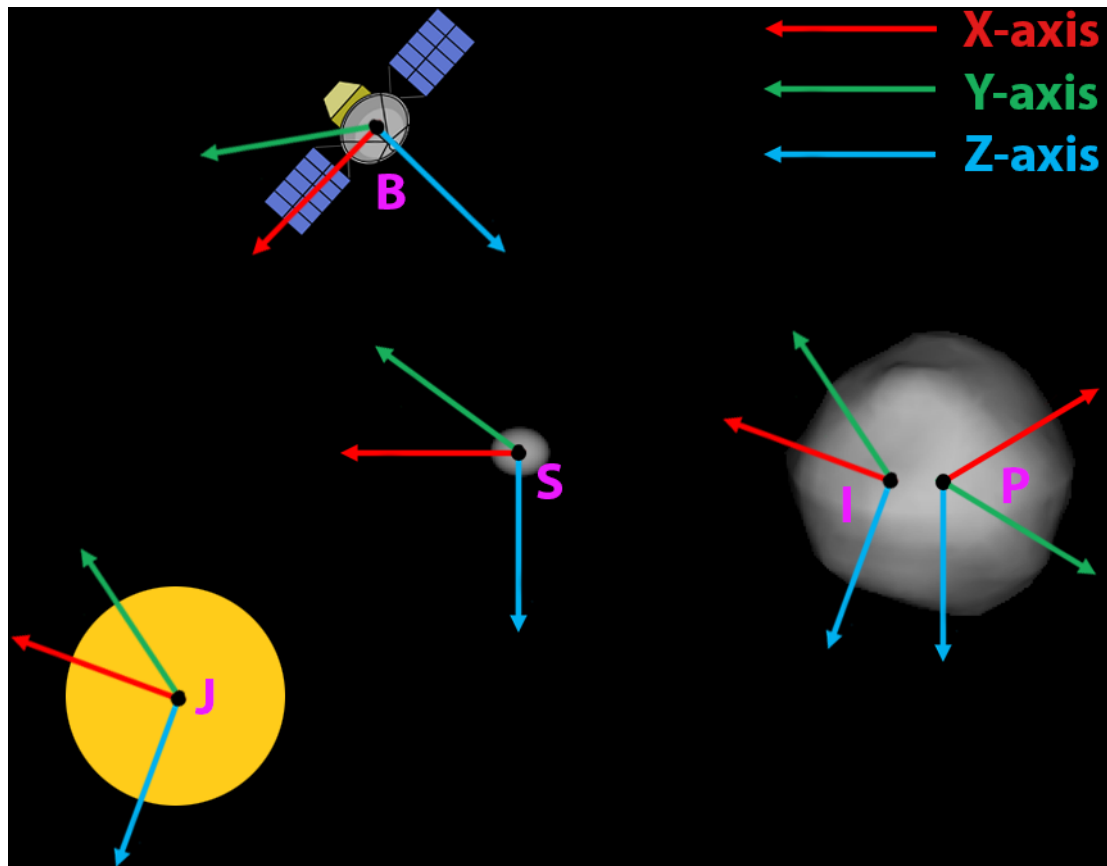
Figure 4.2: Reference frames used in the simulator. Asteroids image by NASA/Naidu et al., AIDA Workshop, 2016.

Spacecraft Trajectory
Besides the environment, the satellite also needs a trajectory to follow. The spacecraft has complete control authority, meaning that it can move in any direction including those against the forces that are presented by the environment. A logical choice for the guidance is therefore to enforce a certain acceleration profile from an initial condition. Then the control part of the problem is cut out. Besides this, the dynamics are easier to model because the interaction of the thrusters and the control system is removed.

Sensors Model
The `SensorModel` block contains models for the noise and bias characteristics of the sensors used on board of the spacecraft. The camera simulator is especially important here because it generates the images that are used by the image processing algorithms. These algorithms extract information such as the center of brightness of the asteroid bodies in the frame or the Sun direction. These measurements are then used in the navigation filter. An alternative is to simulate the camera and image processing by directly reconstructing the measurements that could be generated from camera images. The advantage of this approach is that the navigation filter can be tested without setting up the camera simulator and the image processing. This could be used in the development of the filter. Ultimately, the camera simulator must create the images and the image processing must extract the information, as this is how the system will be used in real life.

HAPNAV Filter
The navigation filter that processes the measurements into a state estimate. What the state vector, measurement vector and type of filter exactly will be is still undecided. However, at the very least the absolute position in J2000 frame must be estimated to match it to the landing zone coordinates.

Simulator Validation Plan
Each component of the simulator must be verified and ideally also validated to make sure it is implemented correctly and functioning as intended. Because no hardware-in-the-loop testing is envisioned at this stage, validation is difficult. The current plan only exists for the gravity models implementation and the orbit propagator. These can be validated by swapping out the gravity models of the asteroids with those for Earth, which is known very precisely. By integration of a known satellite trajectory, the output can be compared to real flight data from literature.

Verification tests can be performed at many stages by checking that the results of components of the simulator make sense and provide the expected solution.

4.1.2. Analysis of Accelerations and Disturbances
In the binary asteroid environment, there are many external forces acting on the spacecraft. Besides the gravity fields of the primary and secondary body, there are other disturbing celestial bodies (Sun, Earth, Moon) that exert forces on the spacecraft. The photons emitted on the Sun interact with the spacecraft surface to create a disturbance force, the solar radiation pressure. The simulator can take into account all these effects, however this does add complexity and computational load. A simple analysis of these forces is presented in this section, with the goal of determining which factors will be included in the final simulator. A threshold for the magnitude of a disturbance acceleration is defined, below which all effects are neglected.

Several assumptions are made in this analysis:

- A point mass gravity model is assumed for all bodies
- The orbits of the two asteroids around each other are circular, therefore the distance between them is constant.
- The celestial bodies are assumed to be on a line, positioned such that their influence is largest (i.e. their closest position relative to the binary system). See Fig. 4.3.
- The projected area of the satellite remains constant, there are no attitude changes.
- Solar System bodies other than the Sun and Earth are not studied.
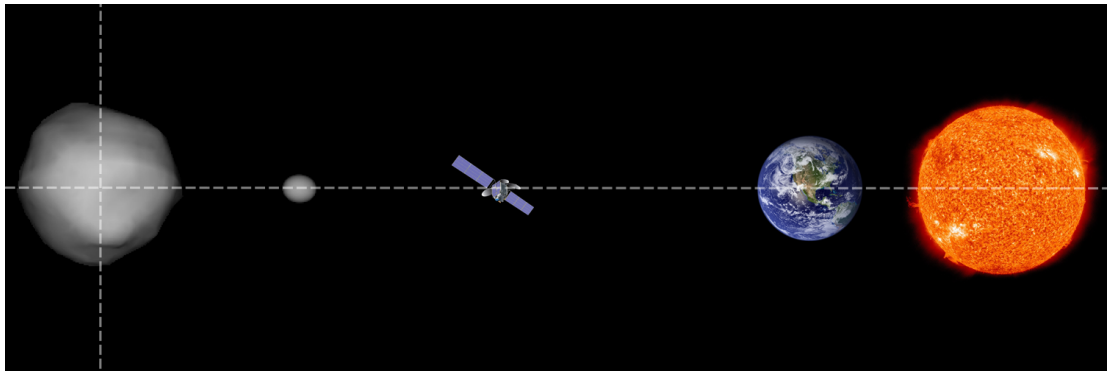
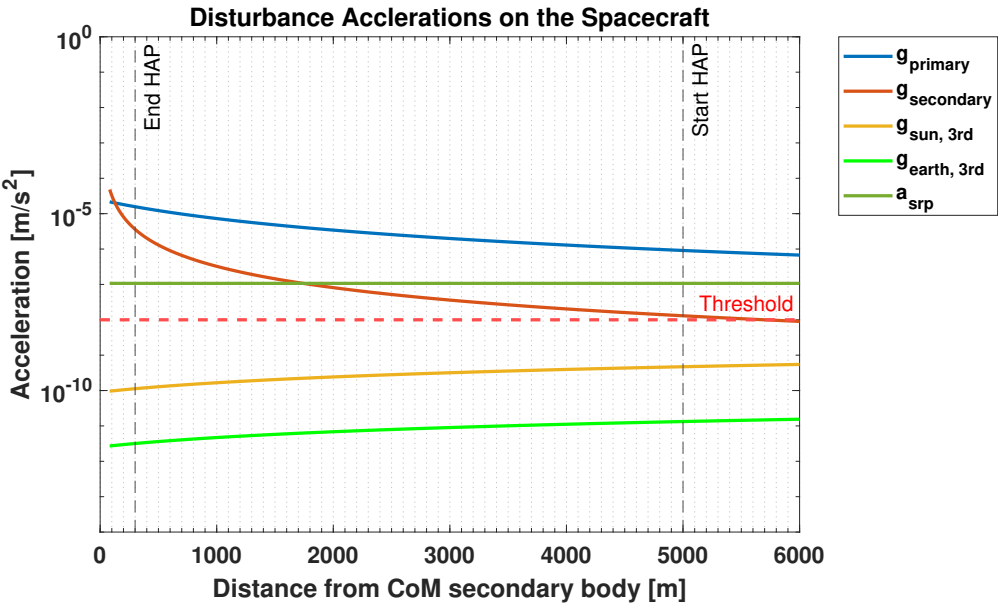**Figure 4.3:** Schematic diagram of the distance assumptions made in the disturbance analysis (not to scale).

Figure 4.4: Disturbance accelerations on the spacecraft as a function of the distance to the CoM of the secondary asteroid.
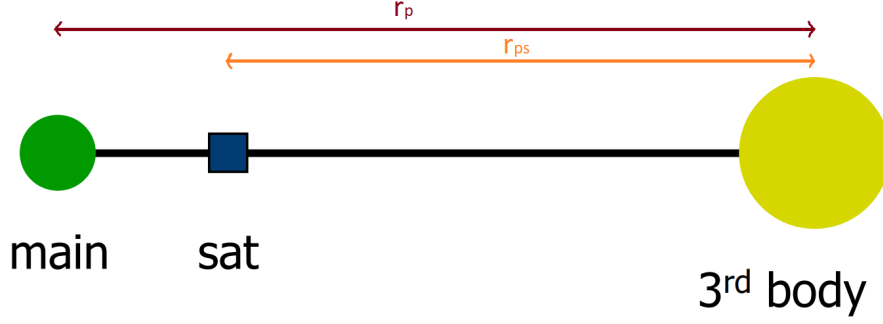
Figure 4.5: Sketch of the relevant parameters in the third body acceleration calculation.

Primary and Secondary Asteroid Gravity

The dominant accelerations in the HAP are the gravitational accelerations of both the primary and the secondary body. The gravity field of the primary dominates up until about 125m from the surface of the secondary. The gravitational acceleration a_b experienced by the spacecraft at a distance of r_{bs} from the CoM of the asteroid b is calculated using Eq. (4.1).

$$a_b(r_{bs}) = GM_b \left(\frac{1}{r_{bs}^2} \right) \tag{4.1}$$

Third-Body Gravity

Other solar system bodies pull on the binary asteroid system as well as the spacecraft. The effect of this so-called third-body perturbation a_p is calculated using Eq. (4.2). It is assumed that the perturbing body, the spacecraft, and the binary system are on a single line. This is shown in Fig. 4.5.

$$a_p = GM_p \left(\frac{1}{r_{ps}^2} - \frac{1}{r_p^2} \right) \tag{4.2}$$

Solar Radiation Pressure

Because the spacecraft is not flying in the shadow of any object, it is subject to a disturbance force from the solar radiation. All light particles carry linear momentum, which reflects off the surface of the spacecraft. The surface reflectivity ρ determines what happens to the particles that hit that surface. If $\rho = 1$, the particles are absorbed. If $\rho = 2$, they are reflected. A perfectly transparent surface will have $\rho = 0$. In this study the spacecraft is assumed to have a coefficient of reflectivity of 1.2. The surface area perpendicular to the direction of radiation is 1 m^2.

The solar radiation pressure can be calculated using Eqs. (4.3) and (4.4) [56].

$$\frac{ma_{sun}}{A_\perp} = \rho p_{sun} \tag{4.3}$$

where

$$p_{sun} = \frac{E}{c} = p_0 \left(\frac{r_\oplus}{r} \right)^2 \tag{4.4}$$

with

$\rho = 1.2$	[-]	coefficient of reflectivity
$c = 2.9979 \times 10^8$	[m s^{-1}]	speed of light
$E = (1372 \pm 45) \left(\frac{r_\oplus}{r} \right)^2$	[W m^{-2}]	intensity of solar radiation (seasonal)
$p_0 = (4.58 \pm 0.15) \times 10^{-6}$	[N m^{-2}]	solar radiation pressure at 1 AU (seasonal)
$r_\oplus = 1.4962 \times 10^8$	[km]	mean radius of Earth's orbit
$A_\perp = 1$	[m^2]	surface of the spacecraft projected in the Sun direction

4.1.3. Gravity Field Analysis

Precise modelling of the gravity field of asteroids is especially important because their shapes are often highly irregular, leading to large deviations from the simple point mass gravity model. More advanced gravity field modelling techniques exist, which aim to approximate the real gravity field of a body. The two gravity models that will be studied are the spherical harmonics expansion and the polyhedron potential models. This exercise will answer the following two questions:

1. How large is the deviation of a more precise gravity model from the point mass gravity model?
2. What is the effect of this deviation on the spacecraft?

Spherical Harmonics Expansion

This well-known gravity model uses periodic functions to describe the gravity potential at any point around the sphere. The general equation to describe the gravity potential according to the spherical harmonics model is given in Eq. (4.5) [57]. The gradient of the potential gives the gravitational acceleration.

$$U = \frac{\mu}{r} \sum_{l=0}^{\infty} \left(\frac{a_e}{r}\right)^l \sum_{m=0}^{l} P_{l,m}(\sin\phi)[C_{l,m}\cos m\lambda + S_{l,m}\sin m\lambda] \qquad (4.5)$$

where

$\mu = GM$	[m^3 s^{-2}]	gravitational parameter
a_e	[m]	semi-major axis of body's reference ellipsoid
r	[m]	spacecraft distance
ϕ, λ	[rad]	spacecraft latitude and longitude, body-fixed
$C_{l,m}, S_{l,m}$	[-]	spherical harmonic coefficients of degree l and order m
$P_{l,m}$	[-]	Associated Legendre Functions of degree l and order m

The model is only accurate outside of the reference radius a_e. We see that the leading part is simply the potential resulting from treating the body as a point mass. Then there are the terms which do not have a dependence on the latitude λ, corresponding to $m = 0$. These form the zonal contribution to the potential, given by Eq. (4.6). The degree-1 term is zero if it is assumed that the coordinate system coincides with the body CoM.

$$U = \frac{\mu}{r} \sum_{l=1}^{\infty} \left(\frac{a_e}{r}\right)^l P_{l,0}(\sin\phi)C_{l,0} \qquad (4.6)$$

The remaining part contains the tesseral and sectorial contributions, given by Eq. (4.7). A visual representation of the zonal, tesseral, and sectorial contributions is shown in Fig. 4.6.

$$U = \frac{\mu}{r} \sum_{l=1}^{\infty} \left(\frac{a_e}{r}\right)^l \sum_{m=1}^{l} P_{l,m}(\sin\phi)[C_{l,m}\cos m\lambda + S_{l,m}\sin m\lambda] \qquad (4.7)$$

In the case of the asteroids, there are no tidal effects such as on Earth. This results in coefficients that do not vary with time. Important to note is that the coefficients are usually normalized, because they vary so much in magnitude. It is important to understand which normalization is used when a set of coefficients is supplied, because they might have to be re-normalized to be used by an existing spherical harmonics implementation. In this case, the coefficients were provided by the university of Bologna team working on the gravity fields of Didymos. They have used the 4π normalisation technique, which is also used by the Airbus spherical harmonics Simulink block. This was verified by comparing the JGM3 and EGM96 gravity model coefficients which were known to be 4π normalized to the coefficient files supplied by Airbus. The 4π normalization convention for Associated Legendre Functions is given in Eq. (4.8) [58].

$$\bar{P}_{lm}(\mu) = \sqrt{(2 - \delta_{m0})(2l + 1)\frac{(l - m)!}{(l + m)!}} P_{lm}(\mu) \qquad (4.8)$$
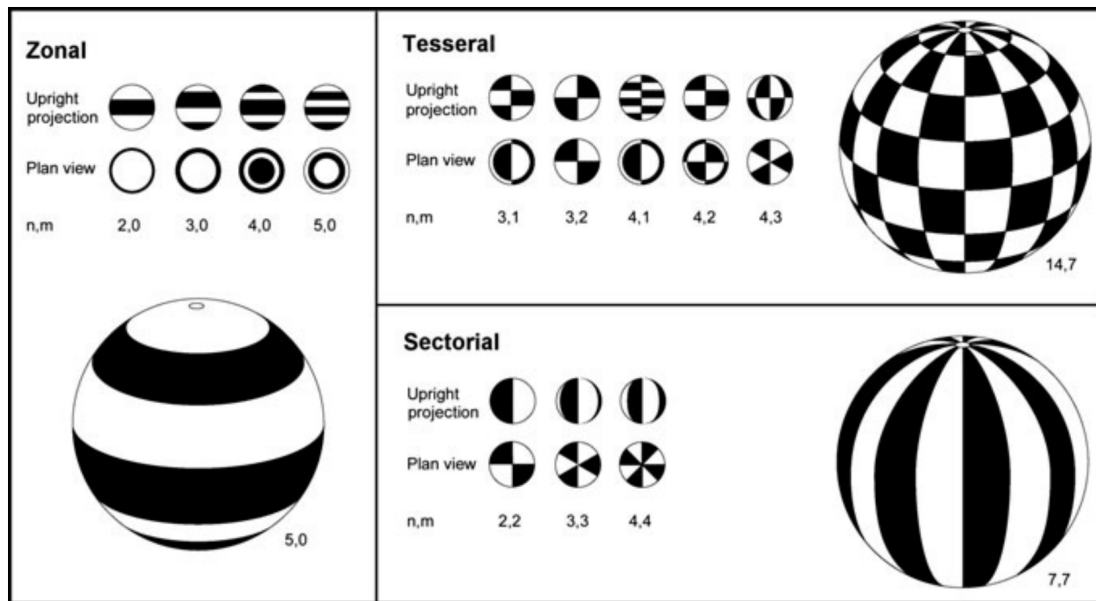
Figure 4.6: The nodal surfaces of spherical harmonics of degree n and order m: zonal harmonics, tesseral harmonics, and sectorial harmonics [56].

Table 4.2: Adjusted densities used in the polyhedron gravity calculation to match the total body mass to that of the HERA reference document.

Object	Adjusted density kg/m^3
Didymos	2107
Dimorphos	2104

For Didymos, the coefficients are provided up to degree 20. Due to poor visibility from Earth of the secondary body, the coefficients for Dimorphos are provided up to degree 2.

Polyhedron Gravity Potential

The polyhedron gravity potential method builds on principles from 3d modelling. An `.obj` file is provided, consisting of vertices, faces and face normal vectors. These `.obj` files are attached with the HERA Didymos Reference Model [59] and are shown in Fig. 4.7.

The `.obj` files can be transformed into a gravity field by assuming that the density of the object is known, as described in [60]. The reference model quotes a uniform density of 2170 kg/m^3. To guarantee that at far range the gravity models all give the same result, the same mass must be used for the bodies. To check the mass that was assigned by using the density of 2170 kg/m^3, a script to calculate the volume of the `.obj` file is used. It was found that the density must be slightly lowered to reach the mass given in the reference document. These factors are given in Table 4.2.

Fig. 4.8 shows the magnitude of the gravity vector in the XY-plane at $Z = 0$ of the binary system. Advantages and disadvantages of the polyhedron gravity model include:

+ Representing the gravity field close to the surface is possible, there is no minimum distance such as the reference sphere in the spherical harmonics model.

+ Computationally efficient once the gravity lookup table is calculated.

- Constant density assumption could introduce errors.

- Heavy computations to generate the lookup table.

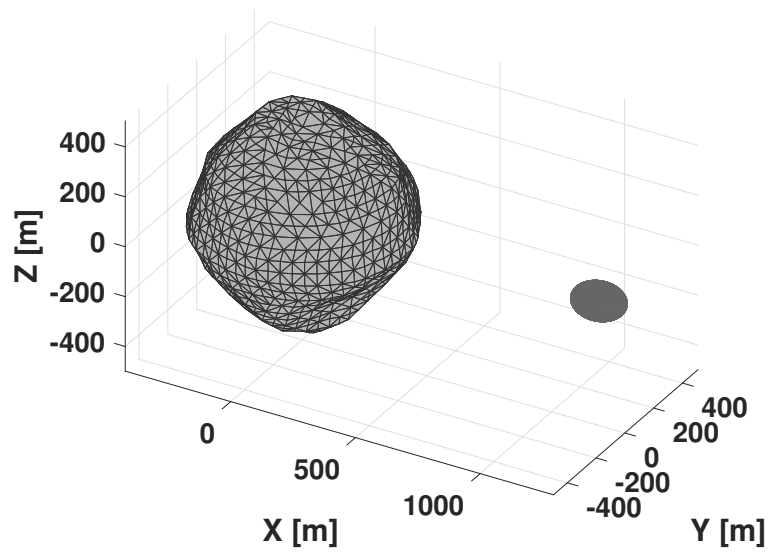- No solution for every point, relies on interpolation between pre-calculated grid points.

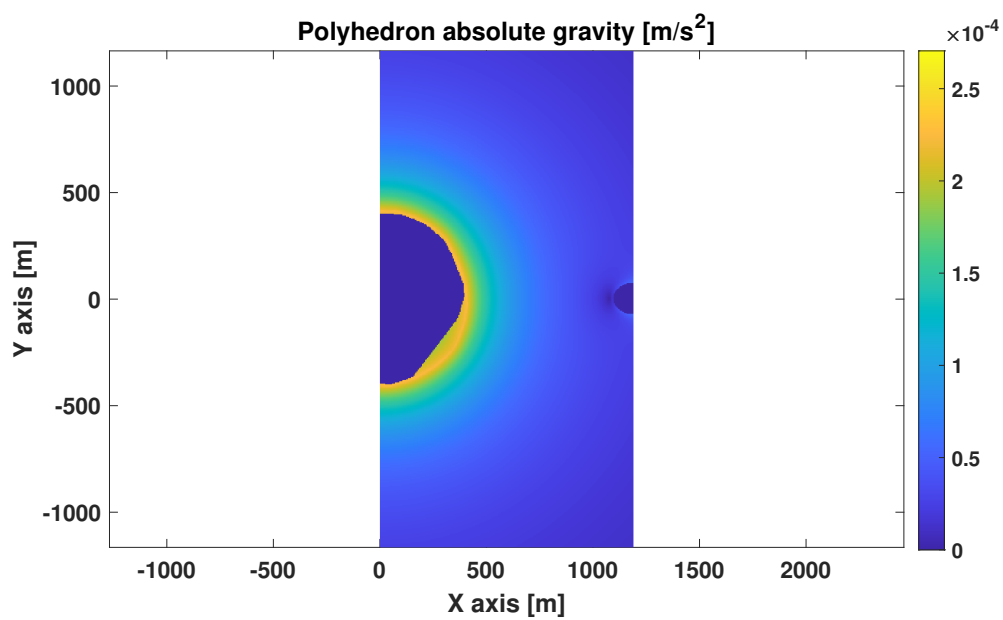**Figure 4.7:** Didymos and Dimorphos `.obj` files.

Figure 4.8: Magnitude of gravity vector according to the polyhedron model.

4.1.4. Simulator Implementation Results and Conclusion

After this preliminary simulator work, it's important to summarize the findings and conclude this part of the literature study. This conclusion will again be split up in three parts, namely the high-level simulator overview, the disturbance acceleration analysis and the gravity fields analysis.

High-Level Simulator Overview

The outcome of this activity is a first version of the architecture of the simulator. It has become clear that there are several choices to be made during the development. To allow intermediate testing of components of the simulator, it is desirable to make assumptions and simplifications during the development. This can for instance be to skip the camera simulator and image processing in the beginning and directly provide the HAPNAV filter with the measurement that would come out of this image processing. One could also think of providing the perfect attitude knowledge with some (known) added noise to the filter, instead of merging the gyro-stellar estimator with the vision-based position estimator. This means that the implementation of the gyro-stellar estimator will not hold back the development of the vision-based navigation solution.

The validation plan will need to be updated as the development continues, by including validation tests for the individual components. For now, a validation plan for the gravity models and orbit propagator exists.

Analysis of Accelerations and Disturbances

The gravity of the primary body is the dominant acceleration acting on the spacecraft during the entire HAP. Even if the approach trajectory of the spacecraft is not the straight line as sketched in Fig. 4.3, this will still be the case. The gravity of the secondary body is much smaller, so small that for the majority of the HAP the solar radiation pressure causes a stronger disturbing effect. The threshold is set at 10^{-8} m/s^2. Any disturbing acceleration below this threshold will not be modelled in the simulator. Assuming that this acceleration is acting on the spacecraft from standstill, after a four hour flight time the accumulated displacement would be $x = \frac{1}{2}at^2 = 1.0368$ m.

Gravity Field Analysis

The goal of this analysis was to answer the following two questions:

1. How large is the deviation of a more precise gravity model from the point mass gravity model?

2. What is the effect of this deviation on the spacecraft?

To start with the first question, the gravity fields generated by two different models are compared to one another. The magnitude of the error vector at every point of a XY-plane slice through the two bodies at $Z = 0$ is calculated. The error vector for two gravity fields A and B is calculated according to Eq. (4.9). The relative error is also used, as defined in Eq. (4.10). $e_{g,rel}(x, y, z)$ is the magnitude of the gravity vector at point (x, y, z).

$$e_g(x, y, z) = \begin{bmatrix} g_x^A(x,y,z) - g_x^B(x,y,z) \\ g_y^A(x,y,z) - g_y^B(x,y,z) \\ g_z^A(x,y,z) - g_z^B(x,y,z) \end{bmatrix} \tag{4.9}$$

$$e_{g,rel}(x, y, z) = \frac{|e_g(x,y,z)| - g^A(x,y,z)}{g^A(x,y,z)} \times 100\% \tag{4.10}$$

The result of this analysis is shown in Fig. 4.9. Now the two questions that this exercise was meant to answer will be answered.

How large is the deviation of a more precise gravity model from the point mass gravity model?

During the HAP, the secondary body will be approached from the $-X$ direction, far away from the primary asteroid. The trajectory will not be exactly along the $-X$ direction, and the trajectory is ultimately in 3D meaning that also the Z component of the gravity field is important. However, it is safe to say that the region where the polyhedron and spherical harmonics gravity models differ most from that of the point mass are avoided during the approach. When measured at $y = 0, z = 0$ at 300 m distance from the surface of the secondary asteroid, the polyhedron model gives an error of 4.46×10^{-8} and the spherical harmonics
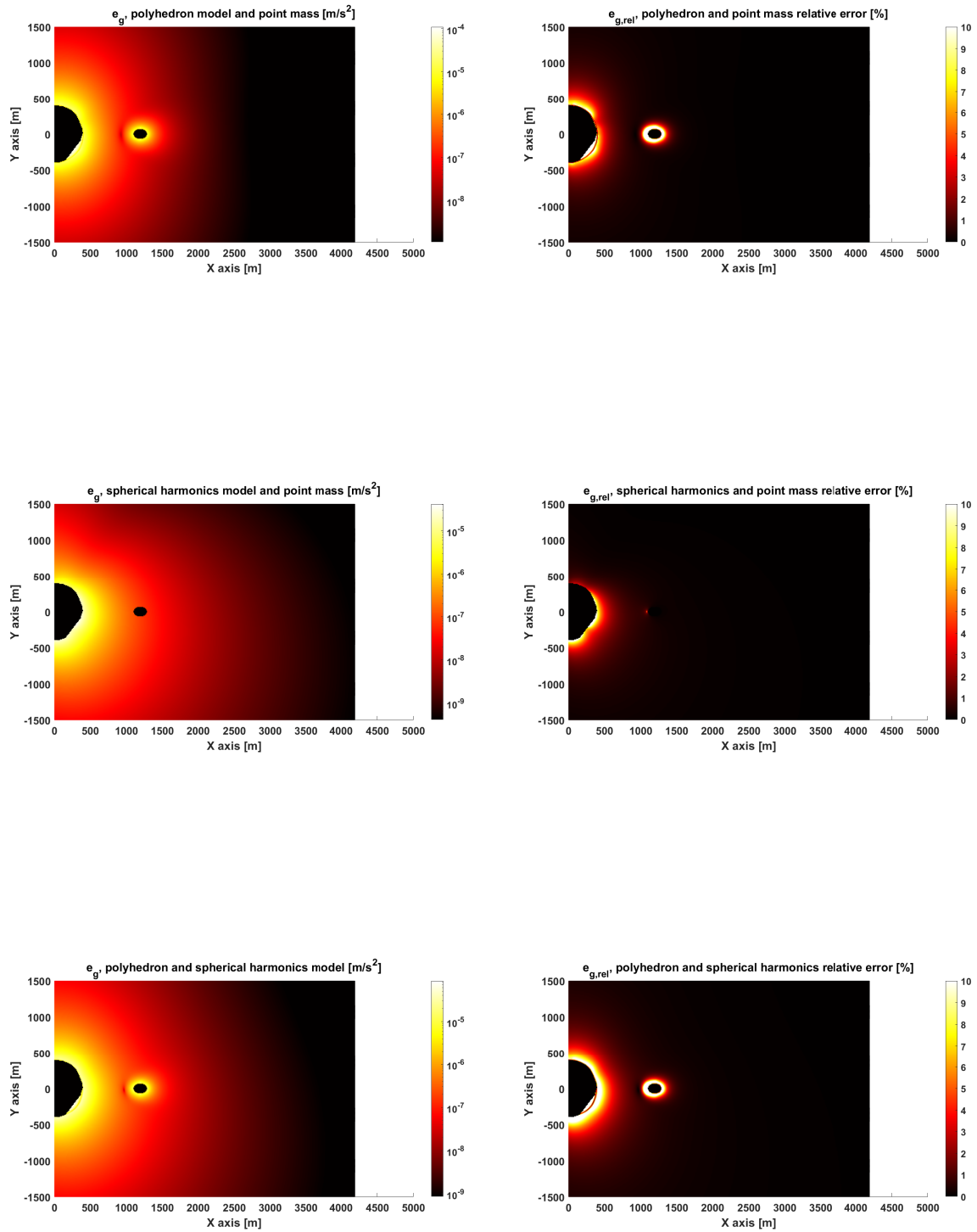
Figure 4.9: Magnitude of error and relative error of different gravity models. Coordinate system is centered in the CoM of the primary asteroid. Note that a logarithmic scale is used for the absolute error figures.

model 2.28×10^{-8}. These are the worst-case errors that the spacecraft will encounter, because the farther it moves away from the bodies, the lower this error will be. The relative error as defined in Eq. (4.10) starts around 0.3% and quickly goes down to below 0.01% as the distance to the asteroids increases. The difference between the polyhedron model, the spherical harmonics model and the point mass model are all very small at the distances relevant to the HAP.

What is the effect of this deviation on the spacecraft?   To estimate what the effect of deviations of this order of magnitude are on the spacecraft flight trajectory, a simple integration is performed. The polyhedron gravity model is compared to the point mass gravity model. The scenario is as follows: the spacecraft starts at the point $(5000, 0, 0)$ where the origin is fixed at the surface of the secondary asteroid. The orientation of the bodies is assumed to be as in Fig. 4.3. The initial velocity is 5cm/s in the direction of the secondary asteroid. One trajectory uses the polyhedron gravity field, the other the point mass gravity field. Once one of the two trajectories reaches 300 m altitude, the simulation is stopped. The result is that after about 52000 seconds, both trajectories reach 300 m altitude, with only 0.24 m difference between them.

Conclusion Gravity Models   The deviation of the point mass gravity model from more precise and realistic models is very small in the region of the HAP. Because the environment is still rather uncertain at this time, it is not possible to know whether the spherical harmonics or the polyhedron gravity model is closer to reality. The benefit of using a more precise gravity model in the simulator is to simulate a non-idealized environment. If the navigation filter uses an assumption for the gravity field, e.g. a point mass model, there will always be a mismatch between the estimated gravity and the real gravity. The navigation filter must be robust to this, as in reality it will face a similar situation.

The current gravity field implementation used in the LAP simulator uses very high resolution polyhedron models of Bennu and Itokawa, rescaled to match the mass and MoI properties of Didymos and Dimorphos. This solution will also be used in the HAP simulator, as it is already existing and tested. It serves the purpose of presenting a realistic gravity field to the spacecraft, for as far as this is possible with the current knowledge of Didymos.

4.1.5. Research Questions
The research questions relevant to this chapter are RQs 2 and 3.

> **Research Question 2**
>
> What are the requirements for a simulator that can be used to develop the navigation system?

> **Research Question 3**
>
> What prior knowledge about the asteroid environment is required to estimate the spacecraft state with a given sensor suite?

RQ 2 has been answered for the simulator part. The key findings of this chapter in relation to the second research question are that the third-body perturbations can be neglected, and that either the spherical harmonics or polyhedron gravity models can be applied to simulate the gravity field around the asteroids. The polyhedron gravity model is now implemented in the simulator. The solar radiation pressure effect was found to be non-negligible and is included in the environment of the simulator.

RQ 3 is partially answered in the sense that the environment is now programmed into a simulator, making this analysis possible in the first place.

4.2. Conclusions preliminary work
This literature study report has presented the motivations and framework of the research in this thesis. This has lead to the following research objective:

Research Objective

Investigate how an autonomous spacecraft can determine its absolute position and velocity in proximity of a binary asteroid by using vision-based navigation.

The research questions that need to be answered to fulfil the research objective are:

Research Question 1

What is the state of the art of navigation around asteroids?

Research Question 2

What are the requirements for a simulator that can be used to develop the navigation system?

Research Question 3

What prior knowledge about the asteroid environment is required to estimate the spacecraft state with a given sensor suite?

Research Question 4

What are the performance requirements for the navigation system, and how do these requirements change during the iterative design process?

Research Question 5

Which navigation systems can meet the performance requirements?

Research Question 6

What are the key sensitivities of the developed navigation system?

RQ 1 has been completely answered in this literature study report by looking at both the past asteroid and comet missions from the major space agencies as well as the research work that has been published by other researchers. Past missions relied heavily on radiometric tracking and Earth-in-the-loop vision based navigation. Autonomous systems were already foreseen back then, such as on the Hayabusa-1 mission. These were were however never tried due to hardware failures. Recent studies have been focusing increasing autonomy and making use of (vision-based) sensor information on-board. This has shown great potential in increased safety, compressed mission timelines and reduction of mission costs.

RQ 2 has been partially answered, as only the simulation environment was covered in this preliminary work. An analysis on how the simulator environment should look and what relevant forces should be included in the environment model is carried out. The conclusion here is that third-body perturbations can be neglected, whereas the solar radiation pressure cannot be neglected. A polyhedron gravity model and a spherical harmonics gravity model both seem to give similar results, and either can be chosen to realistically simulate the gravity field of the asteroids. The polyhedron model is chosen because an already existing implementation exists, which is now part of the simulator for the navigation filter.

RQ 3 is partially answered, in the sense that the simulator environment now exists that makes this analysis possible.

RQ 4 is partially answered. The default requirements are set by the study and are presented in Section 3.4. The 3σ position knowledge error for any axis shall be below 10% of the distance to the target

asteroid. The initial distance to the asteroid in the I-frame shall be in the range [5,8] $\pm$ 0.05 km. The initial velocity in the I-frame is in the range [7,14] $\pm$ 10% cm/s. The final altitude above the outward facing pole of the asteroid during the high altitude phase shall be such that the low altitude navigation system can take over. There is some flexibility in this last requirement, because it is unknown at this stage what altitude can be reached with the high altitude navigation system. The minimum distance that can be reached is 300 m above the surface of the secondary asteroid, because at this altitude the asteroid will fill the complete FOV of the camera. Centroid-based navigation will become impossible once this threshold altitude is crossed.

RQs 5 and 6 remain unanswered and will be answered in the next phase of the research.

Part III

Additional Results

Additional Results

This chapter presents additional results and findings that are not included in the scientific paper and preliminary work chapters. First, additional results for the pointing mode analysis covered in Section 2.4 of the paper are presented. Then, an experimental augmented version of the EKF is introduced and compared to the version developed in the paper.

5.1. Initial filter setup and tuning

For completeness, this section shows the primary pointing mode that is mentioned in Section 2.4 of the paper. The option to first point primary and then point secondary could be motivated by the apparent size of the primary in the image, making it a viable option at very far distances when the secondary is hard to resolve in the image. At the altitudes considered in the reference trajectory, both asteroids are well visible in the images. The results for pointing primary are compared to pointing secondary in Figs. 5.1, 5.2, and 5.3.

In primary pointing mode, the navigation system points towards the primary until the number of asteroids detected in the image goes to one, after which the spacecraft reorients itself to point at the secondary. The reorientation maneuver is implemented as an instantaneous change in the attitude of the spacecraft. The sudden increase in the 3σ bounds that is observed around 3000 seconds when pointing secondary, and around 5000 seconds when pointing primary, indicate the switching point where the number of asteroids in the frame decreases to 1. The graphs indicate that the switching point is earlier for pointing secondary than for pointing primary. This is mainly caused by the size of the primary asteroid. If the pointing is at the secondary, the primary will quickly touch the edges of the frame, disqualifying the measurement associated with the primary. If the spacecraft points at the primary, the chance that the secondary is out of the frame is smaller because it is a much smaller asteroid.

There are also substantial differences in the estimation error in the X-direction. This is the result of the ellipsoid shape model mismatch between the 3D model for the primary in PANGU and the ellipsoid shape model in the measurements model. To get a complete understanding of the mismatch between the ellipsoid shape model and the 3D model for the primary, many simulations from different angles must be done. However, for this particular trajectory the ellipsoid shape model matches the secondary better than the primary. After the switching point at about 5000 seconds, the spacecraft reorients itself and points at the secondary asteroid, switching out the primary ellipsoid model for the secondary ellipsoid model. The difference between the two simulations becomes negligible because they are effectively the same from that point onwards.

5.2. Laser range finder model mismatch estimation

The LRF measurements model is a source of errors in the state estimation process due to the mismatch between the ellipsoid shape model and the true asteroid shape model. An attempt is made to reduce this error by estimating the mismatch as a parameter in the filter. The EKF converges without the LRF as well, as long as both asteroids are in the image. This is shown in Section 2.4 of the paper. The underlying idea for this model mismatch parameter estimation is that the combination of two visible asteroids gives additional ranging information, which can be used to augment the LRF measurement.
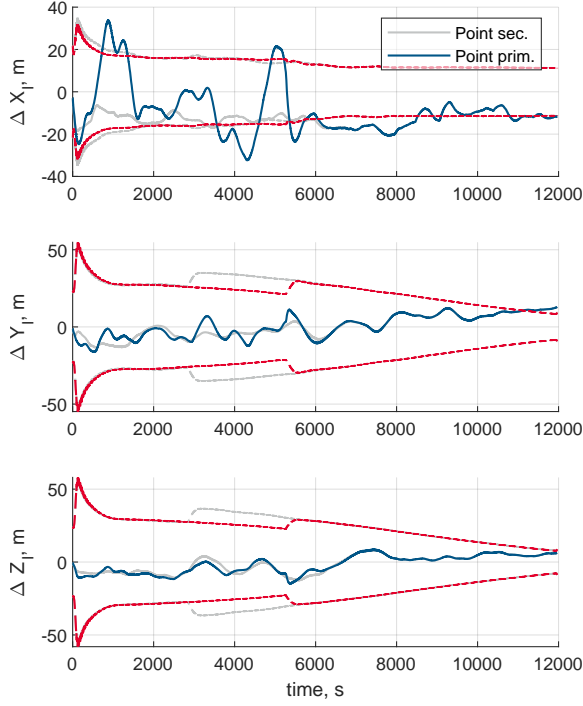
Figure 5.1: I-frame position estimation errors, including error 3σ bounds. Pointing secondary compared to pointing primary.
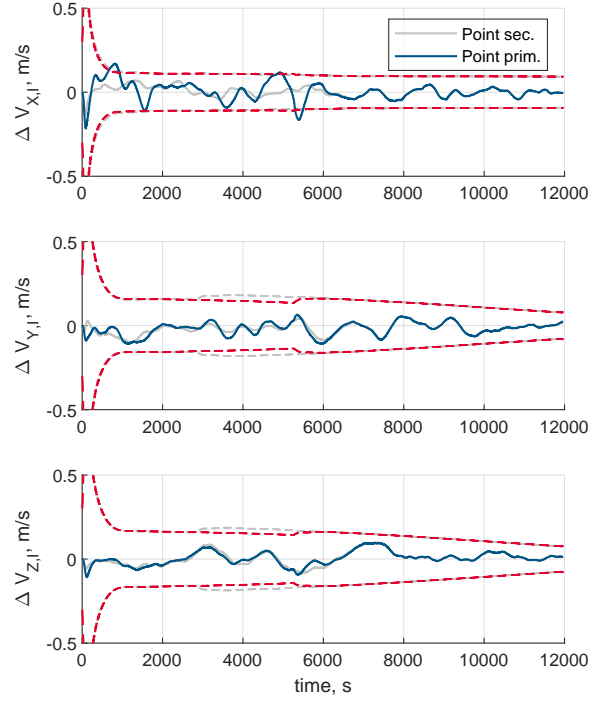

Figure 5.2: I-frame velocity estimation errors, including error 3σ bounds. Pointing secondary compared to pointing primary.

5.2.1. Mismatch parameter characteristics

The mismatch depends on the specific point of contact of the LRF. The mismatch is calculated for every simulation in the initial position sensitivity study in Section 2.5 of the paper to better understand its behavior. This yields one different value for the mismatch at every timestep, each associated with one run. Of these mismatch values, the mean and 3σ bounds are shown for every time step in Fig. 5.5. The convergence of the 3σ bounds is explained by the trajectories becoming more and more similar as time progresses, because the target position is the same for each run. If the final position would be different, this graph would have looked completely different. Because of this uncertainty, no dynamic is assigned to the mismatch parameter b_{LRF}. The white process noise associated with the LRF mismatch parameter, $\eta_{\text{LRF,mm}}$ is a tuning parameter in the EKF.

5.2.2. Extended Kalman filter changes

The state vector is adapted to include the mismatch parameter b_{LRF}:

$$\boldsymbol{x} = \begin{pmatrix} \boldsymbol{r}_I^{IB} & \dot{\boldsymbol{r}}_I^{IB} & \boldsymbol{b}_{\text{acc},B} & b_{\text{LRF}} \end{pmatrix}^T \tag{5.1}$$

and the propagation equation is updated:

$$\dot{\boldsymbol{x}} = f(\boldsymbol{x}, \boldsymbol{u}) + \boldsymbol{G}\boldsymbol{\omega} = \begin{pmatrix} \dot{\boldsymbol{r}}_I^{IB} \\ \ddot{\boldsymbol{r}}_I^{IB} \\ \dot{\boldsymbol{b}}_{\text{acc},B} \\ \dot{b}_{\text{LRF}} \end{pmatrix} + \boldsymbol{G} \begin{pmatrix} \boldsymbol{\eta}_{\text{acc}} \\ \boldsymbol{\eta}_{\text{acc,bias}} \\ \eta_{\text{lrf,mm}} \end{pmatrix} =$$

$$\begin{pmatrix} \dot{\boldsymbol{r}}_I^{IB} \\ -\mu_p \dfrac{\boldsymbol{r}_I^{IB} - \boldsymbol{r}_I^{IP}}{|\boldsymbol{r}_I^{IB} - \boldsymbol{r}_I^{IP}|^3} - \mu_s \dfrac{\boldsymbol{r}_I^{IB} - \boldsymbol{r}_I^{IS}}{|\boldsymbol{r}_I^{IB} - \boldsymbol{r}_I^{IS}|^3} + \boldsymbol{R}_{IB}(\boldsymbol{a}_{\text{meas},B} - \boldsymbol{b}_{\text{acc},B}) \\ \boldsymbol{0} \\ 0 \end{pmatrix} + \begin{bmatrix} \boldsymbol{0}_{3x3} & \boldsymbol{0}_{3x3} & 0 \\ -\boldsymbol{R}_{IB} & \boldsymbol{0}_{3x3} & 0 \\ \boldsymbol{0}_{3x3} & \boldsymbol{I}_{3x3} & 0 \\ \boldsymbol{0}_{3x3} & \boldsymbol{0}_{3x3} & 1 \end{bmatrix} \begin{pmatrix} \boldsymbol{\eta}_{\text{acc}} \\ \boldsymbol{\eta}_{\text{acc,bias}} \\ \eta_{\text{LRF,mm}} \end{pmatrix} \tag{5.2}$$
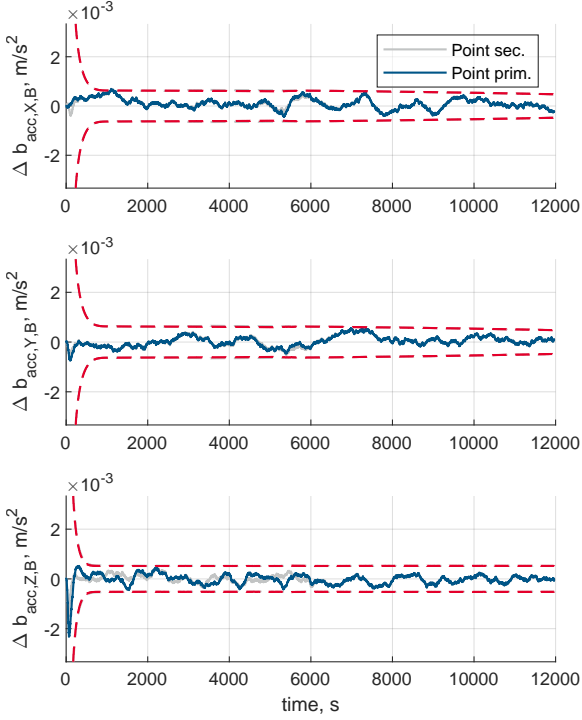
Figure 5.3: B-frame accelerometer bias estimation errors, including error 3σ bounds. Pointing secondary compared to pointing primary.
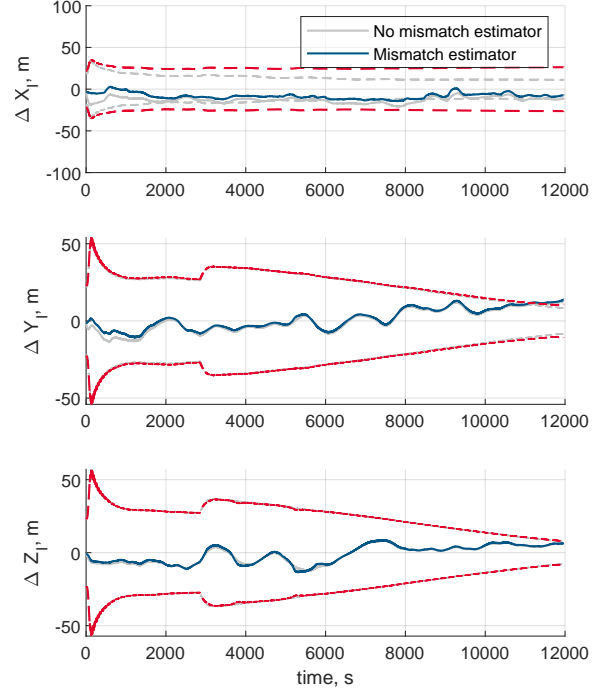

Figure 5.4: I-frame position estimation errors, including error 3σ bounds. EKF without LRF mismatch estimation compared to the EKF with LRF mismatch estimation. Pointing secondary.

The measurement model for the LRF is updated to include both the ellipsoid model and the mismatch parameter:

$$z = h(\boldsymbol{x}, \boldsymbol{u}) = r_{\mathsf{LRF}} = \left\| \boldsymbol{r}_P^{PL} - \boldsymbol{r}_P^{PB} \right\| + b_{\mathsf{LRF}} \tag{5.3}$$

and the new Jacobian becomes:

$$\boldsymbol{H}_x = \frac{\partial h(\boldsymbol{x}, \boldsymbol{u})}{\partial \boldsymbol{x}} = \begin{bmatrix} \dfrac{\partial h(\boldsymbol{x}, \boldsymbol{u})}{\partial \boldsymbol{r}_I^{IB}} & \boldsymbol{0}_{1x3} & \boldsymbol{0}_{1x3} & 1 \end{bmatrix} \tag{5.4}$$

5.2.3. Tuning and results

There are now two tuning parameters associated with the LRF measurement: the σ_{LRF} parameter in the $\boldsymbol{R}$ matrix of the measurement update, and the $\sigma_{\mathsf{LRF,mm}}$ parameter in the $\boldsymbol{Q}$ matrix of the propagation step. The value of $\sigma_{\mathsf{LRF,mm}}$ determines the convergence of the 3σ bounds of b_{LRF}. Because there is no prior knowledge about the behavior of b_{LRF}, it is desired that its uncertainty remains constant. By tuning it is found that with $\sigma_{\mathsf{LRF,mm}} = 0.15$ m/s, the uncertainty in b_{LRF} remains constant. For σ_{LRF}, a value of 5 m is found to give satisfactory results.

This updated version of the EKF is tested on the default trajectory. The result is compared with the original version of the EKF in Fig. 5.4. The two EKFs perform roughly the same in the Y- and Z-direction where the camera is responsible for the majority of the state estimation. The real difference between the two EKFs is shown in the X-direction where the LRF measurement dominates the state estimation. There is a marginal improvement in the state estimation performance, although the EKF with LRF model mismatch estimator is not capable of removing the LRF model mismatch. During the first 3000 seconds of the flight both asteroids are visible in the camera images and there is extra information in the measurements to perform the estimation of b_{LRF}. Still, the EKF does not succeed in doing this, indicating that this approach is not successful.
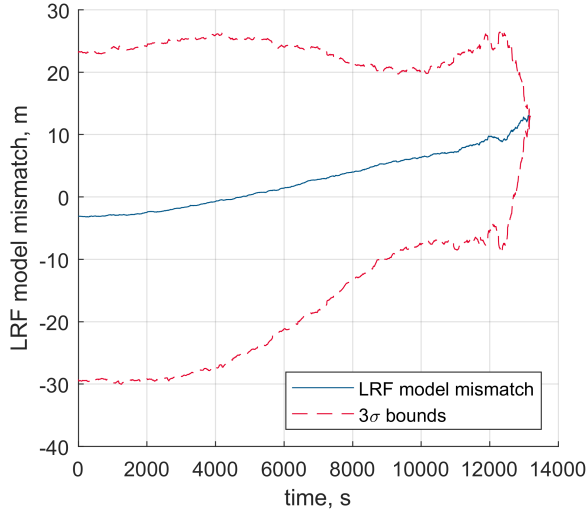
Figure 5.5: LRF model mismatch for the simulations in the initial position sensitivity study in Section 2.5 of the paper. The mean value of the mismatch and the 3σ bounds are shown for all simulations that reach below 600 m altitude. Only pointing secondary is considered.
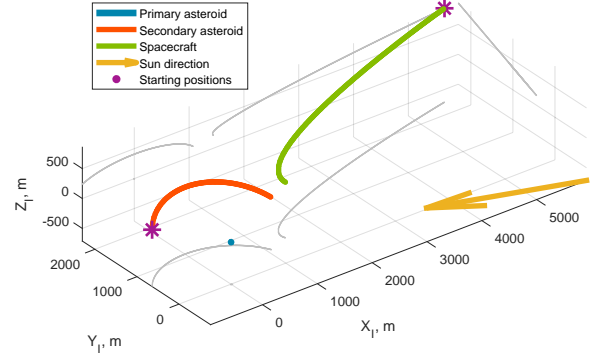

Figure 5.6: Trajectory of the primary, secondary, and the spacecraft in the reference landing scenario. Note that the illumination conditions are favorable due to the low sun phase angles.

As a final test, the performance of both EKFs is evaluated when pointing at the primary asteroid first, followed by the reorientation maneuver once the visibility of one of the asteroids is lost. The results are shown in Fig. 5.7. The EKF with LRF model mismatch estimator now performs worse than the default EKF without it, once again confirming that this approach is not successful.

5.2.4. Conclusion model mismatch estimation

The approach described in this section does not yield satisfactory results. It is most likely not possible to accurately determine the LRF model mismatch b_{LRF} with the available measurements. If the default EKF is used in the midpoint pointing mode, the state estimation is performed without the LRF until the switching point is reached where the secondary pointing mode is enabled. Before the switching point around 9000 s, the state estimation uncertainty in the line of sight direction (X-direction, Fig. 5.6) is rather large as can be seen in Fig. 5.8. The uncertainty in the X-direction is in the order of hundreds of meters. It is not possible to estimate b_{LRF}, which is in the order of tens of meters (Fig. 5.5), if the uncertainty in the X-direction is in the order of hundreds of meters.

Concluding the work presented in this section, it is clear that when only two optical measurements of the asteroids are used, the uncertainty in the line of sight direction is much larger than the errors in the LRF ellipsoid model mismatch. Therefore, the method to estimate the mismatch parameter in this section is not successful.
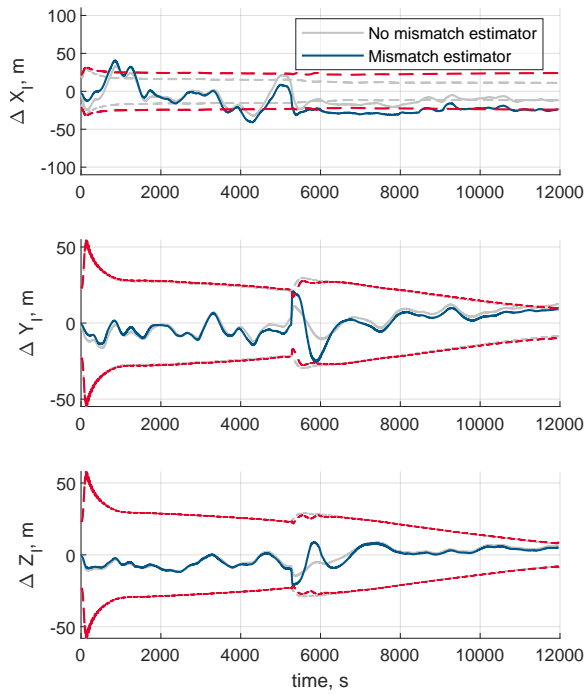
Figure 5.7: I-frame position estimation errors, including error 3σ bounds. EKF without LRF mismatch estimation compared to the EKF with LRF mismatch estimation. Pointing primary.
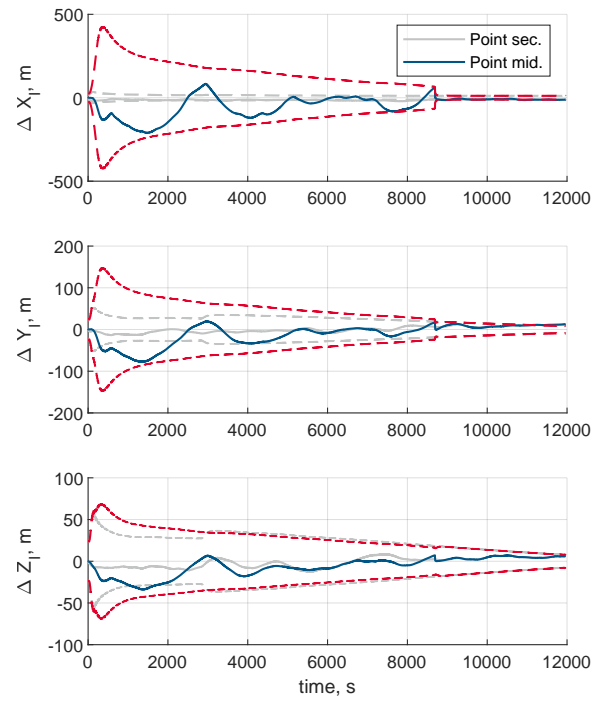
Figure 5.8: I-frame position estimation errors, including error 3σ bounds. Pointing secondary compared to pointing at the midpoint. Default EKF without LRF model mismatch estimation.

6

Verification and Validation

All experiments in this work are carried out in a simulated environment. It is crucial to understand the limitations and assumptions that have been made to construct the simulated environment, to put the results in context. This chapter first summarizes the steps that have been taken to verify the correct implementation of the components in the simulator in Section 6.1. Finally, the validation steps that have been taken to validate the results, as well as those validation efforts that still need to be done to validate the navigation filter, are given in Section 6.2.

6.1. Verification

6.1.1. SPICE kernel

The SPICE kernel is implemented in the simulator as a block that returns the asteroid and Sun position, velocity, and orientation for a given moment in time in the Modified Julian Date format. By selecting a long enough simulation time, the rotation period of the primary and secondary, as well as the orbit radius of the secondary can be calculated. These are all verified to be consistent with the values in [59].

The spin pole of the primary is parallel to the secondary orbital spin pole. This is verified by calculating a vector normal to the orbital plane of the secondary around the primary. This orbital plane is defined by three points along the orbit of the secondary. Each point is taken one third of an orbital period after the other. The rotation axis of the primary is found to be parallel to the vector normal to the orbital plane of the secondary around the primary, thus the rotation of the primary is implemented correctly.

The secondary asteroid is verified to complete one full revolution around the primary in the period stated in [59]. Its spin pole is also confirmed to be parallel to that of the primary.

6.1.2. Solar radiation pressure

A manual check is done to verify that the solar radiation pressure force points in the direction away from the Sun. First the unit vector from the spacecraft to the Sun is calculated. Then the normalized solar radiation force is calculated. The dot product of these two vectors is found to be -1, proving that the solar radiation pressure indeed acts in the opposite direction of where the light from the Sun is coming from.

6.1.3. Gravity fields

During the set-up of the scripts that calculate the polyhedron gravity model lookup tables, intermediate results have been plotted time and time again to verify that the solutions were as expected. One key verification test that is done is to make sure that the polyhedron gravity model approximates the point mass gravity model at far distances. The result of this test is found in Section 4.1. The polyhedron gravity model indeed approximates the point mass gravity model at distances beyond a couple hundred meters distance from the asteroid surface.

The polyhedron gravity model is calculated for a mesh grid of points that encapsulates the region that the spacecraft could possibly reach within the simulations. Linear interpolation is used to calculate the gravity at every point in between the grid points. The polyhedron gravity model is not defined within the 3D polyhedron model itself, and a function is built into the gravity model lookup-table calculation script to check for every grid point whether it is inside the 3D polyhedron model.

To verify that the orientation of the polyhedron gravity model is correct, the 3D model that is used to construct the polyhedron model is imported into MATLAB with the patched polygon drawing function. Then, all points that are found to be within the hull of the 3D polyhedron model during the calculation of the gravity lookup-tables are visualized in a point cloud graph and compared to the 3D model. The point cloud is found to perfectly match the 3D model, verifying that the orientation of the 3D model as used in the polyhedron gravity model is the same as what is used in the 3D model itself. What is used in the 3D model itself is also used in PANGU, thus this check makes sure that the primary and secondary asteroid gravity models are aligned with the visuals in PANGU.

6.1.4. PANGU

To test the setup of the virtual scene in PANGU, a test is designed in which the secondary asteroid casts a shadow onto the primary asteroid. The goal of this test is to verify the implementation of the 3D models in PANGU, and whether the shadows that PANGU produces are correct. The result is shown in Fig. 6.1. The shadows look as expected, verifying this aspect of PANGU.

There are many more aspects to a camera simulator such as PANGU that are not covered here. The lens model, inclusion of effects such as chromatic aberration, vignetting, and radiation noise are all examples of camera specific properties that are not tested here. Besides this, the light metering settings of the camera are not considered. All these details must be carefully investigated in future work to make sure that the PANGU environment is indeed representative for the real asteroid environment. For the purposes of this research, this level of verification is sufficient to design the navigation system and to prove the working principle of the navigation concept.
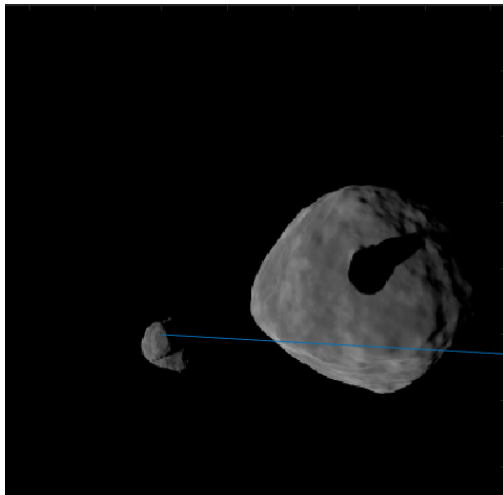

Figure 6.1: Image taken during the PANGU test, showing the shadow cast by the secondary onto the primary.
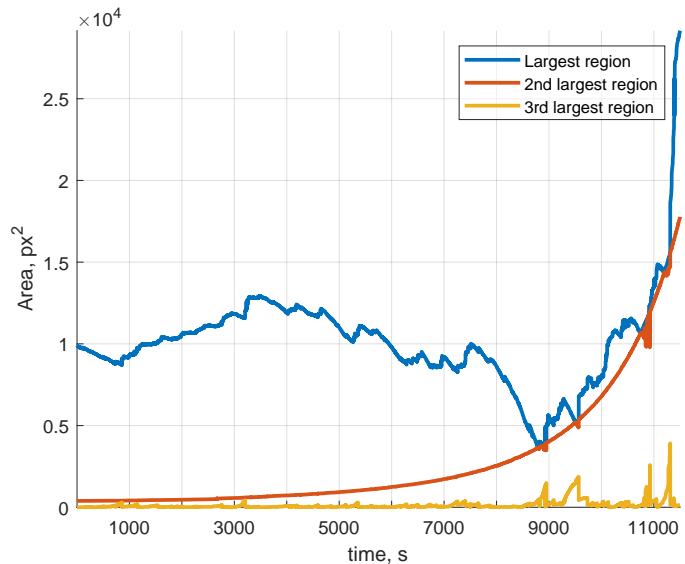
Figure 6.2: Size in px^2 of the three largest regions detected at every timestep of the reference trajectory simulation.

6.1.5. Image processing

The image processing algorithm extracts estimates for the center of figure locations of the asteroids. Several tests are done to verify that the algorithm indeed performs as intended. The image processing algorithm is given in Algorithm 1.

Classification

The classification refers to the assignment of the label 'primary' and 'secondary' to the detected regions of pixels, step 5 of Algorithm 1. A test is setup in which only one pixel is white. This white pixel is placed at the middle point between the expected center of figure locations of the two asteroids. The pixel is then moved one pixel in the direction of the primary or the secondary, which should yield two different classification results. This is indeed the observed behavior.

Algorithm 1 Image processing

1: Convert the image to grayscale.
2: Binarize the image. Every grayscale pixel is converted to either 1 (white) or 0 (black). The threshold that determines to which group a pixel belongs is set using Otsu's method [61].
3: Fill holes in the image. A hole is defined as a set of background pixels that cannot be reached by filling in the background from the edge of the image.
4: Extract the area, centroid location, and bounding box of each 8-connected object in the binary image.
5: Assign the label 'primary' or 'secondary' to each detected object based on the minimum distance between the object centroid and the predicted projection of the primary and secondary center of mass.
6: Sort the objects within the primary and secondary lists by their area. Select the largest two objects from each list.
7: Apply the Sun phase angle correction ε_cob to the largest object corresponding to the primary asteroid.
8: Discard the objects if their bounding boxes overlap each other. Stop simulation.
9: Discard objects if their bounding box touches the edges of the frame.
10: Discard all measurements if the distance between two consecutive $\hat{p}_\text{cof}$ is beyond a threshold value.

Another test is done by placing a region of two pixels close to the expected center of figure location of the primary, followed by another region of only one pixel in the vicinity. The algorithm then assigns the label 'primary' to both of these regions, and selects the centroid of the largest region as the center of brightness of the primary. This is the expected behavior, as only the largest region that is detected for each asteroid is considered as a possible measurement.

The assumption that the largest detected region is representative for the whole asteroid is only valid if this largest region is much larger than any other smaller regions. These smaller regions can be detected in the shadow regions around the edges of the asteroid at higher Sun phase angles. For the reference trajectory, the size of the three largest regions during the whole landing trajectory are shown in Fig. 6.2. The third largest region is indeed always much smaller than the other regions, thus the approach is justified. Interesting to note is that the orange line, corresponding to the 2nd largest region, grows as the spacecraft gets closer to the secondary. The large jump in the area of the largest region towards the end of the simulation is explained by the primary asteroid returning back in the frame.

Sun phase angle correction factor
The Sun phase angle correction is at step 7 of Algorithm 1. To verify that this correction is indeed helpful and brings p_cob closer to p_cof, the mean Euclidean pixel distance between the true center of figure p_cof and the estimated center of figure $\hat{p}_\text{cof}$ is compared:

$$\text{Mean Euclidean pixel distance} = \frac{\sum\limits_{i=1}^{n} \|p_\text{cof} - \hat{p}_\text{cof}\|_i}{n} \tag{6.1}$$

Now $\hat{p}_\text{cof}$ is either p_cob, or the version corrected with ε_cob. This analysis is carried out for the reference trajectory. The mean Euclidean pixel distance for the primary asteroid reduces from 3.24 px to 1.75 px when the correction factor is applied. For the secondary asteroid however, the mean Euclidean pixel distance increases from 2.88 px to 3.30 px when the factor is applied. This shows that the correction factor is indeed not suitable for non-spherical shapes, and therefore it is chosen that the correction factor is only applied to the primary asteroid.

Discarding of measurements
Steps 8, 9, and 10 describe events that lead to the measurement being discarded. These steps rely on simple functions that are tested with an edge case to verify their working. For example, the overlap of bounding boxes can be easily simulated by creating two overlapping bounding boxes and giving these as input for the function that checks whether they overlap.

6.1.6. Laser range finder
The LRF measurement model uses the ellipsoid-line intersection to calculate the expected LRF measurements. A test is set up in the simulator to check that the implementation is correct. For this test,

the spacecraft is placed at a fixed distance of 500 m from the secondary asteroid center of mass. The spacecraft points at the center of mass of the secondary and the LRF measures the distance to the surface. The secondary then completes one full revolution around its center of mass. The experiment setup is visualized in Fig. 6.3. The LRF measurements are then compared with the expected measurements from the ellipsoid measurement model. An image taken by the navigation camera during this experiment is shown in Fig. 6.4. By subtracting the LRF measurement from the altitude, the distance from the center of mass to the surface of the asteroid is obtained. With a full revolution of the asteroid, a slice of the asteroid 3D model is obtained. The same can be done for the ellipsoid model. Two tests are done, each test represents a different axis of rotation for the asteroid. These results are shown in the form of a polar plot in Fig. 6.5. The ellipsoid model captures the overall shape of the asteroid, and its orientation is also correct. This test verifies that the LRF measurement model is implemented correctly.

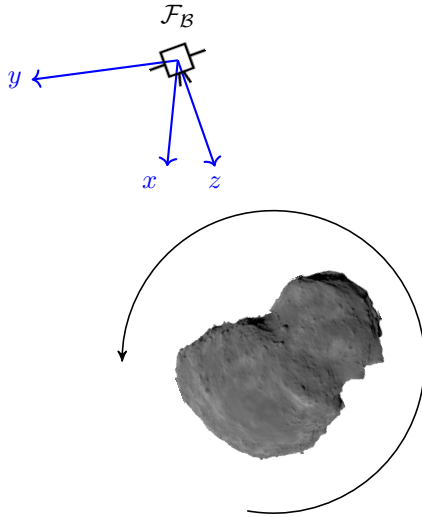**Figure 6.3:** Sketch of the LRF verification experiment. The secondary asteroid completes one full rotation around one axis.
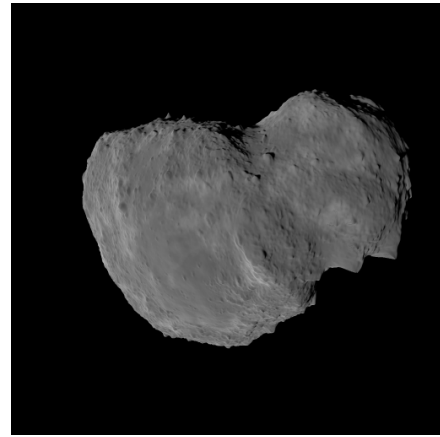

Figure 6.4: Image taken during the laser range finder test. The spacecraft is 500 m away from the center of mass of the secondary asteroid.
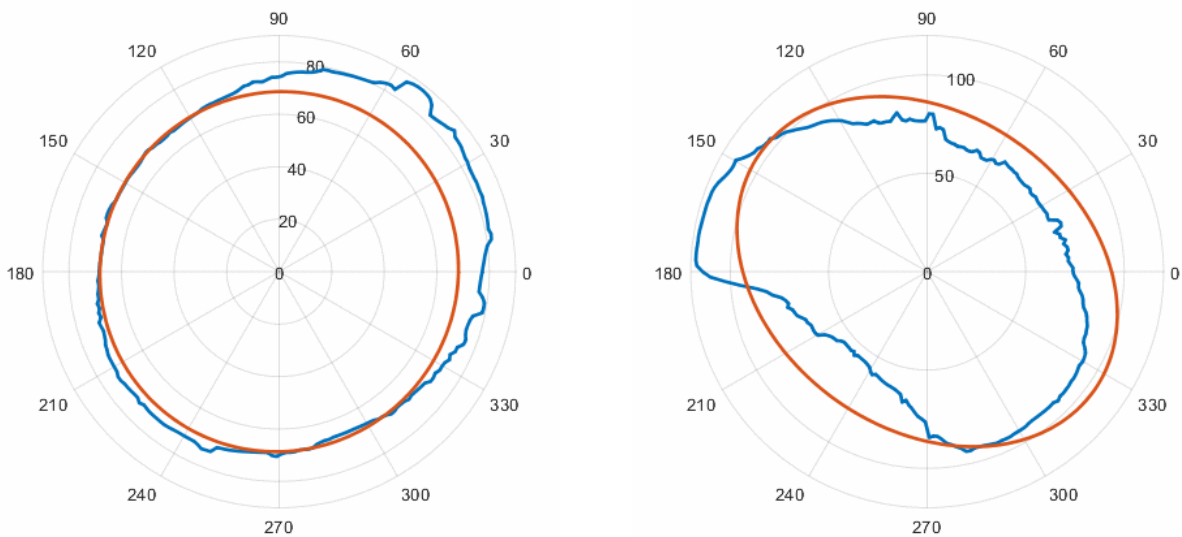

Figure 6.5: Polar plots comparing the LRF measurement from PANGU (blue) and the ellipsoid measurements model (orange). Radial distance in m.

6.1.7. Extended Kalman filter

The EKF implementation is verified in multiple ways. First, the propagation step is verified. Then, the consistency of the filter is verified through use of ideal measurements with known noise characteristics.

Propagation step verification

The propagation step is verified by tweaking the simulator to represent the dynamics as they are implemented in the EKF. This is done by replacing the polyhedron gravity model with a point mass gravity model. Then, the noise is removed from the input by disabling the accelerometer noise and velocity random walk. The EKF state is initialized without error. Over the four hour trajectory, position errors in the order of 0.1 m are accumulated, along with velocity errors of around 0.02 mm/s. This difference is explained by the different numerical integration schemes in the dynamics block and in the EKF. The EKF uses the forward Euler integration scheme, whereas the simulator automatically selects a numerical integration scheme using the automatic solver selection option in Simulink. For the accelerometer velocity random walk there is no difference between the simulator and the EKF because the noise that drives the process is turned off. This test verifies the correct implementation of the dynamics in the propagation step.

Consistency verification

The consistency verification is briefly mentioned in Section 2.4 of the paper. The consistency requirements are stated once more: the estimation errors (i) are zero-mean, and (ii) have a covariance matrix smaller or equal to the one calculated by the filter [62].

Two verification simulations are done with ideal measurements. These simulations are identical, with one exception: in the second simulation the primary asteroid measurement is ignored. This means that even if the primary is visible in the camera image, no measurement is used in the EKF. The error signals of the two simulations are tested against the consistency requirements for both simulations. For the position estimation errors, the mean of all individual components stays within $\pm$ 2 m. For the velocity estimation errors, the mean stays within $\pm$ 0.02 m/s. For the accelerometer velocity random walk estimation errors, the mean stays within $\pm$ 3e-5 m/s^2. It is expected that for more simulation runs, this mean tends to zero.

Now the covariance requirement is tested. If the estimation errors follow a Gaussian distribution with zero mean and a variance of at the maximum that calculated by the EKF, the chance that for example the X-position estimation error lies inside its 3σ bounds at a given time step is 0.9973. For every filter state, the percentage of data points that lies within the EKF's calculated uncertainty bounds is shown in Table 6.1. The expected percentages based on the theory are 68%, 95%, and 99.7%, for 1σ, 2σ, and 3σ, respectively.

Both the error means and covariances indicate that the EKF is close to consistent. However, the data of only two simulation runs is very limited and therefore it is not possible to draw a definite conclusion about the filter consistency based on the data presented here. If the filter is indeed inconsistent, an observability analysis such as [63] could be applied to this problem to determine the cause of the inconsistency and potentially mitigate it.

6.2. Validation plan

Validation is required to ensure that the results in this work match the results in reality. Because of the reality gap between the simulator and reality, a working solution in the simulator does not necessarily perform the same in a real space environment with real hardware. No validation testing is done with the setup as described in this work. Therefore, this section provides a validation plan that needs to be carried out in future work to validate the results. First, an overview of several assumptions that have been made in the simulation model is given. Then a plan to validate the image processing is given, followed by a comparison of the results in this paper with independently published work in literature. Finally, a plan to validate the full system is given.

6.2.1. Assumptions

To build the simulator, assumptions are made which cause a difference between the results obtained in the simulator and reality. The impact of an assumption must be assessed to understand the impact they have on the results.

Table 6.1: Error signal characteristics for two simulations with ideal measurements that only include white noise. There are 95721 data points in each simulation.

	Primary + secondary			Secondary only		
	% within 1σ	% within 2σ	% within 3σ	% within 1σ	% within 2σ	% within 3σ
X_I	67.4063	94.8820	99.5205	70.7629	94.0744	99.7911
Y_I	71.2560	96.8168	99.9582	55.5030	87.1000	98.0715
Z_I	60.9177	93.6754	96.9098	59.6118	89.8340	99.3680
$V_{X,\mathrm{I}}$	60.2229	92.8709	100.000	65.6972	92.7257	98.4152
$V_{Y,\mathrm{I}}$	64.9325	94.2865	99.8600	55.6900	87.7707	97.5763
$V_{Z,\mathrm{I}}$	62.7689	93.3108	99.9582	64.6828	93.8707	99.8297
$b_{\mathrm{acc},X,\mathrm{B}}$	65.0098	89.2803	98.9219	61.8046	89.7953	98.2836
$b_{\mathrm{acc},Y,\mathrm{B}}$	61.6866	95.3751	100.000	64.6504	96.2662	100.000
$b_{\mathrm{acc},Z,\mathrm{B}}$	64.3130	97.0414	99.2008	68.2097	94.4035	99.2154
Column mean	64.2793	94.1710	99.3699	62.9569	91.7601	98.9501

In Section 4.1, an analysis of the perturbing forces on the spacecraft in the binary asteroid environment is presented. This analysis is crucial to understand the impact of the assumptions that are made, such as the neglecting of third body gravity effects.

A cannonball model is used to model the SRP. The cannonball model considers the spacecraft to be a sphere and as a result the attitude of the spacecraft is not part of the SRP calculation. Every part of the (non-variable) surface area has the same reflective properties. An analysis on the impact of assuming a cannonball SRP model on the spacecraft dynamics in the vicinity of a binary asteroid environment is given in [64]. This work shows that the differences between the cannonball model and more elaborate SRP models can be as large as 500%. These are extreme cases where the combination of model parameters is such that the differences between the models are highlighted, but it does show the significance of the error that could be introduced with this simplification. The differences in SRP are mainly relevant for the trajectory of the spacecraft. The dynamics in the EKF do not depend on a model for the SRP and instead directly measure the acceleration of the spacecraft.

In the current implementation, sensor misalignments are not considered. Through calibration efforts, an attempt is made to reduce the impact of sensor misalignments. However, the remaining (small) misalignment must still be accounted for, and are often not constant throughout the duration of the mission. Therefore, methods to estimate the misalignments online are implemented in reality.

The pointing at the desired asteroid, or at the midpoint in between them, is enforced in the simulator by exploiting knowledge of the true state. In reality, this is not possible as the true state is unknown. Instead, the attitude from the attitude determination system with its star trackers and rate gyros should be used as an input to the pointing algorithm. This attitude knowledge can be combined with the line of sight of the asteroid obtained from the navigation camera images, to create an online pointing algorithm. Assuming perfect pointing is convenient for the purpose of navigation filter development, but the system should always be tested in combination with an online pointing algorithm to make sure that the interaction between the two systems is stable.

All these points are reasons to believe the results in this work are not completely representative for the performance of the navigation system in a real environment. The following validation plan is made to mitigate the uncertainty in the results.

6.2.2. Pseudo-validation with literature

A comparison with other results from literature is not a true form of validation. Such a comparison with results in literature is therefore referred to here as pseudo-validation. A one-to-one comparison with results in literature is difficult to make because everyone uses a different set-up. Part of this work is however comparable to a study on vision-based navigation. Torre (2021) proposes an angles-only navigation solution that relies on cameras, without using a LRF [28]. The spacecraft is positioned at the Lagrange
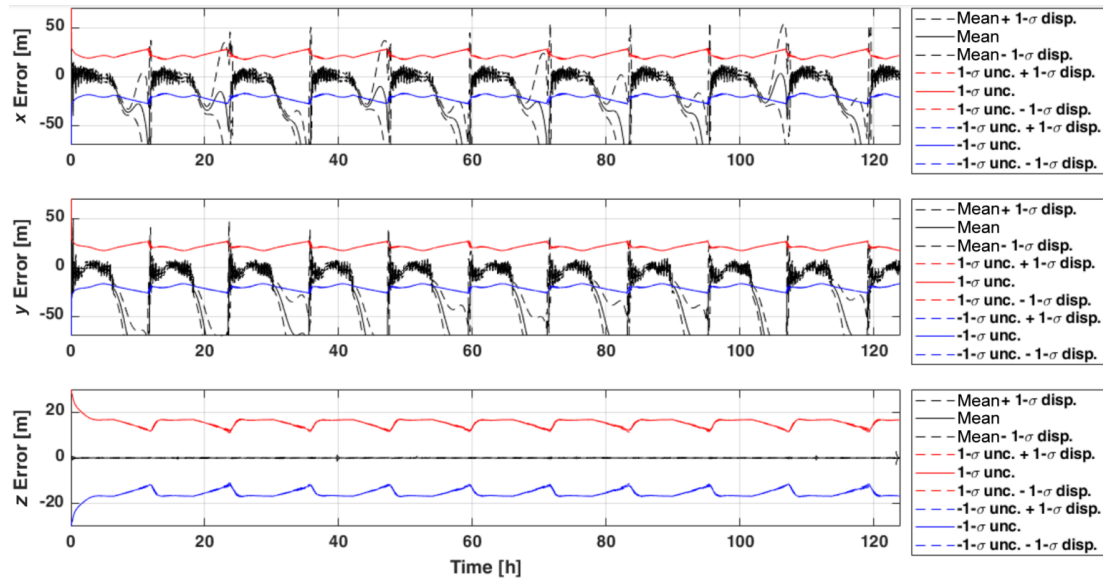
Figure 6.6: "Position estimation error components and respective 1-σ uncertainty." [28]

point L4 in the binary asteroid system Didymos, with excellent angular separation of the asteroids resulting in an observable state. These results from literature are best compared to the results for pointing at the midpoint in between the asteroids. This leads to a similar measurement set-up, without an LRF and with two LOS measurements to the two asteroids.

The spacecraft in [28] always stays at L4 at about 1.3 km from the secondary, while in this work the spacecraft is continuously moving towards the secondary asteroid. Therefore, the results are best compared when the spacecraft is at a similar distance from the secondary. This is around t=10500 s. The results as presented in [28] are shown in Fig. 6.6. The results for the simulation run in which the camera is pointed in the midpoint between the asteroids is shown in Fig. 6.7. Unfortunately one of the asteroids has already left the camera frame at t=10500, which triggered the reorientation maneuver. This is solved in [28] by using multiple cameras. The final time where pointing at the midpoint is still used is therefore used for the comparison.

The 1σ state estimation error uncertainty for the method presented in this work is 20, 8, and 5 m for the X-, Y-, and Z-axes, respectively. These values are comparable to the best-case performance shown in Fig. 6.6. The solution in [28] is estimating the position for a much longer time horizon, which also includes eclipse periods during which the image processing is struggling much more than in the near-optimal lighting conditions assumed in this work. The results are very similar between the two navigation systems which is reason to believe that the navigation system presented in this work is implemented correctly. This comparison only provides pseudo-validation of the vision-based part of the navigation system.

6.2.3. Image processing validation

Image processing plays a crucial role in the navigation system of the spacecraft. Validating its performance on-ground is difficult because the space environment is not easily replicated. ESA's GNC Rendezvous, Approach and Landing Simulator (GRALS)[1], depicted in Fig. 6.8, is an excellent candidate to validate the image processing part of the navigation system without going to space. The robotic arm can be equipped with cameras and ranging sensors, and is attached to a 33 meter long moving track. The testbench is specifically designed to simulate the close approach and landing on uncooperative objects, such as asteroids.

Validation testing with GRALS could be the final on-ground validation step, after testing with camera simulators such as PANGU and asteroid images from previous missions. This is still not a form of true validation because reality will inevitably be different than what is in GRALS as well.

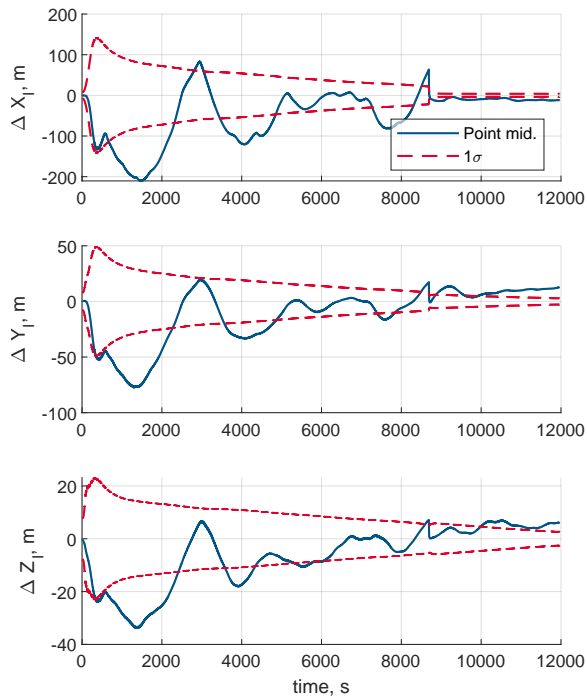[1]`https://www.esa.int/ESA_Multimedia/Images/2018/05/GRALS_Testbed`, last accessed 2023/03/21

Figure 6.7: I-frame position estimation errors, including error 1σ bounds. EKF without LRF mismatch estimation. Pointing at the midpoint, switching to secondary at t=8690 s.
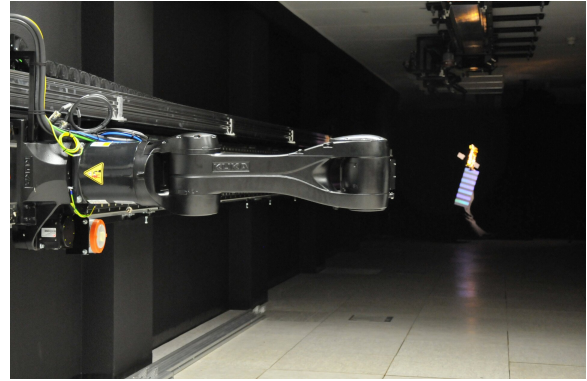
Figure 6.8: ESA's GNC Rendezvous, Approach and Landing Simulator (GRALS). Image credit: ESA - M.Grulich

6.2.4. Full system validation

Several major assumptions have been made in this work. For example, the attitude and pointing side of the GNC problem is completely left out. The solar radiation pressure and gravity field will exert a disturbance torque on the spacecraft as well, which is currently not modeled. The thrusters and their dynamics, the sloshing of fuel, and the vibrations and flexible modes of the spacecraft are all relevant characteristics of the spacecraft. Full system validation should be conducted to look after all these aspects.

To validate the navigation system in a relatively low-risk manner, fly-bys with other Solar System bodies on the way to the target asteroid could be exploited to test the navigation system. This method was also used by Rosetta when it flew past (2867) Šteins and (21) Lutetia [65]. On-board optical measurements were used to navigate the spacecraft such that it met the requested fly-by conditions.

Ideally, the object used for the fly-by validation run is very well documented. This includes a precise shape model and ephemeris. The environment of this asteroid can then be recreated in the simulator, and the navigation performance is compared between reality and the simulator. Because the asteroid that is used for the validation is well documented, the expected errors can be calculated in the simulator. These errors can then be compared to those found in the real spacecraft navigation system, validating the navigation system.

Part IV

Closure

7

Conclusions

The ongoing interest in asteroids keeps researchers and space agencies occupied with the quest for improved navigation systems. Autonomy is identified as a key technology to reduce mission cost while simultaneously improving the capabilities of the spacecraft in terms of safety and operational return. Vision based navigation has proven to be a reliable method to fulfil the navigation needs of spacecraft in the vicinity of asteroids, and will continue to evolve over time.

The development of vision based navigation systems for asteroid navigation poses many challenges. The differences between the simulated reality and the real asteroid environment if one of these challenges. The complexity of creating realistic visuals in a simulator and the required validation task that comes with it, and the complex dynamics of the asteroid environment are prime examples of why it is difficult to recreate the asteroid environment in a simulator.

With careful consideration of the limitations of the simulated asteroid environment, the door to the development of incremental improvements of state-of-the-art navigation systems is opened. This work is an example of such an incremental improvement, which combines the outcomes of several other research works.

Closing remarks on the main findings of this work are given in Section 7.1, followed by the answering of the research questions in Section 7.2. Finally, recommendations for future work are given in Section 7.3.

7.1. Closing remarks

Traditional asteroid navigation systems have shown great success by enabling spacecraft to execute their scientific mission tasks. Prime examples are asteroid sample return missions such as JAXA's Hayabusa-1 and NASA's OSIRIS-REx. These missions demonstrate the current capabilities of asteroid navigation.

This research extends the current scientific body on asteroid navigation by investigating an autonomous navigation system that relies on minimal prior knowledge about the asteroid. On top of this, a minimalistic and low-cost hardware setup is considered. The navigation system is developed from the ground up to take advantage of the presence of multiple asteroids within a binary asteroid system.

The results of the work show that the navigation performance of the developed system is satisfactory for the requirements set in the NEO-MAPP study. Furthermore, it is shown that the navigation can also be performed in the case of a failure of the laser range finder, although the performance deteriorates significantly.

The image processing algorithm is identified as a key sensitivity of the navigation system. The image processing task is complex due to challenging lighting conditions at high sun phase angles, asteroids overlapping in the images, and irregularly shaped asteroids. The sensitivity study in this work shows that the navigation system is robust to changing illumination conditions, but the performance is impacted.

7.2. Research questions

The research objective and research questions posed in Section 1.3 form the pillars of the research work. The research objective is:

Research Objective

Investigate how an autonomous spacecraft can determine its absolute position and velocity in proximity of a binary asteroid by using vision-based navigation.

which led to the six research questions. Each of these six research questions will be briefly answered below, concluding the work that is done to fulfil the research objective.

Research Question 1

What is the state of the art of navigation around asteroids?

The state of the art of navigation around asteroids is split in the historical missions described in Section 3.2, and recent advancements in the scientific literature described in Section 3.3 and Section 2.1 of the paper. Historic missions relied heavily on radiometric tracking for the approach phase, followed by a precise characterization phase once in the vicinity of the asteroid. For close proximity operations, autonomous navigation without Earth-based measurements is made possible by exploiting the information gathered in the characterization phase.

Recent work has focused on increasing the autonomy of the spacecraft navigation system by relying more on measurements relative to the asteroid that are obtained locally. Swarms of spacecraft collaborating together to navigate an unknown environment is also a concept that is gaining attention by the scientific community. AI techniques show great potential in the field of asteroid navigation as well, but verification and validation remain a point of concern. One reason for this is that the unknown aspects of the asteroid environment must somehow be accounted for, without overfitting a solution to the environment assumed in the training dataset. The exact workings of AI-based methods is often not very well understood, because the connections and patterns it recognizes in the training data is captured in a condensed form, for example in the weights of a neural network. With traditional methods, it's therefore most likely easier to say with high certainty how the navigation solution will respond to an edge case, whereas for AI-based methods this is more challenging.

Research Question 2

What are the requirements for a simulator that can be used to develop the navigation system?

RQ 2 is answered in Section 4.1 and Sections 2.2 and 2.3 of the paper. An analysis of the relevant forces and the fidelity of the components of the simulator is essential to understand the validity of the results that the simulator produces. A key component in the development of a vision based navigation solution is the camera simulator. Naturally, verification and validation of the camera simulator is essential to be confident in the results it produces. This process is described in Chapter 6.

Research Question 3

What prior knowledge about the asteroid environment is required to estimate the spacecraft state with a given sensor suite?

RQ 3 is answered in Sections 3.3 and 3.4 and Section 2.5 of the paper. The required prior knowledge depends on the navigation concept. For kinetic impactors such as DART, knowledge of the distance to the asteroid is not as important as for a mission that involves a controlled landing. This allows the navigation system for kinetic impactors to require much less knowledge about the target body compared to other asteroid missions. For autonomous close proximity operations, traditional methods use extensive prior knowledge in the form of a shape model, gravity model, and often a library of known landmarks. Recent developments try to avoid this dependence on prior knowledge by deploying AI-based methods, or by exploiting new navigation systems with swarms of spacecraft.

> **Research Question 4**
>
> What are the performance requirements for the navigation system, and how do these require-
> ments change during the iterative design process?

RQ 4 is answered in Section 3.4 and in Section 2.5 of the paper. The default requirements are set by the study NEO-MAPP study. The 3σ position knowledge error for any axis shall be below 10% of the distance to the target asteroid. The initial distance to the asteroid in the I-frame shall be in the range [5,8] $\pm$ 0.05 km. The initial velocity in the I-frame is in the range [7,14] $\pm$ 10% cm/s. The final altitude above the outward facing pole of the asteroid during the high altitude phase shall be such that the low altitude navigation system can take over.

Initially the final altitude was set to 300 m, which is the point at which the secondary asteroid fills the FOV of the camera. Because the spacecraft approaches towards a point on the outward facing pole of the secondary asteroid, the primary will inevitably show behind the secondary. The current implementation of the image processing cannot handle images in which the bounding boxes around the asteroids are overlapping, triggering an early shutdown of the simulation at about 550 m altitude for the reference trajectory. This final altitude depends on the trajectory, but ultimately the overlap of the two asteroids cannot be escaped with the current implementation of the pointing algorithm. This is the starting point of an iterative process with the engineers responsible for the low-altitude phase of the landing. If their navigation solution is compatible with the 550 m altitude (and some margin), there is no problem. Else, a solution must be found such that the spacecraft can approach closer in the high altitude phase. For instance by using a more sophisticated image processing algorithm that can deal with overlapping bodies.

> **Research Question 5**
>
> Which navigation systems can meet the performance requirements?

RQ 5 is partially answered in Sections 3.4 and 3.5 by exploring several navigation system options found in literature. The stringent requirements on the sensors that can be used for the navigation already disqualify many options. What remains is a quest to find the best possible performance by combining methods from literature that exploit the sensors that are onboard of the NEO-MAPP spacecraft.

The performance of the navigation system developed in this work is now compared to the performance requirements. In Section 2.5 of the paper, the sensitivity of the EKF to varying filter state initializations is studied. The requirement from the NEO-MAPP study is 50 m uncertainty in the distance to the target, which is tested with a 30 m uncertainty (1σ) on every position axis in the filter state. This uncertainty corresponds to a 51.96 m uncertainty in the distance ($\sqrt{3*30^2}$). For the velocity a very conservative uncertainty of 5 m/s (1σ) is used instead of the required uncertainty that is in the order of cm/s. For the accelerometer bias, a conservative uncertainty of 0.01 m/s^2 (1σ) is used. The EKF converges in 390 out of 400 tests with these parameters. This indicates that it is very likely that the requirements of the study are met, given the conservative uncertainties used in the sensitivity study.

Section 2.5 of the paper shows that the EKF has no trouble with starting distances in the range of [5,8] km and starting velocities in the range of [7,14] cm/s.

There are most likely other navigation systems that can also fulfil the performance requirements. However, only one working option is studied in this work. Future research could explore other options.

> **Research Question 6**
>
> What are the key sensitivities of the developed navigation system?

RQ 6 is answered in Section 2.5 of the paper. The key sensitivities are identified to be related to the image processing and the quality of the shape model that is used in the measurements model of the navigation filter. Other sensitivities might come to light when the simulator is further developed, or when validation testing is conducted. The interaction between the navigation system and other components of the spacecraft, which are currently not simulated, might bring other sensitivities to light.

7.3. Recommendations

This section provides a brief overview of the primary recommendations for the future continuation of this research project.

Include attitude control and estimation:

The pointing algorithm currently relies on the perfect knowledge of the state and asteroid ephemeris. This is an essential part to obtain the camera measurements that are inputs for the EKF. In reality, this perfect knowledge is not available and therefore the spacecraft must determine and control its attitude. The desired pointing direction of the camera and LRF must be based on image data. Inclusion of such an image-based pointing algorithm leads to a more complete understanding of the capabilities of a spacecraft using this navigation system.

Improvements in the image processing

The issue of overlapping asteroids needs to be solved to increase the deployability of the navigation system. The current image processing requires permanent separation of the two asteroids in the frame. This limitation needs to be removed such that a wider range of approach trajectories can be flown and robustness of the state estimation is improved. The detection of the center of figure for complex asteroid shapes in challenging lighting conditions is another area of improvement. Possible improvements are to exploit prior knowledge about the asteroid shape with a data-driven approach as proposed in [66], or by using AI-based image processing such as proposed in [48]. More image imperfections should also be tested to reach a more complete understanding of the capabilities of the image processing. This work includes Gaussian blur, radial distortion, and salt & pepper noise. Many more imperfections are mentioned in [67] which can also be tested.

Verification and validation

All experiments in this work are carried out in a simulated environment. It is crucial to understand the limitations and assumptions that have been made to construct the simulated environment, to put the results in context. A list of recommendations related to verification and validation is given in Chapter 6.

Online shape model estimation

With the addition of more sensors, most importantly a Lidar or multiple laser range finders, much more information about the asteroid surface can be collected. While the navigation system does not necessarily need a precise shape model, it could always be useful to improve the performance. The goodness of fit of the shape model is identified to be one of the sensitivities of the current navigation system in Section 2.5 of the paper. The intersection of the LRF beam with a more precise shape model is described in [68].

Add more sensors

Adding more sensors potentially increases the robustness and performance of the filter. More LRF's, or a flash lidar could be added, as demonstrated in [20]. Adding a second camera allows the navigation system to obtain LOS measurements of both asteroids without being limited by the FOV of a single camera. These measurements can then be used with a triangulation technique, as presented in [28].

Explore other filter architectures

In this work the EKF is chosen for its simplicity and light computational load. In Subsection 3.3.2 many other options are identified, each with their own advantages and disadvantages. It is worthwhile to investigate how the different filter architectures compare in this particular problem.

References

[1] Morbidelli, A., Bottke W. F., J., Froeschlé, C., and Michel, P. "Origin and Evolution of Near-Earth Objects". In: *Asteroids III*. 2002, pp. 409–422.

[2] Goodrich, C. A., Hartmann, W. K., O'Brien, D. P., Weidenschilling, S. J., Wilson, L., Michel, P., and Jutzi, M. "Origin and history of ureilitic material in the solar system: The view from asteroid 2008 TC3 and the Almahata Sitta meteorite". In: *Meteoritics & Planetary Science* 50.4 (2015), pp. 782–809. DOI: `10.1111/maps.12401`.

[3] Alexander, C. M. O., Boss, A. P., and Carlson, R. W. "The Early Evolution of the Inner Solar System: A Meteoritic Perspective". In: *Science* 293.5527 (2001), pp. 64–68. DOI: `10.1126/science.1052872`.

[4] Izidoro, A., Raymond, S. N., Pierens, A., Morbidelli, A., Winter, O. C., and Nesvorny, D. "The asteroid belt as a relic from a chaotic early Solar System". In: *The Astrophysical Journal* 833.1 (2016), p. 40. DOI: `10.3847/1538-4357/833/1/40`.

[5] Anthony, N. and Emami, M. R. "Asteroid engineering: The state-of-the-art of Near-Earth Asteroids science and technology". In: *Progress in Aerospace Sciences* 100 (June 2018), pp. 1–17. ISSN: 0376-0421. DOI: `10.1016/j.paerosci.2018.05.001`.

[6] Chapman, C. R. "The hazard of near-Earth asteroid impacts on earth". In: *Earth and Planetary Science Letters* 222.1 (2004), pp. 1–15. ISSN: 0012-821X. DOI: `10.1016/j.epsl.2004.03.004`.

[7] Adams, E. et al. "Double Asteroid Redirection Test: The Earth Strikes Back". In: *2019 IEEE Aerospace Conference*. 2019, pp. 1–11. DOI: `10.1109/AERO.2019.8742007`.

[8] Cheng, A. F. et al. "Momentum Transfer from the DART Mission Kinetic Impact on Asteroid Dimorphos". In: *Nature* (Mar. 2023), pp. 1–3. DOI: `10.1038/s41586-023-05878-z`.

[9] Thornton, C. L. and Border, J. S. *Radiometric tracking techniques for deep-space navigation*. en. Deep-space communications and navigation series. Nashville, TN: John Wiley & Sons, Jan. 2003.

[10] Ulamec, S. et al. "Rosetta Lander – Landing and operations on comet 67P/Churyumov–Gerasimenko". In: *Acta Astronautica* 125 (Aug. 2016), pp. 80–91. DOI: `10.1016/j.actaastro.2015.11.029`.

[11] Kominato, T., Matsuoka, M., Uo, M., Hashimoto, T., Kubota, T., and Kawaguchi, J. "Hayabusa's Optical Hybrid Navigation for Approaching to and Stationkeeping around Asteroid Itokawa". In: *The Journal of Space Technology and Science* 22.1 (2006), pp. 11–20.

[12] Castellini, F., De Santayana, R. P., Wokes, D., and Kielbassa, S. "Optical navigation for Rosetta operations near comet Churyumov-Gerasimenko". In: *Advances in the Astronautical Sciences* 150 (Jan. 2014), pp. 1619–1637.

[13] Tsuda, Y., Yoshikawa, M., Abe, M., Minamino, H., and Nakazawa, S. "System design of the Hayabusa 2—Asteroid sample return mission to 1999 JU3". In: *Acta Astronautica* 91 (2013), pp. 356–362. ISSN: 0094-5765. DOI: `10.1016/j.actaastro.2013.06.028`.

[14] Antreasian, P. G. et al. "OSIRIS-REx Proximity Operations and Navigation Performance at Bennu". In: *AIAA SCITECH 2022 Forum*. American Institute of Aeronautics and Astronautics, Jan. 2022. DOI: `10.2514/6.2022-2470`.

[15] Gil-Fernandez, J., Prieto-Llanos, T., Cadenas-Gorgojo, R., Graziano, M., and Drai, R. "Autonomous GNC Algorithms for Rendezvous Missions to Near-Earth-Objects". In: *AIAA/AAS Astrodynamics Specialist Conference and Exhibit*. American Institute of Aeronautics and Astronautics, June 2008. DOI: `10.2514/6.2008-7087`.

[16] Liounis, A. J. "Limb based optical navigation for irregular bodies". In: *1st Annual RPI Workshop on Image-Based Modeling and Navigation for Space Applications, Troy, NY*. 2018.

[17] Negri, R. B., Prado, A. F. B. d. A., Chagas, R. A. J., and Moraes, R. V. de. *Autonomous Rapid Exploration in Close-Proximity of an Asteroid*. 2022. DOI: `10.48550/ARXIV.2208.03378`.

[18] Rowell, N., Dunstan, M., Parkes, S., Gil-Fernández, J., Huertas, I., and Salehi, S. "Autonomous visual recognition of known surface landmarks for optical navigation around asteroids". In: *The Aeronautical Journal* 119.1220 (2015), pp. 1193–1222.

[19] De Santayana, R. P. and Lauer, M. "Optical measurements for Rosetta navigation near the comet". In: *Proceedings of the 25th International Symposium on Space Flight Dynamics (ISSFD), Munich*. 2015.

[20] Dietrich, A. and McMahon, J. W. "Asteroid Proximity Navigation using Flash LIDAR". In: *AIAA/AAS Astrodynamics Specialist Conference*. American Institute of Aeronautics and Astronautics, Aug. 2014. DOI: `10.2514/6.2014-4355`.

[21] Morley, T. and Budnik, F. "Rosetta Navigation for the Fly-by of Asteroid 2867 Šteins". In: *Proceedings 21st International Symposium on Space Flight Dynamics-21st ISSFD, Toulouse, France*. 2009.

[22] Synnott, S., Donegan, A., Riedel, J., and Stuve, J. "Interplanetary optical navigation-Voyager Uranus encounter". In: *Astrodynamics Conference*. American Institute of Aeronautics and Astronautics, Aug. 1986. DOI: `10.2514/6.1986-2113`.

[23] Vetrisano, M. and Vasile, M. "Autonomous navigation of a spacecraft formation in the proximity of an asteroid". In: *Advances in Space Research* 57.8 (Apr. 2016), pp. 1783–1804. DOI: `10.1016/j.asr.2015.07.024`.

[24] Christian, J. A. and Lightsey, E. G. "Onboard Image-Processing Algorithm for a Spacecraft Optical Navigation Sensor System". In: *Journal of Spacecraft and Rockets* 49.2 (2012), pp. 337–352. DOI: `10.2514/1.A32065`.

[25] Christian, J. A. "Optical Navigation Using Planet's Centroid and Apparent Diameter in Image". In: *Journal of Guidance, Control, and Dynamics* 38.2 (Feb. 2015), pp. 192–204. DOI: `10.2514/1.g000872`.

[26] Morita, H., Shirakawa, K., Kubota, T., Hashimoto, T., and Kawaguchi, J. "Hayabusa's Real-time Landmark Tracking Navigation for Descents and Touching-Downs". In: *AIAA/AAS Astrodynamics Specialist Conference and Exhibit*. American Institute of Aeronautics and Astronautics, June 2006. DOI: `10.2514/6.2006-6537`.

[27] Adam, C. D. et al. "Transition from Centroid-Based to Landmark-Based Optical Navigation During OSIRIS-REx Navigation Campaign at Asteroid Bennu". In: *RPI Space Imaging Workshop*. 2019.

[28] Torre, F., Grey, S., and Vasile, M. "Angles-Only Navigation in the Proximity of a Binary Asteroid System". In: *Journal of Guidance, Control, and Dynamics* 44.1 (Jan. 2021), pp. 57–74. DOI: `10.2514/1.g004355`.

[29] Stastny, N. B. and Geller, D. K. "Autonomous Optical Navigation at Jupiter: A Linear Covariance Analysis". In: *Journal of Spacecraft and Rockets* 45.2 (Mar. 2008), pp. 290–298. DOI: `10.2514/1.28451`.

[30] Jia, H., Zhu, S., and Cui, P. "Observability-Based Navigation Using Optical and Radiometric Measurements for Asteroid Proximity". In: *IEEE Transactions on Aerospace and Electronic Systems* 56.4 (2020), pp. 2677–2688. DOI: `10.1109/TAES.2019.2953947`.

[31] Huixin, Y., Xixiang, Y., and Weihua, Z. "State estimation of spacecraft formation near small asteroid". In: *Proceedings of 2014 IEEE Chinese Guidance, Navigation and Control Conference*. 2014, pp. 55–60. DOI: `10.1109/CGNCC.2014.7007219`.

[32] Gil-Fernandez, J. and Ortega-Hernando, G. "Autonomous vision-based navigation for proximity operations around binary asteroids". In: *CEAS Space Journal* 10.2 (2018), pp. 287–294.

[33] Takahashi, S. and Scheeres, D. J. "Autonomous Exploration of a Small Near-Earth Asteroid". In: *Journal of Guidance, Control, and Dynamics* 44.4 (2021), pp. 701–718.

[34] Jedicke, R., Granvik, M., Micheli, M., Ryan, E., Spahr, T., and Yeomans, D. K. "Surveys, Astrometric Follow-Up, and Population Statistics". In: *Asteroids IV*. University of Arizona Press, 2015. DOI: `10.2458/azu_uapress_9780816532131-ch040`.

[35] Busch, M. W. et al. "Radar observations and the shape of near-Earth asteroid 2008 EV5". In: *Icarus* 212.2 (2011), pp. 649–660. ISSN: 0019-1035. DOI: `10.1016/j.icarus.2011.01.013`.

[36] Scheeres, D. J. "Introduction and Background". In: *Orbital Motion in Strongly Perturbed Environments*. Springer Berlin Heidelberg, 2012, pp. 3–22.

[37] Kaasalainen, M. "Optimization Methods for Asteroid Lightcurve Inversion I. Shape Determination". In: *Icarus* 153.1 (Sept. 2001), pp. 24–36. DOI: `10.1006/icar.2001.6673`.

[38] Belton, M. J. et al. "Galileo encounter with 951 Gaspra: first pictures of an asteroid". en. In: *Science* 257.5077 (Sept. 1992), pp. 1647–1652.

[39] Panicucci, P. "Autonomous vision-based navigation and shape reconstruction of an unknown asteroid during approach phase". PhD thesis. Toulouse, ISAE, 2021.

[40] Williams, B., Antreasian, P., Bordi, J., Carranza, E., Chesley, S., Helfrich, C., Miller, J., Owen, W., and Wang, T. "Navigation for near Shoemaker: The first spacecraft to orbit an asteroid". In: *Advances in the Astronautical Sciences* 109 (Jan. 2002), pp. 973–988.

[41] Morita, H., Shirakawa, K., Uo, M., Hashimoto, T., Kubota, T., and Kawaguchi, J. "Hayabusa descent navigation based on accurate landmark tracking scheme". In: *The journal of space technology and science* 22.1 (2006), pp. 21–31.

[42] Tsuda, Y., Nakazawa, S., Kushiki, K., Yoshikawa, M., Kuninaka, H., and Watanabe, S. "Flight status of robotic asteroid sample return mission Hayabusa2". In: *Acta Astronautica* 127 (2016), pp. 702–709.

[43] Tsuda, Y., Yoshikawa, M., Abe, M., Minamino, H., and Nakazawa, S. "System design of the Hayabusa 2—Asteroid sample return mission to 1999 JU3". In: *Acta Astronautica* 91 (2013), pp. 356–362.

[44] Leonard, J. M., Geeraert, J. L., Page, B. R., French, A. S., Antreasian, P. G., Adam, C. D., Wibben, D. R., Moreau, M. C., and Lauretta, D. S. "OSIRIS-REx orbit determination performance during the navigation campaign". In: *2019 AAS/AIAA Astrodynamics Specialist Conference*. AAS 19-714. 2019.

[45] Adam, C. D. et al. "Transition from Centroid-Based to Landmark-Based Optical Navigation During OSIRIS-REx Navigation Campaign at Asteroid Bennu". In: *RPI Space Imaging Workshop*. GSFC-E-DAA-TN74664. 2019.

[46] Atchison, J. et al. "Double Asteroid Redirection Test (DART) Mission Design and Navigation for Low Energy Escape". In: *69th International Astronautical Congress*. Oct. 2018.

[47] Du, S., Wang, M., Chen, X., Fang, S., and Su, H. "A High-accuracy Extraction Algorithm of Planet Centroid Image in Deep-space Autonomous Optical Navigation". In: *Journal of Navigation* 69.4 (Dec. 2015), pp. 828–844. DOI: `10.1017/s0373463315000910`.

[48] Kaluthantrige, A., Feng, J., Gil-Fernández, J., and Pellacani, A. "Centroiding technique using machine learning algorithm for space optical navigation". In: *3rd IAA Conference in Space Situational Awareness*. 2022, pp. 1–13.

[49] Pugliatti, M. and Topputo, F. "Navigation about irregular bodies through segmentation maps". In: *31st AAS/AIAA Space Flight Mechanics Meeting*. 2021.

[50] Michel, P., Falke, A., and Ulamec, S. *The European Commission funded NEO-MAPP project in support of the ESA Hera mission: Near-Earth Object Modelling And Payload for Protection*. 2020.

[51] *The International Astronomical Union Minor Planet Center*. URL: `https://minorplanetcenter.net/db_search/show_object?&object_id=Didymos`.

[52] Naidu, S. et al. "Radar observations and a physical model of binary near-Earth asteroid 65803 Didymos, target of the DART mission". In: *Icarus* 348 (Sept. 2020), p. 113777. DOI: `10.1016/j.icarus.2020.113777`.

[53] Fang, J. and Margot, J.-L. "Near-Earth binaries and triples: Origin and evolution of spin-orbital properties". In: *The Astronomical Journal* 143.1 (2011), p. 24.

[54] Pravec, P. et al. "Photometric survey of binary near-Earth asteroids". In: *Icarus* 181.1 (2006), pp. 63–93. DOI: `10.1016/j.icarus.2005.10.014`.

[55] Dionne, K. "Improving Autonomous Optical Navigation for Small Body Exploration Using Range Measurement". In: *AIAA Guidance, Navigation, and Control Conference*. American Institute of Aeronautics and Astronautics, June 2009. DOI: `10.2514/6.2009-6106`.

[56] Walter, U. *Astronautics*. en. 3rd ed. Cham, Switzerland: Springer International Publishing, Mar. 2019.

[57] Kaula, W. *Theory of Satellite Geodesy: Applications of Satellites to Geodesy*. Blaisdell Publishing Company, 1966.

[58] Wieczorek, M. A. and Meschede, M. "SHTools: Tools for Working with Spherical Harmonics". In: *Geochemistry, Geophysics, Geosystems* 19.8 (Aug. 2018), pp. 2574–2592. DOI: `10.1029/2018gc007529`.

[59] *"Hera Didymos reference model"*. ESA-TECSP-AD-017258. Revision 3. ESA. Feb. 2020.

[60] Werner, R. A. and Scheeres, D. J. "Exterior gravitation of a polyhedron derived and compared with harmonic and mascon gravitation representations of asteroid 4769 Castalia". In: *Celestial Mechanics and Dynamical Astronomy* 65.3 (1997). DOI: `10.1007/bf00053511`.

[61] Otsu, N. "A Threshold Selection Method from Gray-Level Histograms". In: *IEEE Transactions on Systems, Man, and Cybernetics* 9.1 (1979), pp. 62–66. DOI: `10.1109/TSMC.1979.4310076`.

[62] Bar-Shalom, Y., Li, X.-R., and Kirubarajan, T. *Estimation with Applications to Tracking and Navigation*. John Wiley & Sons, Inc., 2001. DOI: `10.1002/0471221279`.

[63] Huang, G. P., Mourikis, A. I., and Roumeliotis, S. I. "Analysis and improvement of the consistency of extended Kalman filter based SLAM". In: *2008 IEEE International Conference on Robotics and Automation*. 2008, pp. 473–479. DOI: `10.1109/ROBOT.2008.4543252`.

[64] Jean, I., Ng, A., and Misra, A. K. "Impact of solar radiation pressure modeling on orbital dynamics in the vicinity of binary asteroids". In: *Acta Astronautica* 165 (2019), pp. 167–183. ISSN: 0094-5765. DOI: `https://doi.org/10.1016/j.actaastro.2019.09.003`.

[65] Lauer, M., Herfort, U., Hocken, D. B., and Kielbassa, S. "Optical measurements for the flyby navigation of rosetta at asteroid Steins". In: *Proceedings of the 21st International Symposium on Space Flight Dynamics (ISSFD), Toulouse, France*. Oct. 2009.

[66] Pugliatti, M., Franzese, V., and Topputo, F. "Data-Driven Image Processing for Onboard Optical Navigation Around a Binary Asteroid". In: *Journal of Spacecraft and Rockets* 59.3 (May 2022), pp. 943–959.

[67] Hendrycks, D. and Dietterich, T. *Benchmarking Neural Network Robustness to Common Corruptions and Perturbations*. 2019. arXiv: `1903.12261 [cs.LG]`.

[68] Razgus, B., Mooij, E., and Choukroun, D. "Relative Navigation in Asteroid Missions Using Dual Quaternion Filtering". In: *Journal of Guidance, Control, and Dynamics* 40.9 (Sept. 2017), pp. 2151–2166. DOI: `10.2514/1.g002805`.